THERMALLY INDUCED TWO-PHASE FLOW INSTABILITIES, INCLUDING THE EFFEC
SAHA, PRADIP
ProQuest Dissertations and Theses; 1974; ProQuest Dissertations & Theses Global

INFORMATION TO USERS

This material was produced from a microfilm copy of the original document. While the most advanced technological means to photograph and reproduce this document have been used, the quality is heavily dependent upon the quality of the original submitted.

The following explanation of techniques is provided to help you understand markings or patterns which may appear on this reproduction.

1. The sign or "target" for pages apparently lacking from the document photographed is "Missing Page(s)". If it was possible to obtain the missing page(s) or section, they are spliced into the film along with adjacent pages. This may have necessitated cutting thru an image and duplicating adjacent pages to insure you complete continuity.

2. When an image on the film is obliterated with a large round black mark, it is an indication that the photographer suspected that the copy may have moved during exposure and thus cause a blurred image. You will find a good image of the page in the adjacent frame.

3. When a map, drawing or chart, etc., was part of the material being photographed the photographer followed a definite method in "sectioning" the material. It is customary to begin photoing at the upper left hand corner of a large sheet and to continue photoing from left to right in equal sections with a small overlap. If necessary, sectioning is continued again — beginning below the first row and continuing on until complete.

4. The majority of users indicate that the textual content is of greatest value, however, a somewhat higher quality reproduction could be made from "photographs" if essential to the understanding of the dissertation. Silver prints of "photographs" may be ordered at additional charge by writing the Order Department, giving the catalog number, title, author and specific pages you wish reproduced.

5. PLEASE NOTE: Some pages may have indistinct print. Filmed as received.

Xerox University Microfilms
300 North Zeeb Road
Ann Arbor, Michigan 48106

Reproduced with permission of the copyright owner. Further reproduction prohibited without permission.

74-21,580

SAHA, Pradip, 1948-
THERMALLY INDUCED TWO-PHASE FLOW INSTABILITIES, INCLUDING THE EFFECT OF THERMAL NON-EQUILIBRIUM BETWEEN THE PHASES.

Georgia Institute of Technology, Ph.D., 1974
Engineering, mechanical

University Microfilms, A XEROX Company, Ann Arbor, Michigan

Reproduced with permission of the copyright owner. Further reproduction prohibited without permission.

THERMALLY INDUCED TWO-PHASE FLOW INSTABILITIES, INCLUDING THE EFFECT OF THERMAL NON-EQUILIBRIUM BETWEEN THE PHASES

A THESIS

Presented to

The Faculty of the Division of Graduate

Studies and Research

by

Pradip Saha

In Partial Fulfillment

of the Requirements for the Degree

Doctor of Philosophy

in the School of Mechanical Engineering

Georgia Institute of Technology

June, 1974

Reproduced with permission of the copyright owner. Further reproduction prohibited without permission.

THERMALLY INDUCED TWO-PHASE FLOW INSTABILITIES, INCLUDING

THE EFFECT OF THERMAL NON-EQUILIBRIUM

BETWEEN THE PHASES

Approved:

N. Zuber, Chairman

W. Wulff

R. S. Devoto

J. C. Wu

C. W. Gorton

Date approved by Chairman: 4/26/77

Reproduced with permission of the copyright owner. Further reproduction prohibited without permission.

TO MY PARENTS

Reproduced with permission of the copyright owner. Further reproduction prohibited without permission.

ACKNOWLEDGMENTS

The author wishes to express his deep sense of gratitude and indebtedness to his thesis advisor, Dr. Novak Zuber, for introducing the author to the area of two-phase flow, for suggesting the present problem, and for continuous guidance and encouragement without which this work could not be completed.

It is a great pleasure to thank Drs. W. Wulff, C. W. Gorton, J. C. Wu, and R. S. Devoto for their interest and constructive suggestions in the course of reviewing this work.

The boiling loop used by the author to obtain experimental data was built through the hard work of a group of faculty members, graduate students, and able technicians of the School of Mechanical Engineering at Georgia Institute of Technology. The author is grateful to all of them, particularly to Dr. M. Ishii and Mr. Y. Kim with whom he had worked closely during the construction and initial operation of the loop.

The present work, including the construction of the boiling loop, was sponsored by the National Science Foundation (Grant no. KG-16023). The author is thankful to the above organization for the financial assistance.

Finally, the author would like to thank all of his colleagues, friends, and well-wishers for their encouragement and friendship during the period of execution of this work.

Reproduced with permission of the copyright owner. Further reproduction prohibited without permission.

TABLE OF CONTENTS

	Page
ACKNOWLEDGMENTS	iii
LIST OF TABLES	vi
LIST OF ILLUSTRATIONS	vii
NOMENCLATURE	x
SUMMARY	xv
Chapter I. INTRODUCTION	1
1. Definition of the Problem	1
2. Objectives of the Thesis	3
3. Outline of the Thesis	3
Part 1--EXPERIMENTAL PROGRAM	5
II. EXPERIMENTAL INVESTIGATION	6
1. Description of the Boiling Loop	6
2. Details of the Test Section Assembly	10
3. Loop Instrumentation	12
4. Procedure of the Experiment	17
5. Experimental Results	22
Part 2--THEORETICAL ANALYSIS	36
III. STATE OF THE ART	37
1. Types of Instabilities	37
2. Previous Work on Low Frequency Oscillations	38
IV. EFFECT OF THERMAL NON-EQUILIBRIUM ON VAPOR VOID FRACTION	42
1. Description of a Boiling Channel	42
2. Previous Work on Point of Net Vapor Generation	45
3. Present Model for the Point of Net Vapor Generation	50
4. Prediction of True Vapor Void Fraction	58

Reproduced with permission of the copyright owner. Further reproduction prohibited without permission.

TABLE OF CONTENTS (Continued)

Chapter			Page
IV.	5.	Constitutive Relation for the Rate of Vapor Generation.	61
	6.	Comparison of Predicted Vapor Void Fraction with Experimental Data	66
V.		STABILITY ANALYSIS.	69
	1.	Formulation of the Problem.	69
	2.	Method of Solution.	81
	3.	Kinematics of the Flow.	84
	4.	Dynamics of the Flow.	96
	5.	General Characteristic Equation	104
	6.	Determination of Transfer Functions	105
	7.	Non-Dimensional Characteristic Equation	116
	8.	Determination of Stability Boundary	120
VI.		RESULTS AND DISCUSSIONS	127
	1.	Results of the Theoretical Analysis	127
	2.	Comparison with Experimental Data	131
VII.		SIMPLIFIED STABILITY CRITERION.	144
VIII.		CONCLUSIONS	149
APPENDICES			151
A.		COEFFICIENTS OF THE NON-DIMENSIONAL CHARACTERISTIC EQUATION	152
B.		THE PROGRAM "INSTAB".	163
	1.	The Flow Diagram.	163
	2.	The Listing of the Program.	166
C.		REDUCED EXPERIMENTAL DATA FOR COMPARISON WITH THEORETICAL PREDICTIONS.	172
D.		UNCERTAINTY OF THE EXPERIMENTAL DATA.	176
E.		REPEATABILITY OF THE EXPERIMENTAL DATA.	177
BIBLIOGRAPHY			180
VITA			184

Reproduced with permission of the copyright owner. Further reproduction prohibited without permission.

LIST OF TABLES

Table		Page
1.	Results for Set No. I	24
2.	Results for Set No. II	25
3.	Results for Set No. III	26
4.	Results for Set No. IV	27
5.	Results for Set No. V	28
6.	Results for Set No. VI	29
7.	Results for Set No. VII	30
8.	Data Used for the Present Correlation	54
9.	Reduced Data for Set No. I	172
10.	Reduced Data for Set No. II	173
11.	Reduced Data for Set No. III	173
12.	Reduced Data for Set No. IV	174
13.	Reduced Data for Set No. V	174
14.	Reduced Data for Set No. VI	175
15.	Reduced Data for Set No. VII	175
16.	Reduced Data for Set No. I(b)	177

Reproduced with permission of the copyright owner. Further reproduction prohibited without permission.

LIST OF ILLUSTRATIONS

Figure		Page
1.	Schematic of the Boiling Loop	7
2.	Details of the Test Section Assembly	11
3.	Schematic of the Pressure and Flow Measuring Arrangement	15
4.	A Typical Inlet Flow Trace with Increasing Power Input (Run No. OT 11, Set No. IV)	20
5.	Determination of the Point of Inception of Flow Oscillation (Run No. OT 11, Set No. IV)	21
6.	Heat Transfer Coefficient from the Test Section to the Surrounding Air	23
7.	Trace of Inlet Flow and System Pressure Drop (Run No. OT 34, Set No. VI)	32
8.	Trace of Inlet Flow and System Pressure Drop (Run No. OT 45, Set No. VII)	33
9.	Trace of Inlet Flow and System Pressure Drop (Run No. OT 15, Set No. IV)	34
10.	Trace of Inlet Flow and System Pressure Drop (Run No. OT 16, Set No. IV)	35
11.	A Typical Boiling Channel	43
12.	Peclet Number versus Stanton Number at the Point of Net Vapor Generation	55
13.	Comparison between Predicted and Measured Vapor Void Fraction; Data of Martin [34]	67
14.	Comparison between Predicted and Measured Vapor Void Fraction; Data of Lobachev, et al. [43]	67
15.	Comparison between Predicted and Measured Vapor Void Fraction; Data of Staub, et al. [35]	68

Reproduced with permission of the copyright owner. Further reproduction prohibited without permission.

LIST OF ILLUSTRATIONS (Continued)

Figure		Page
16.	Mathematical Representation of the Physical System.	70
17.	Comparison between the Present Non-Equilibrium Model and the Equilibrium Model for the Rate of Vapor Generation.	82
18.	Modified Distribution for the Rate of Vapor Generation.	107
19.	The Stability Plane	122
20.	The Stability Map for Case I.	129
21.	The System Stability Boundaries for Case I and Case II	130
22.	Comparison between the Equilibrium and the Non-Equilibrium Theories.	132
23.	Comparison of Experimental Data on the Onset of Flow Oscillation with Various Theoretical Predictions	133
24.	Comparison of Experimental Data on the Frequency of Oscillation with Various Theoretical Predictions	134
25.	Comparison of Experimental Data on the Onset of Flow Oscillation with Various Theoretical Predictions	136
26.	Comparison of Experimental Data on the Frequency of Oscillation with Various Theoretical Predictions	137
27.	The Effect of System Pressure	138
28.	The Effect of Inlet Restriction	140
29.	The Effect of Exit Restriction.	141
30.	The Effect of Reynolds Number	142
31.	Critical Subcooling Number and Construction of Simplified Stability Criterion	146

Reproduced with permission of the copyright owner. Further reproduction prohibited without permission.

LIST OF ILLUSTRATIONS (Concluded)

Figure		Page
32.	Construction of Simplified Stability Criterion.	148
33.	Comparison of Stability Boundary between Sets No. I and I(b)	178
34.	Comparison of Frequency of Oscillation between Sets No. I and I(b)	179

Reproduced with permission of the copyright owner. Further reproduction prohibited without permission.

NOMENCLATURE

Latin

A_c	cross-sectional area of the channel
a	thermal diffusivity
C_i	coefficients defined in Appendix A
C_k	kinematic wave velocity
$C^*_{k,CD}$	function defined by Equation (5.172)
$C^*_{k,DE}$	function defined by Equation (5.173)
$C^*_{k,CE}$	function defined by Equation (5.181)
C_m	coefficient for mixture friction factor
C_o	distribution parameter
c_p	specific heat
D_d	departing bubble diameter
D_i	coefficients defined in Appendix A
D_h	hydraulic diameter
E(z)	function defined by Equation (5.86)
f	frequency of oscillation
f_f	liquid friction factor
f_m	mixture friction factor
$f(\beta)$	bubble contact angle function
G	mass velocity
g	acceleration due to gravity
H(z,s)	function defined by Equation (5.91)

Reproduced with permission of the copyright owner. Further reproduction prohibited without permission.

NOMENCLATURE (Continued)

h_f	single phase heat transfer coefficient
h_l	heat transfer coefficient given by (4.12)
I_1	function defined by Equation (5.178)
I_2	function defined by Equation (5.179)
i	enthalpy
i_1	enthalpy at the inlet of the channel
Δi_{fg}	latent heat of vaporization
Δi_{sub}	inlet subcooling, $i_{fs} - i_1$
Δi_λ	subcooling at the point of net vapor generation
j	volumetric flux density
K(s)	function defined by Equation (5.165)
k	thermal conductivity
k_i, k_e	inlet and exit orifice coefficients
ℓ	length of the channel
$\Delta\ell$	characteristic length, $\bar{\lambda}_{eq} - \bar{\lambda}$
$\Delta\ell_c$	the length $\bar{\lambda}_{cb} - \bar{\lambda}$ defined in section V-6
ℓ_c^*	the ratio $\Delta\ell_c / \Delta\ell$
$N_{pch,eq}$	equilibrium phase change number
N_{sub}	subcooling number
Nu	Nusselt number at the point of net vapor generation
P	pressure
P_s	system pressure
ΔP	pressure drop
ΔP_s	system pressure drop

Reproduced with permission of the copyright owner. Further reproduction prohibited without permission.

NOMENCLATURE (Continued)

Pe	Peclet number
Pr	Prandtl number
Q(s)	characteristic function
$\dot{q}''_w$	wall heat flux
Re	Reynolds number
St	Stanton number at the point of net vapor generation
s	perturbation variable, $a + j\omega$ ($j = \sqrt{-1}$)
	a = amplification factor
	ω = angular frequency
T	temperature
T_{sat}	saturation temperature
ΔT	local subcooling, $T_{sat} - T$
t	time
v	velocity
v_{fi}	velocity at the inlet of the channel
V_{gj}	vapor drift velocity, $v_g - j$
$\bar{V}_{gj}$	weighted mean vapor drift velocity
x	true vapor quality
x_{eq}	equilibrium vapor quality
$x_{e,eq}$	x_{eq} at the exit of the channel
x_λ	x_{eq} at the point of net vapor generation
$Y_{B \text{ or } d}$	distance of the top of the departing bubble from the wall
z	axial co-ordinate
$Z^*(s^*)$	shifted characteristic function

Reproduced with permission of the copyright owner. Further reproduction prohibited without permission.

NOMENCLATURE (Continued)

Greek

α	vapor void fraction
Γ_g	mass rate of vapor generation per unit volume
$\Gamma_{g,eq}$	Γ_g under thermal equilibrium assumption
ϵ	perturbation magnitude ($\ll \bar{v}_{fi}$)
λ	distance of the boiling boundary from the inlet
λ_{eq}	λ under thermal equilibrium assumption
λ_{CD}	distance defined in section V-6
Λ_i	various transfer functions
μ	viscosity
ξ_h	heated perimeter
ρ	density
$\Delta\rho$	density difference between the phases, $\rho_f - \rho_g$
σ	surface tension
τ	particle co-ordinate
τ_{12}	residence time in the heated liquid region
τ_{34}	residence time in the region D defined in section V-6
τ_w	wall shear stress
ϕ	function defined by Equation (5.72)
Ω	local characteristic frequency of phase change
Ω_{eq}	equilibrium frequency of phase change
ω	angular frequency of oscillation

Reproduced with permission of the copyright owner. Further reproduction prohibited without permission.

NOMENCLATURE (Continued)

Subscripts

c	in the region C defined in section V-6
D	in the region D defined in section V-6
e	at the exit of the channel
ex	external
f	liquid phase
g	vapor phase
i or 1	at the inlet of the channel
m	two phase mixture
s	saturation condition
w	at the wall
12	heated liquid region
24	heated mixture region
34	region D defined in section V-6
λ	at the point of net vapor generation

Superscripts

+ or *	dimensionless

Special Notations

$\bar{G}$	steady state part of variable G
δG	perturbed part of variable G
ΔF	increment in function F
$\langle\ \rangle$	area averaged

Reproduced with permission of the copyright owner. Further reproduction prohibited without permission.

SUMMARY

The problem of thermally induced two-phase flow instabilities has been studied both experimentally and theoretically. In the experimental part, i.e., the first part, of the thesis the onset of thermally induced flow oscillations in a uniformly heated boiling channel has been presented. This consists of a brief description of the design, construction, and instrumentation of the boiling loop, which is followed by the procedure used in obtaining the data on the onset of flow oscillation and the presentation of the experimental results.

In the second part of the thesis, a theoretical analysis including the effect of thermal non-equilibrium has been carried out. A new general correlation for determining the point of net vapor generation in a boiling channel with inlet subcooling has been found. It has been discovered that, for low mass flow rates ($Pe < 70,000$) the point of net vapor generation is governed by the local thermal condition, whereas for high mass flow rates ($Pe > 70,000$) this point is controlled by hydrodynamic condition.

A constitutive equation for the rate of vapor generation in the thermal non-equilibrium region has been derived from the steady state energy consideration. This equation, together with the new correlation for the point of net vapor generation has been successfully used to predict the vapor void fraction in various boiling channels.

The dynamic response of the system including the effect of thermal non-equilibrium has been studied by introducing a small perturbation in

Reproduced with permission of the copyright owner. Further reproduction prohibited without permission.

the inlet velocity. A characteristic equation in the form of a seventh order polynomial with three time delays has been derived. The system stability boundary in the subcooling number versus equilibrium phase change number plane is then obtained by using the D-partition method. When compared with the equilibrium theory, the present non-equilibrium theory predicts a more stable system at low subcooling number and a more unstable system at high subcooling number. Experimental data on the onset and the frequency of oscillation reported in the first part of the thesis show better agreement with the new non-equilibrium model (assuming no change in the local subcooling at the boiling boundary) than with the equilibrium model. A simplified stability criterion, which can be used for preliminary estimation of the system stability boundary, has also been developed for low subcooling number.

Reproduced with permission of the copyright owner. Further reproduction prohibited without permission.

CHAPTER I

INTRODUCTION

I-1. Definition of the Problem

It is well known that two-phase flow instabilities can introduce operational and safety problems to systems and components of great importance, such as nuclear reactors, liquid rocket engines, heat exchangers, steam generators, evaporators, and various chemical process units. To avoid the occurrence of these highly undesirable events, it is essential to be able to predict accurately the onset of flow instabilities in such systems in terms of design parameters and operating conditions.

Of all the various types of two phase flow instabilities, an account of which can be found in the review paper by Bouré, Bergles and Tong [1], low frequency oscillations, i.e., density wave oscillations, are the most common type of instabilities encountered in practical systems. As a result, this particular type of instability has been studied extensively during the last fifteen years. But, in all the previous studies, including the latest one by Ishii [2], the effect of thermal non-equilibrium between the phases, i.e., the temperature difference between the liquid and the vapor phase, has been neglected. In reality, however, there are many instances where two phases can exist simultaneously even though their bulk, i.e., mean, temperatures are different. One of the most common examples is the subcooled boiling region in a heated boiling channel. Due to the thermal boundary layer near the heated surface,

Reproduced with permission of the copyright owner. Further reproduction prohibited without permission.

significant vapor generation can occur even though the local bulk temperature of the liquid is lower than the corresponding saturation temperature (or, the local vapor bulk temperature). This in effect, increases the length of the region occupied by the mixture; but at the same time reduces the local rate of vapor generation because part of the heat added is utilized to increase the bulk temperature of the liquid. Importance of this region in relation to the vapor void fraction, pressure drop, and overall performance of the system is well documented in the literature [3,4], and shall be discussed later in connection with the present problem.

From the theoretical as well as practical standpoint, therefore, stability analysis of a two-phase flow mixture cannot be regarded as complete unless the effect of thermal non-equilibrium is taken into consideration. The first logical step in that direction will be to determine the rate of vapor generation in a liquid whose bulk temperature is below saturation. This rate, which is different from that predicted under the assumption of thermodynamic equilibrium, must be described by an appropriate constitutive equation for evaporation. Furthermore, for the case of thermodynamic non-equilibrium it becomes necessary to determine the location (in the duct) where significant vapor generation starts. Several attempts, discussed later, have been made to determine this point of net vapor generation in the case of subcooled boiling. However, there is still a need for a better and, at the same time, simple criterion for the location of this point.

Reproduced with permission of the copyright owner. Further reproduction prohibited without permission.

In general, validity of any new theory can only be judged by comparing it with systematic, well-controlled experimental data. At present, there is a scarcity of such data on the onset of low frequency oscillations. To overcome this deficiency, a boiling loop has been built in the School of Mechanical Engineering at Georgia Institute of Technology. Therefore, it is now possible to obtain data on the onset of flow oscillations in a boiling channel and compare them with any theory.

I-2. Objectives of the Thesis

The present thesis has the following three objectives:

1. To generate experimental data on the onset of low frequency flow oscillations in a heated boiling channel with inlet subcooling.

2. To obtain a general criterion for the point of net vapor generation and develop a constitutive relation for the rate of vapor generation in subcooled boiling, i.e., thermal non-equilibrium region.

3. To include the effect of thermal non-equilibrium in the stability analysis and compare the new analysis with the latest equilibrium theory as well as with the experimental data to be obtained during the present research program.

I-3. Outline of the Thesis

The thesis is divided into two parts. In the first part, i.e., Chapter II, the experimental investigation has been reported. This consists of a brief description of the design, construction and instrumentation of the boiling loop, the procedure for obtaining data on the onset of flow oscillations, and a presentation of the data.

Reproduced with permission of the copyright owner. Further reproduction prohibited without permission.

The second part is devoted to the theoretical analysis of the problem. A brief review of the previous analytical work on low frequency oscillations is presented in Chapter III. In Chapter IV the effect of thermal non-equilibrium on vapor void fraction has been discussed. A new criterion for the point of net vapor generation has been found and a constitutive equation for the rate of vapor generation in the two phase mixture region has been developed. The formulation of the problem is given in Chapter V. The developments of Chapter IV have been utilized to obtain the characteristic equation for the system including the effects of thermal non-equilibrium between the phases. D-partition method is then used to determine the system stability boundary. In Chapter VI, the results of the new analysis have been compared with those of the latest equilibrium theory as well as with the experimental data presented in part one of the thesis. In Chapter VII, a simplified stability criterion for low subcooling number has been developed. The final chapter is devoted to conclusions.

Reproduced with permission of the copyright owner. Further reproduction prohibited without permission.

Part 1

EXPERIMENTAL PROGRAM

Reproduced with permission of the copyright owner. Further reproduction prohibited without permission.

CHAPTER II

EXPERIMENTAL INVESTIGATION

II-1. Description of the Boiling Loop

A schematic diagram of the boiling loop built in the School of Mechanical Engineering, Georgia Institute of Technology is shown in Figure 1. Although the loop is not restricted to any particular fluid, Freon-113 has been chosen as the operating fluid because of its low boiling point (117.6°F at atmospheric pressure) and low latent heat of vaporization (63.1 Btu/lbm at atmospheric pressure). It is, therefore, possible to obtain high exit quality with modest power input. Furthermore, Freon-113 is non-corrosive, non-toxic, non-flammable, and chemically stable.

As shown in Figure 1, an Ingersoll-Rand Inliner pump delivers all the freon to the test section and the by-pass. Except for the test section and a few secondary tubings, all the pipings are of standard hard drawn copper tubes of 2" and 1½" diameter. Most of the joints are brazed; but, in order to retain some degree of flexibility, several flanged connections and a fair amount of threaded unions have been used.

There is a preheater (American Standard BCF 605 Heat Exchanger), heated by saturated steam at 40 psig, at the entrance of the test section assembly. At the downstream of the preheater, there are two 1.5 kw Variac-controlled electric immersion heaters to enable a finer control of the inlet temperature.

Reproduced with permission of the copyright owner. Further reproduction prohibited without permission.

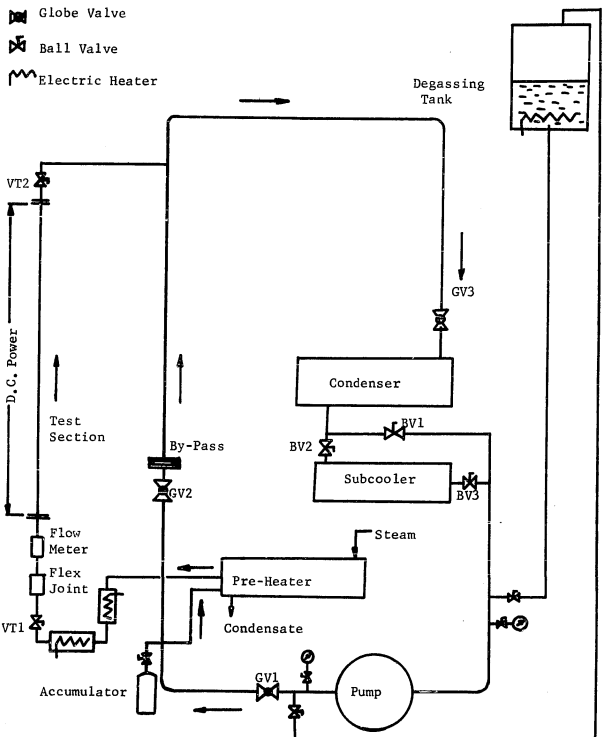

Figure 1. Schematic of the Boiling Loop

Reproduced with permission of the copyright owner. Further reproduction prohibited without permission.

The preheating system is followed by a ½" Jamesbury ball valve (VT1), a thermal expansion joint, a ½" ITT Barton turbine flow meter, the inlet flange assembly, the heated test section, the exit flange assembly, and another ½" Jamesbury ball valve (VT2). The by-pass, fitted with a globe valve (GV2) and an orifice flow meter, runs parallel to the test section. The exit end of the test section assembly merges with the by-pass and the entire freon flows to the condenser. An American Standard four pass heat exchanger no. 806 with 126 sq. ft of surface area has been used as the condenser. Freon enters the shell side whereas the cooling water passes through the tube side. In addition to the condenser, a subcooler of smaller capacity (American Standard BCF 605 Heat Exchanger) has been installed to facilitate operation at high inlet subcooling condition at the test section.

The system pressure and the flow can be adjusted to the desired values by regulating the valves GV1, GV3, and BV1 (or, BV3). The test section flow and/or by-pass flow ratio can be controlled by the globe valve GV2. Although the inlet and exit valves, i.e., VT1 and VT2, could be used to adjust the test section flow, it is not recommended during one set of experiment. This is because of the fact that a change in valve positions implies loss of geometrical similarity of the test section.

The heated portion of the test section is 9 ft long. It is a circular tube made of 304 stainless steel with outside diameter of 0.5" and inside diameter of 0.402". Two equivalent 304 stainless steel flanges are welded at the two ends of the tube. These flanges are connected to d.c. power supplied from a rectifier where regular a.c. power is transformed to low voltage and then rectified to low ripple direct current. The power

Reproduced with permission of the copyright owner. Further reproduction prohibited without permission.

supply is operated from a control panel, and is characterized by fine regulation and fast response which enable the system to reach its steady state condition rather quickly.

A degassing tank equipped with an immersion heater has been mounted at the top of the loop for several reasons. First, to provide sufficient net positive suction head (NPSH) for the pump; second, to accommodate volume expansion during heating; and third, to facilitate degassing of the test fluid after the initial charge.

The loop is provided with sufficient instrumentation to record pressure and temperature at various sections and/or locations of the loop. This shall be described in a later section.

The most serious problem encountered during the initial operation of the loop was the vibration transmitted from the pump-motor set. Several reasons were cited: for example, the compactness of the loop which corresponds to rather short distance between the test section and the pump-motor set, high center of mass of the pump-motor set, and relatively light construction of the supporting structure of the loop. In order to eliminate the vibration, the pump-motor set was first isolated from the floor by vibration isolators, and from the piping by two "Garflex" connectors. The fluid noises and the pressure fluctuations were effectively absorbed by a 2½ gallon "Greer" accumulator with Buna-N bladder charged to 50 psig with nitrogen. In addition, several pipe anchors with absorbing rubber pads were installed and the supporting structure was reinforced.

The operating range of the loop can be summarized as:

Reproduced with permission of the copyright owner. Further reproduction prohibited without permission.

Pressure	up to 240 psia
Total flow rate	0-100 gpm
Test section flow rate	0-5 gpm
Inlet subcooling	0-250°F
Test section power	0-100 kw
Input heat flux	0-730 watts/in^{2}

II-2. Details of the Test Section Assembly

As stated earlier, the test section assembly consists of an inlet valve (VT1), a flexible or thermal expansion joint, a turbine flow meter, an inlet flange assembly, the heated test section, an exit flange assembly, and an exit valve (VT2). The height of the entire assembly is 12 feet and it is shown in Figure 2.

Inlet and exit throttlings are given by the $\frac{1}{2}$" Jamesbury ball valves VT1 and VT2. The thermal expansion joint with a stainless steel internal bellow can absorb $1\frac{1}{4}$" of compression and $\frac{1}{4}$" of extension. During the initial operation of the loop the heated test section buckled even though the expansion joint was in line. The problem was solved by pulling the inlet flange assembly down by two tension springs each loaded to 70 lbf.

The turbine flow meter measures the flow rate through the test section. A turbine flow meter was chosen because of its quick response to a slight variation in flow.

Each of the inlet and exit flange assemblies has a gland for immersion thermocouple and a pressure tap. The pressure tap can be used either for the measurement of system pressure or for differential pressure measurement with other taps. These flange assemblies are holding the

Reproduced with permission of the copyright owner. Further reproduction prohibited without permission.

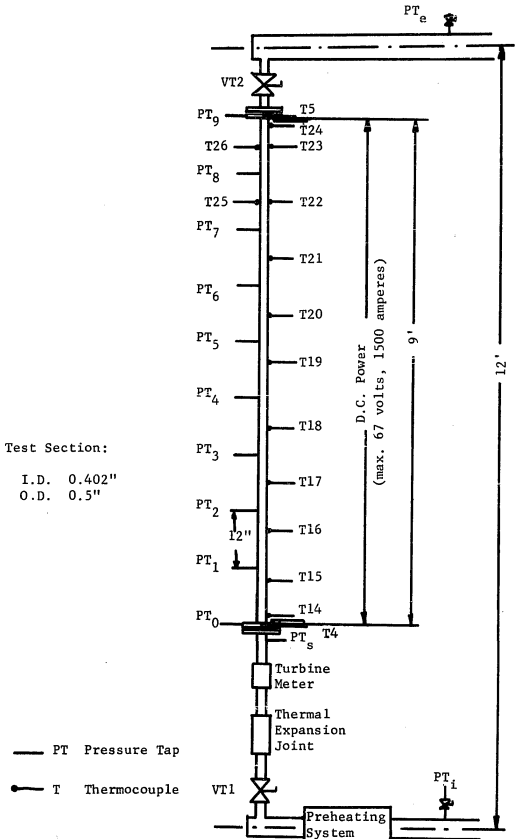

Figure 2. Details of the Test Section Assembly

Reproduced with permission of the copyright owner. Further reproduction prohibited without permission.

heated test section in between them. The test section is a 9 feet long circular tube made of stainless steel with 0.5" O. D. and 0.402" I. D. Two stainless steel flanges are welded at the two ends of the tube and these are connected to d.c. power. The tube itself works as the electrical resistor (0.49×10^{-2} Ω/ft) and because of constant wall thickness (0.049") the axial heat flux distribution is essentially uniform. Maximum power input is 100 kw (67 V and 1500 amps), which corresponds to a maximum heat flux of 730 watts/in^2.

There are eight pressure taps (PT1 through PT8), each 12" apart, on the test section. First, 2" long stainless steel tubes of ¼" O. D. and 3/32" I. D. were welded to the test section. The actual taps were made with 1/16" diameter drill piercing through the test section wall along the center line of ¼" O. D. tubes. Each of the pressure taps is connected to a pressure transducer or a pressure gauge with ¼" O. D. nylon tubes rated to 600 psig.

Copper-Constantan thermocouples have been used for temperature measurement. Locations of most of the thermocouples are shown in Figure 2 and will be discussed in more detail in the following section.

II-3. Loop Instrumentation

The loop is equipped with a sufficient number of measuring instruments to study steady state as well as non-steady behavior of two-phase flow system. Simple instruments have been used to measure the flow rate, pressure, temperature, and power input to the test section. Arrangements have been made so that the flow rate through the test section and the pressure drop across the test section can be recorded simultaneously. Under

Reproduced with permission of the copyright owner. Further reproduction prohibited without permission.

the transient or the oscillatory flow conditions this arrangement provides data on amplitude and frequency of oscillations as well as on the phase angle shift between the flow rate and the pressure drop. Such data are important for studies of dynamic behavior of two-phase flow system.

The details of the instruments used are given below.

Flow Measurement

Flow through the test section is measured with an ITT Barton ½" stainless steel turbine meter (series 7284) of 10423.9 pulses/gallon. The output signal from the meter is fed into an ITT Barton flow rate indicator (series 881). The indicator was calibrated first with internal 120 Hz calibration frequency. Linearity of the indicator was then checked with a frequency generator and the full scale flows for each of the three ranges of the indicator were established. For continuous trace of the test section flow, the output signal is fed into a Hewlett Packard 2 channel 7100 BM strip chart recorder. The signal could also be fed into an oscilloscope. The accuracy of the flow measurement is ± 1% of the full scale flow.

The by-pass flow is measured from the pressure drop across a 1.6" I. D. orifice plate installed in the by-pass line. The pressure drop for this purpose is measured in a Meriam U-tube mercury manometer.

Pressure Measurement

Standard Bourdon tube gauges of range 0-300 psig and 0-200 psig have been used for pressure measurement at the pump discharge and pump suction respectively. A test gauge (Acco Helicoid) of range 0-300 psig with an accuracy of ± ½ of 1% has been installed to measure the pressure

Reproduced with permission of the copyright owner. Further reproduction prohibited without permission.

at the entrance of the heated test section. This pressure is considered to be the system pressure.

Pressure drops across the inlet (between PT_i and PT_o) and the exit (between PT_9 and PT_e) section of the test section assembly are measured with two ITT Barton differential pressure indicators (model 227), each having a differential pressure range of 0-25 psi. The indicator housing is made of forged brass and can withstand a pressure of 500 psig. A 3/4" O. D. beryllium copper bellow is used as the sensing device.

A Statham differential strain-gauge type pressure transducer (model PM 399 TC ± 50-350) has been used for pressure drop measurement across the reference pressure tap (PT_o) and any other pressure tap on the heated test section. The transducer has a differential pressure range of ± 50 psi and a calibration factor of 0.5515 millivolt/psi. The output is fed into the same Hewlett Packard strip chart recorder where the pressure drop across the desired taps can be recorded simultaneously with the test section flow rate. A schematic of the entire arrangement is shown in Figure 3.

Temperature Measurement

Two copper-constantan immersion thermocouples (T4 and T5) with 1/16" O. D. stainless steel sheaths are inserted through the glands provided at the inlet and exit flange assemblies. These thermocouples are used to measure fluid temperature at the inlet and the exit of the heated test section. These two thermocouples have been specially calibrated using a constant temperature bath. The accuracy of temperature measurement with the above thermocouples is ± 1°F.

As shown in Figure 2, a number of copper-constantan thermocouples have been mounted on the outside wall of the test section. A special

Reproduced with permission of the copyright owner. Further reproduction prohibited without permission.

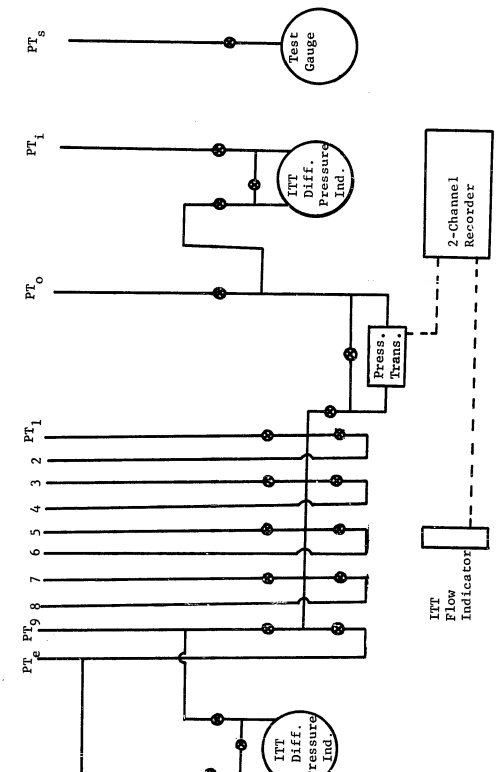

Figure 3. Schematic of the Pressure and Flow Measuring Arrangement

Reproduced with permission of the copyright owner. Further reproduction prohibited without permission.

binding mixture (Sauereisen Insa-Lute adhesive cement) has been used to hold the thermocouple beads at proper positions and care has been taken to ensure no electrical contact between a bead and the electrically heated test section. By knowing the outside wall temperature and the heat generation in the tube wall due to resistive heating, it is possible to calculate the inside wall temperature, and thence the two phase heat transfer coefficient.

Two thermocouples (T25 and T26) have been mounted near the exit of the test section to check the dry-out condition. Output from these thermocouples are fed into two millivoltmeters, each of range 0-25 mV, mounted on the instrument panel. Input power is lowered if any of these meters reads more than 20 mV, i.e., if the wall temperature exceeds 750°F.

Several other thermocouples are used to check/measure temperature at various locations of the loop like, at the pump discharge (T3), at the degassing tank (T6), at cooling water inlet and outlet (T9 and T10), at the power cable jacket outlet (T12), etc. All thermocouple outputs (except for those of T25 and T26) are fed into a calibrated 24-channel Honeywell recorder.

Power Measurement

Power input to the test section is measured with a voltmeter of range 0-100 V, and an ammeter of range 0-1500 amps. A digital voltmeter is also installed on the instrument panel for a better reading of the voltage across the test section. From a number of steady-state single-phase heat balances, the accuracy of power measurement has been found to be ± 4% of the measured power.

Reproduced with permission of the copyright owner. Further reproduction prohibited without permission.

II-4. Procedure of the Experiment

The purpose of the present experimental program is to obtain data on the onset of thermally induced flow oscillations. These data are acquired in such a way that the experimental results can be compared directly with the theoretical predictions of [2] and the new analysis presented in the second part of the thesis. The procedure of the experiment is:

1. Select a system pressure.

2. Set the inlet and exit throttling valves (VT1 and VT2) at some particular positions. This automatically specifies a particular system geometry and must not be disturbed during one set of experiments. The values of inlet and exit orifice coefficients (k_i and k_e) are determined from steady state adiabatic experiments which shall be discussed later.

3. Select an inlet flow velocity through the test section, i.e., a flow Reynolds number. This should also be kept constant during one set of data.

4. Establish an inlet temperature (i.e., inlet subcooling) by adjusting the preheating system.

5. Start increasing power input to the test section in small steps. Sufficient time should be allowed in between two successive steps so that the true nature (steady state or oscillatory) of the system can be understood. Power is increased until sustained oscillation is observed in the recorder.

At the advent of two phase mixture in the test section, the inlet flow might change due to different pressure drop characteristics. In that case, a slight adjustment of the by-pass valve (GV2) becomes necessary

Reproduced with permission of the copyright owner. Further reproduction prohibited without permission.

to maintain the chosen inlet flow through the test section. Because of high by-pass to test section flow ratio (15 to 20) this adjustment does not affect the condition (simulation) of parallel channel instability with constant pressure drop across the channels. The power input corresponding to the inception (onset) of flow oscillation is determined from the trace of the test section flow, and the procedure for this shall be discussed shortly. Heat loss to the surroundings shall also be taken into account.

By repeating steps 4 and 5, one can determine the relationship between inlet subcooling and power required to initiate oscillation for a particular system pressure, a particular system geometry (k_i and k_e) and a particular Reynolds number. This constitutes one set of instability data. Several such sets are required to study the effect of system pressure, flow Reynolds number, inlet and exit restriction on the stability of the system.

Determination of Inlet and Exit Orifice Coefficients

In the theoretical analysis, all the equipment at the upstream of the heated test section, i.e., the preheating system, inlet valve VT1, expansion joint, etc., is lumped together and considered as an inlet orifice. Similarly, the equipment at the downstream, i.e., the valve VT2 and the short piping merging the by-pass, is considered as an exit orifice. Due to the presence of complicated components like the immersion heater, flexible joint, turbine flow meter, etc., it is almost impossible to determine theoretically the values of inlet and exit orifice coefficients. Therefore, these are evaluated experimentally. The valves VT1 and VT2 are set at a particular position; the flow and the pressure drop excluding gravity are measured without heat addition to the test section. The

Reproduced with permission of the copyright owner. Further reproduction prohibited without permission.

values of k_i and k_e are then determined from the following relations:

$$\left.\begin{aligned} \Delta P_i &= k_i \rho_f v_f^2 \\ \Delta P_e &= k_e \rho_f v_f^2 \end{aligned}\right\} \quad (2.1)$$

Determination of the Onset of Oscillation

A typical trace of the test section flow is shown in Figure 4. It can be seen that as power is increased the average fluctuation of the flow is also increased. In fact, it is almost impossible to pin-point the onset of flow oscillation just by looking at the flow indicator or the trace. The problem is solved by plotting the average amplitude of the flow fluctuation against the power supplied to the test section and then determine the point of inception of the oscillation as shown in Figure 5. The frequency of oscillation is also found from the flow trace.

In order to determine the net power to the fluid, it is now necessary to account for the heat loss from the test section to the surroundings.

Determination of Heat Loss

As shown in Figure 2, there are several thermocouples mounted on the outside surface of the test section. Temperatures of those points are continually recorded on a Honeywell recorder. From this the average outside surface temperature of the test section, $T_{w,av}$, can be determined. The room temperature, T_{amb}, is also noted during the experiment. The boiling loop is housed in a large room, and only mechanisms of heat loss are natural convection and radiation. Dr. M. Ishii prepared a graph

Reproduced with permission of the copyright owner. Further reproduction prohibited without permission.

All chart speeds 0.5 cm/sec.

4.425 kw

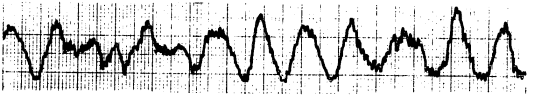

5.850 kw

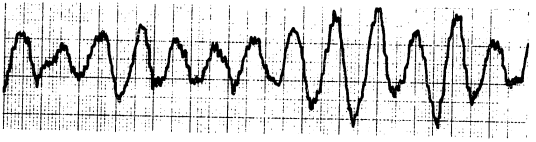

6.825 kw

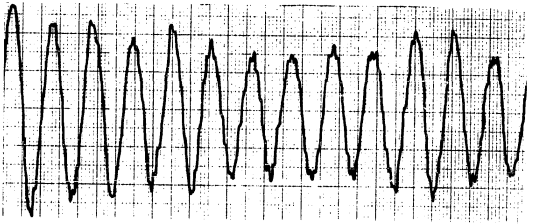

7.100 kw

Figure 4. A Typical Inlet Flow Trace with Increasing Power Input (Run No. OT 11, Set No. IV)

Reproduced with permission of the copyright owner. Further reproduction prohibited without permission.

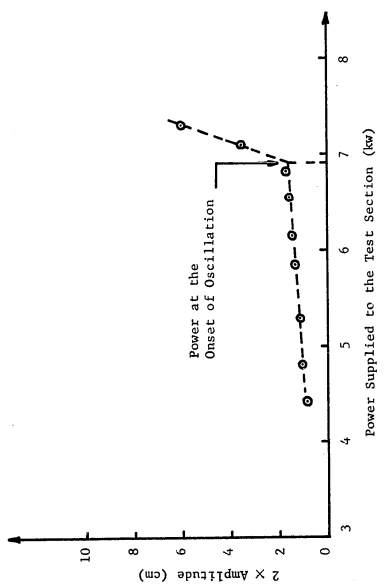

Figure 5. Determination of the Point of Inception of Flow Oscillation
(Run No. QT11, Set No. IV)

Reproduced with permission of the copyright owner. Further reproduction prohibited without permission.

showing the combined (free convection plus radiation) heat transfer coefficient, h_t, from the test section to the surrounding air. The graph is reproduced in Figure 6, and the heat loss, $\dot{Q}_{hl}$, corresponding to the point of inception of flow oscillation is calculated from the following:

$$\dot{Q}_{hl} = A_s h_t (T_{w,av} - T_{amb}) \tag{2.2}$$

where A_s is the outside surface area of the test section.

The amount of heat loss is subtracted from the measured power input to determine the actual power input at the onset of oscillation. In the following section the experimental data obtained during the present investigation shall be presented.

II-5. Experimental Results

Seven sets of experiments have been conducted to see the effects of various parameters. The results are presented in Tables 1 through 7. Sets I through III are at three different pressures, and sets IV through VI are at three different Reynolds numbers. Sets I and IV show the effect of inlet restriction, whereas sets I and VII show the effect of exit restriction. Properties of Freon-113 are taken from [5,6,7]. Discussion of these experimental results and comparison with theoretical predictions shall be deferred until Chapter VI. But, a few comments and observations seem to be appropriate in the present context.

Only one mode of oscillations could be detected from the present inlet flow traces. The time period of oscillation was found to be in the order of transit time through the test section. Attempts were made to

Reproduced with permission of the copyright owner. Further reproduction prohibited without permission.

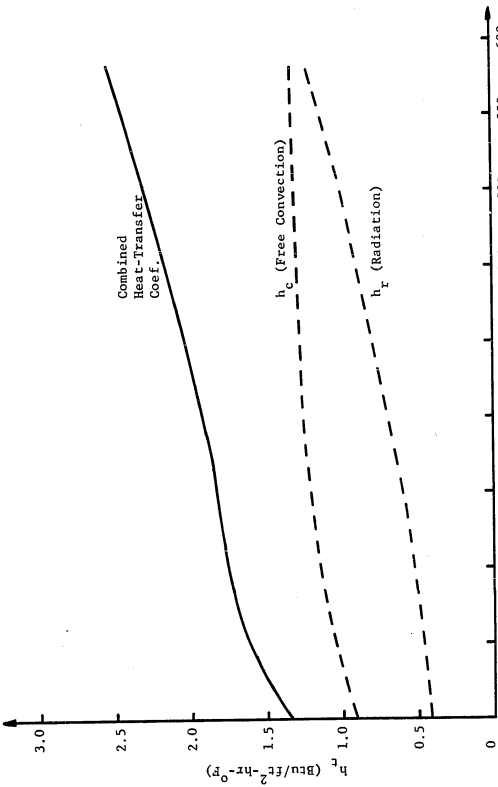

Figure 6. Heat Transfer Coefficient from the Test Section to the Surrounding Air

Reproduced with permission of the copyright owner. Further reproduction prohibited without permission.

Reproduced with permission of the copyright owner. Further reproduction prohibited without permission.

Table 1. Results for Set No. I

Run No.	Inlet Temp. T_i (^oF)	Inlet Subcooling Δi_{sub} Btu/lbm	Measured Power at the onset of Oscillation Btu/sec	Heat Loss Btu/sec	Net Power $\dot{Q}_w$ Btu/sec	Frequency of Oscillation f cycle/sec
OT 5	281	4.9	7.018	0.177	6.841	0.833
OT 4	279	5.6	6.165	0.135	6.030	0.708
OT 3	272.5	7.2	5.880	0.137	5.743	0.590
OT 2	269.5	8.2	4.268	0.135	4.133	0.440
OT 1	261	10.3	4.505	0.137	4.368	0.415
OT 9	247	13.7	5.405	0.135	5.270	0.361
OT 8	235	16.5	6.022	0.137	5.885	0.354
OT 7	228.5	18.3	6.733	0.138	6.595	0.340
OT 6	219	20.3	7.587	0.150	7.437	0.334
OT 10	206	23.3	8.630	0.168	8.462	0.333

Note: System Pressure: 175 psia; Inlet Velocity: 3.21 ft/sec; Reynolds Number: 5.94×10^4; Inlet Value 100% open: $k_i = 2.85$; and Exit Value 100% open: $k_e = 2.03$.

Reproduced with permission of the copyright owner. Further reproduction prohibited without permission.

Table 2. Results for Set No. II

Run No.	Inlet Temp. T_i (^oF)	Inlet Subcooling Δi_{sub} Btu/lbm	Measured Power at the onset of Oscillation Btu/sec	Heat Loss Btu/sec	Net Power Q_W Btu/sec	Frequency of Oscillation f cycle/sec
OT 55	285	7.8	4.220	0.142	4.078	0.448
OT 54	281	8.9	4.457	0.142	4.315	0.433
OT 53	275.5	10.3	4.742	0.143	4.599	0.434
OT 52	270	11.7	5.122	0.143	4.979	0.405
OT 51	263	13.4	5.405	0.148	5.257	0.386
OT 59	242.5	18.6	7.113	0.157	6.956	0.339
OT 58	234	20.6	7.967	0.173	7.794	0.369
OT 57	225	22.7	8.677	0.203	8.474	0.350
OT 56	218	24.3	9.057	0.173	8.884	0.334
OT 60	203	27.7	10.052	0.222	9.830	0.324

Note: System Pressure: 200 psia; Inlet Velocity: 3.07 ft/sec; Reynolds Number: 5.9×10^4; Inlet Valve 100% open: $k_i = 2.85$; and Exit Valve 100% open: $k_e = 2.03$.

Reproduced with permission of the copyright owner. Further reproduction prohibited without permission.

Table 3. Results for Set No. III

Run No.	Inlet Temp. T_i (°F)	Inlet Subcooling Δi_{sub} Btu/lbm	Measured Power at the onset of Oscillation Btu/sec	Heat Loss Btu/sec	Net Power Q_w Btu/sec	Frequency of Oscillation f cycle/sec
OT 73	273	3.1	7.113	0.140	6.973	0.912
OT 72	269	4.2	6.448	0.132	6.316	0.770
OT 71	263	5.7	5.832	0.133	5.699	0.610
OT 77	253	8.1	4.600	0.125	4.475	0.456
OT 76	245	10.1	4.837	0.127	4.710	0.418
OT 75	236	12.2	5.548	0.128	5.420	0.396
OT 74	227.5	14.3	6.212	0.128	6.084	0.381
OT 80	224	15.2	6.307	0.130	6.177	0.359
OT 79	215	17.2	6.828	0.133	6.695	0.352
OT 78	209	18.7	7.350	0.133	7.217	0.344

Note: System Pressure: 150 psia; Inlet Velocity: 3.34 ft/sec; Reynolds Number: 5.9×10^4; Inlet Valve 100% open: $k_i = 2.85$; and Exit Valve 100% open: $k_e = 2.03$.

Reproduced with permission of the copyright owner. Further reproduction prohibited without permission.

Table 4. Results for Set No. IV

Run No.	Inlet Temp. T_i (^oF)	Inlet Subcooling Δi_{sub} Btu/lbm	Measured Power at the onset of Oscillation Btu/sec	Heat Loss Btu/sec	Net Power $\dot{Q}_W$ Btu/sec	Frequency of Oscillation f cycle/sec
OT 15	278	5.9	7.967	0.187	7.780	0.788
OT 14	274.5	6.7	6.923	0.180	6.743	0.758
OT 13	268	8.4	6.497	0.140	6.357	0.638
OT 12	262	9.8	5.975	0.140	5.835	0.475
OT 11	260	10.5	6.448	0.143	6.305	0.479
OT 19	250	12.8	6.022	0.135	5.887	0.410
OT 18	242	14.9	6.497	0.142	6.355	0.401
OT 17	233	17.0	6.970	0.142	6.828	0.378
OT 16	225	18.8	7.302	0.142	7.160	0.366
OT 20	212	22.0	8.488	0.165	8.323	0.342

Note: System Pressure: 175 psia; Inlet Velocity 3.21 ft/sec; Reynolds Number: 5.94×10^4; Inlet Valve 60% open: $k_i = 6.55$; and Exit Valve 100% open: $k_e = 2.03$.

Reproduced with permission of the copyright owner. Further reproduction prohibited without permission.

Table 5. Results for Set No. V

Run No.	Inlet Temp. T_i (^oF)	Inlet Subcooling Δi_{sub} Btu/lbm	Measured Power at the onset of Oscillation Btu/sec	Heat Loss Btu/sec	Net Power $\dot{Q}_w$ Btu/sec	Frequency of Oscillation f cycle/sec
OT 25	280.5	5.3	3.603	0.138	3.465	0.540
OT 24	277.5	6.2	3.793	0.138	3.655	0.532
OT 23	270	7.9	3.983	0.138	3.845	0.492
OT 22	262	10.0	4.410	0.147	4.263	0.467
OT 21	254.5	11.8	4.647	0.147	4.500	0.397
OT 29	253.5	12.2	4.742	0.143	4.599	0.383
OT 28	241	15.2	5.405	0.143	5.262	0.359
OT 27	230	17.8	5.927	0.143	5.784	0.328
OT 26	221	19.7	6.497	0.155	6.342	0.348
OT 30	209	22.7	7.587	0.152	7.435	0.330

Note: System Pressure: 175 psia; Inlet Velocity: 2.37 ft/sec; Reynolds Number: 4.34×10^4; Inlet Valve 60% open: $k_i = 6.55$; and Exit Valve 100% open: $k_e = 2.03$.

Reproduced with permission of the copyright owner. Further reproduction prohibited without permission.

Table 6. Results for Set No. VI

Run No.	Inlet Temp. T_i (^oF)	Inlet Subcooling Δi_{sub} Btu/lbm	Measured Power at the onset of Oscillation Btu/sec	Heat Loss Btu/sec	Net Power Q_w Btu/sec	Frequency of Oscillation f cycle/sec
OT 34	276.5	6.2	11.760	0.263	11.497	0.868
OT 33	272.5	7.2	9.483	0.228	9.255	0.720
OT 32	269	8.2	9.008	0.195	8.813	0.650
OT 31	264	9.5	10.195	0.192	10.003	0.652
OT 38	247.5	13.5	11.143	0.197	10.946	0.556
OT 37	238	15.8	11.855	0.193	11.662	0.527
OT 36	230.5	17.6	12.945	0.223	12.722	0.516
OT 35	227.5	18.3	13.182	0.222	12.960	0.447
OT 40	215	21.2	14.082	0.225	13.857	0.423
OT 39	210	22.4	14.605	0.230	14.375	0.412

Note: System Pressure: 175 psia; Inlet Velocity: 4.88 ft/sec; Reynolds Number: 8.94×10^4; Inlet Valve 60% open: $k_i = 6.55$; and Exit Valve 100% open: $k_e = 2.03$.

Reproduced with permission of the copyright owner. Further reproduction prohibited without permission.

Table 7. Results for Set No. VII

Run No.	Inlet Temp. T_i (^oF)	Inlet Subcooling Δi_{sub} Btu/lbm	Measured Power at the onset of Oscillation Btu/sec	Heat Loss Btu/sec	Net Power $\dot{Q}_W$ Btu/sec	Frequency of Oscillation f cycle/sec
OT 45	284.5	4.0	5.595	0.140	5.455	0.646
OT 44	280	5.4	4.457	0.135	4.322	0.534
OT 43	273	7.1	3.935	0.137	3.798	0.436
OT 42	268.5	8.3	4.125	0.135	3.990	0.418
OT 41	262.5	9.9	4.315	0.130	4.185	0.378
OT 49	245.5	14.1	5.500	0.137	5.363	0.320
OT 48	238	15.9	6.183	0.140	6.043	0.314
OT 47	228	18.3	6.970	0.145	6.825	0.292
OT 46	221	19.7	7.350	0.143	7.207	0.288

Note: System Pressure: 175 psia; Inlet Velocity: 3.21 ft/sec; Reynolds Number: 5.94×10^4; Inlet Valve 100% open: $k_i = 2.85$; and Exit Valve 55% open: $k_e = 10.66$.

increase the input power beyond the first mode of oscillation; but vigorous oscillations endangered the entire system and thus put a limit on the input power. Therefore, no higher order oscillations, as reported in [8], could be detected during the present program. However, the time period of oscillation clearly indicates that the instabilities are caused by the time delays and, therefore, can be referred to as density wave oscillations.

A few simultaneous traces of inlet flow and system (test section assembly) pressure drop have been presented in Figures 7 through 10. It can be seen that there is a time lag between the system pressure drop (cause) and the inlet flow (effect). The phase shift is between 90°-180° in Figures 7 and 8, but between 270°-360° in Figure 9. Inlet subcooling, however, does not have any appreciable effect on the phase shift, as seen from Figures 9 and 10.

During the flow oscillation the wall temperature was also observed through the two millivoltmeters mounted on the instrument panel. No appreciable fluctuation could be seen in any of these two meters. Therefore, flow oscillations do not necessarily cause a wall temperature oscillation or excursion.

The uncertainty and the repeatability of the experimental data have been discussed in Appendix D and E respectively.

Reproduced with permission of the copyright owner. Further reproduction prohibited without permission.

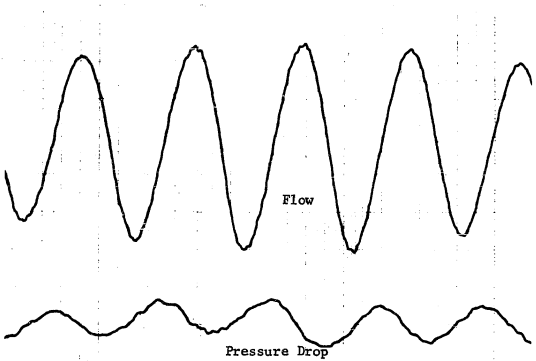

Time →

(Chart speed: 2.5 cm/sec, Δi_{sub} = 6.2 Btu/lbm)

Figure 7. Trace of Inlet Flow and System Pressure Drop (Run No. OT 34, Set No. VI)

Reproduced with permission of the copyright owner. Further reproduction prohibited without permission.

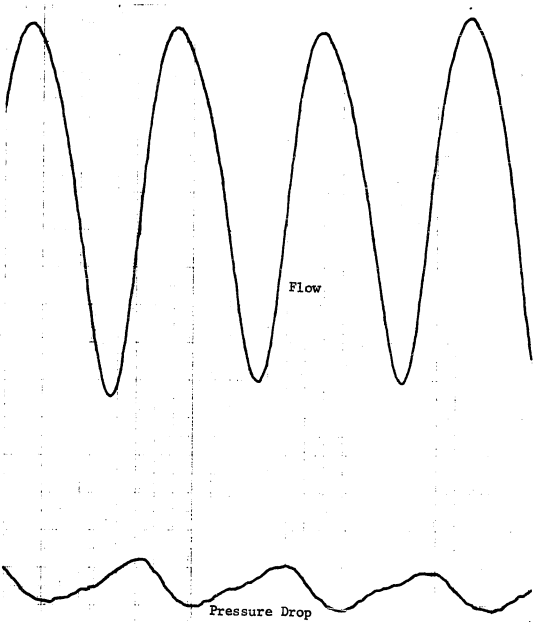

(Chart speed: 2.5 cm/sec, Δi_{sub} = 4.0 Btu/lbm)

Figure 8. Trace of Inlet Flow and System Pressure Drop (Run No. OT 45, Set No. VII)

Reproduced with permission of the copyright owner. Further reproduction prohibited without permission.

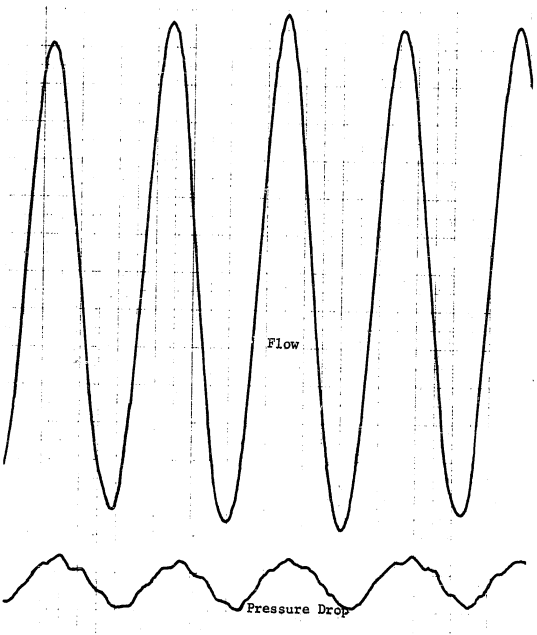

(Chart speed: 2.5 cm/sec, Δi_{sub} = 5.9 Btu/lbm)

Figure 9. Trace of Inlet Flow and System Pressure Drop (Run No. 0T 15, Set No. IV)

Reproduced with permission of the copyright owner. Further reproduction prohibited without permission.

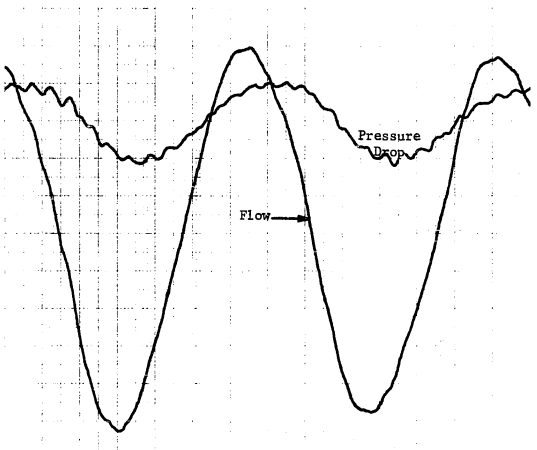

Time →

(Chart speed: 2.5 cm/sec, Δi_{sub} = 18.8 Btu/lbm)

Figure 10. Trace of Inlet Flow and System Pressure Drop (Run No. OT 16, Set No. IV)

Reproduced with permission of the copyright owner. Further reproduction prohibited without permission.

Part 2

THEORETICAL ANALYSIS

Reproduced with permission of the copyright owner. Further reproduction prohibited without permission.

CHAPTER III

STATE OF THE ART

III-1. Types of Instabilities

Thermally induced two-phase flow instabilities can be divided into two main categories: excursive and oscillatory.

Excursive instability, commonly known as Ledinegg instability, is characterized by a sudden non-repetitive change in the flow rate from one steady state condition to another. This type of instability can occur if the slope of the system pressure drop versus flow rate curve (demand curve) is algebraically smaller than that of the pump pressure drop versus flow rate curve (supply curve).

The oscillatory types of instabilities are rather complicated dynamic phenomena which can be subdivided into the following:

a) Instability due to sudden change of flow regime: Jeglic and Grace [9] observed that the flow oscillations were accompanied by quick transition from bubbly flow to annular flow regime. Moreover, the interface between these two regimes had been oscillating up and down the test section with the same frequency as the flow oscillation.

b) Acoustic instability: This type of instability is characterized by the high frequency (10-100 cycles/sec) of oscillation. The time period of oscillation is of the same order of magnitude as the time required for a pressure wave to travel through the system.

Reproduced with permission of the copyright owner. Further reproduction prohibited without permission.

c) Density wave instability: This is characterized by the low frequency (~ 1 cycle/sec) of oscillation. The time period is of the same order of magnitude as the time required for a kinematic (continuity) wave to travel through the system. As mentioned before, this is the type of instability that is encountered in practical system most frequently [1], and is the topic for the present thesis.

III-2. Previous Work on Low Frequency Oscillations

In general two approaches have been followed in the stability analysis of two-phase flow systems. The first is based on phenomenological models which are obtained from the assumed similarity with a simple lumped parameter mechanical system or an electric circuit having excitations. The second approach is to formulate the problem from the conservation laws for the mixture.

Because of its simplicity, many of the earlier studies belong to the first group. However, since the models are not based on conservation laws, one must supply several experimental coefficients or correlation functions into these formulations. Therefore, the applicability of their results is severely restricted.

Two models, a homogeneous flow model and a slip flow model, have been considered in the studies based on conservation equations. In homogeneous flow model the relative velocity between the phases is neglected, whereas in the slip flow model this important characteristic of two phase flow systems is taken into account.

Besides this classification into homogeneous and slip flow model,

Reproduced with permission of the copyright owner. Further reproduction prohibited without permission.

generally two distinct methods have been used to obtain a solution of the instability problem. In the first, the system of partial differential equations is linearized by assuming small disturbance around a steady state. The response of the system to various perturbations, as well as the stability criterion, are then obtained by using standard techniques of control theory. The second method is based on a numerical solution whereby the set of non-linear partial differential equations is solved by numerical technique.

Teletov and Serov [10] were apparently the first to formulate the dynamic problem of two-phase flow system. They realized that for low frequency oscillation, mixture density was a function of mixture enthalpy only, and not of both enthalpy and pressure. Therefore, they were able to decouple the momentum equation from the continuity and energy equation. About ten years later, Serov, et al. [11,12] integrated the momentum equation and obtained the characteristic equation for a distributed parameter system. They took into account the variation of inlet flow and heat transfer coefficient, but neglected the displacement of boiling boundary. The resulting characteristic equation was a fifth order polynomial with two time delays. This was solved for the stability boundary in a simplified form by the D-partition method.

Wallis and Heasley [13] used a model similar to that of Serov. Using Lagrangian co-ordinates, they integrated the continuity and energy equation with a disturbed inlet flow. The characteristic equation, however, was obtained from the momentum balance for a lumped parameter system, and the Nyquist criterion was used to discuss the stability of the system.

Reproduced with permission of the copyright owner. Further reproduction prohibited without permission.

Finally, Bouré [14,15] integrated the continuity, energy and the momentum equation to obtain a characteristic equation for a distributed parameter system. The coefficients of the polynomial differ from those of Serov, et al. [11,12] because the analysis of Bouré took into account the variation of inlet flow and the displacement of the boiling boundary (which was neglected by Serov), but omitted the wall heat capacity (which was considered by Serov). The important point, however, is that all the analyses discussed above are limited to homogeneous flow with thermodynamic equilibrium between the phases.

Unfortunately, in most of the two-phase flow systems the effect of relative velocity between the phases and the effect of thermodynamic non-equilibrium cannot be neglected a priori. In slip flow models the effect of relative velocity is taken into consideration. But as pointed out in [16], the traditional slip flow models are not formulated with respect to the center of mass of the mixture, and, therefore, those cannot be used to analyze and predict correctly dynamic phenomena in a system where the relative velocity between the phases is important. Also, the authors [17,18] who used the traditional slip model, had to use three different expressions for the mixture density as well as two different expressions for the enthalpy of the mixture. Apart from this basic shortcoming of traditional slip model formulation, almost all slip models have been solved directly by computers. This approach, besides being expensive for parametric studies, does not provide an insight into the physical aspects of the problem.

Zuber [16] was the first to formulate the problem in terms of the center of mass, taking into consideration the effects of relative velocity

Reproduced with permission of the copyright owner. Further reproduction prohibited without permission.

between the two phases and the effects of thermodynamic non-equilibrium condition. The formulation consists of four field equations (the continuity, momentum and energy equation for the mixture and the continuity equation for the vapor phase expressed in terms of kinematic wave) and seven constitutive equations. By using small perturbation on the variables, the set of equations for a system in thermal equilibrium and with constant heat flux has been integrated analytically resulting in a characteristic equation for a distributed system.

Following the formulation of Zuber [16], Ishii [2,19] obtained the important similarity groups, namely subcooling number, phase change number, drift number, etc., which govern the kinematics and dynamics of the system. The formulation of Ishii was general enough to incorporate the effects of non-uniform heat flux and thermal non-equilibrium condition; but, the characteristic equation obtained was limited to the case of uniform heat flux and thermal equilibrium condition between the phases. The major contribution of the study was, however, to obtain the system stability boundary in the subcooling number versus phase change number plane. Ishii also obtained a simple stability criterion for high subcooling number [2]. The importance of relative velocity between the phases and various two-phase friction factor models has also been studied. But, as mentioned earlier, no attempt has been made to include the effect of thermal non-equilibrium between the phases in the stability analysis.

Reproduced with permission of the copyright owner. Further reproduction prohibited without permission.

CHAPTER IV

EFFECT OF THERMAL NON-EQUILIBRIUM ON VAPOR VOID FRACTION

IV-1. Description of a Boiling Channel

For the formulation of the present problem, it is important to understand the physical aspects of thermodynamic non-equilibrium in a two phase flow system.

A typical boiling channel subjected to an uniform heat flux distribution is shown in Figure 11. Liquid enters the channel at a temperature below the corresponding saturation temperature. As a result of heat addition, the bulk temperature of the liquid as well as the temperature of the wall increases along the direction of the flow. It is well known that even for heterogeneous nucleation of bubbles, a certain amount of liquid superheating is needed around the bubble. Therefore, as soon as the inside wall temperature exceeds the corresponding saturation temperature by the required amount, bubbles start to nucleate at the wall even though the liquid bulk temperature can be well below the saturation temperature. This corresponds to the point A in Figure 11. The wall temperature beyond that point remains almost constant.

Because of uniform heat flux distribution the liquid bulk temperature starts to increase linearly. This would increase linearly up to the saturation value if all the heat added to the system would go to raise the temperature of the liquid only. After that, the liquid bulk temperature would remain constant at the saturation value, and all the heat added

Reproduced with permission of the copyright owner. Further reproduction prohibited without permission.

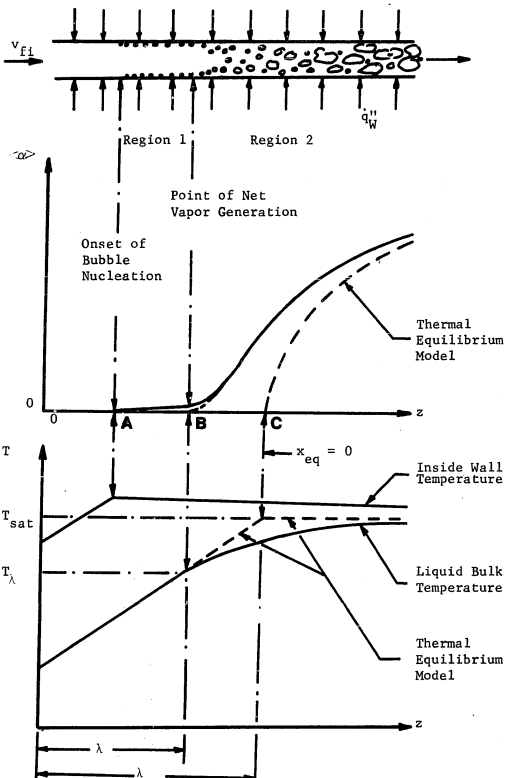

Figure 11. A Typical Boiling Channel

Reproduced with permission of the copyright owner. Further reproduction prohibited without permission.

would go to generate vapor. This is the thermal equilibrium model and is shown by the dotted lines in Figure 11. It should be noticed that according to the equilibrium model vapor generation starts from point C.

In reality, however, bubble generation starts upstream, i.e., at point A. At this point the liquid bulk temperature is very much below the saturation temperature, i.e., the subcooling is rather high. However, the wall temperature is above saturation so that a thin superheated liquid film exists next to the wall. It is in this thin layer that the bubbles nucleate, grow, and eventually collapse after they penetrate into the subcooled liquid region. Therefore, the vapor void fraction cannot increase significantly. However, as the subcooling decreases along the direction of the flow, the bubbles grow, leave the surface and move to the core of the flow. This phenomenon gives rise to an increase in vapor void fraction. From Figure 11 it can be seen that the void fraction profile increases rapidly from a point B, which is somewhere in between the points A and C. The liquid bulk temperature, however, is lower than what is predicted by the equilibrium model because a part of the heat added to the system generates vapor right from the point A. Eventually, at a considerable distance from point C, the liquid bulk temperature as well as the void fraction profile approach the equilibrium model. It should be noticed that at point C, where the equilibrium model predicts a zero value for void fraction, the actual void fraction, due to the effect of thermal non-equilibrium, can be as high as 30 to 40 percent. Therefore, the actual mixture density at point C can be 30 to 40 percent lower than the value predicted by the equilibrium model. Moreover, the length of the two-phase mixture region is, in fact, longer than that predicted by the equilibrium

Reproduced with permission of the copyright owner. Further reproduction prohibited without permission.

model.

For a correct analysis of the problem of flow instability including the effect of thermal non-equilibrium, it is important that correct mixture density is used. Several experimental investigations [20,21,22] have confirmed the existence of two regions as shown in Figure 11. In region 1, i.e., the region between points A and B, the void fraction is on the order of one to two percent. Therefore, the mixture density in this region is almost same as the liquid density, which is the value predicted by the equilibrium model. But, beyond point B, i.e., in region 2, the void fraction increases rapidly, and the liquid density can no longer be accepted as the mixture density. Therefore, for all intents and purposes the point B can be considered as the boundary between the liquid phase region and the two-phase mixture region. This point is called the "Point of Net Vapor Generation". Now, the task is to locate this point of net vapor generation in terms of system parameters and then predict the true void fraction profile.

IV-2. Previous Work on Point of Net Vapor Generation

Several attempts have been made in the past to predict the location of point B, i.e., the point of net vapor generation. Those shall be discussed briefly in the following subsections.

Bowring's Model [21]

Bowring was first to suggest that the initiation of significant vapor formation corresponds to the point of initial bubble detachment from the wall. He developed an empirical relation, based on the then existing steam-water void fraction data, which was expressed in the form:

Reproduced with permission of the copyright owner. Further reproduction prohibited without permission.

$$\Delta T_{\lambda} = T_{sat} - T_{\lambda} = \frac{\dot{q}''_{w}\,(14 + 0.1\,P)}{v_{fi}} \qquad (4\text{-}1)$$

where, the local subcooling at the point of net vapor generation, ΔT_{λ}, was in ^{o}C, the heat flux, $\dot{q}''_{w}$, was in watts/cm^2, system pressure, P, was in atmosphere, and liquid inlet velocity, v_{fi}, was in cm/sec.

Since this correlation is not dimensionless and is based on a few experimental data, it is of limited usefulness. However, the idea of bubble detachment formed the basis of two later models, namely those of Levy [23] and Staub [24]. In these models it is postulated that no bubble is detached from the surface in the region 1, shown in Figure 11, and the initial point of bubble detachment is the point of net vapor generation.

Levy's Model [23]

Levy assumed a bubble of arbitrary shape attached to the heated surface. The point of bubble detachment was established from two considerations. First, a balance of all the forces acting on the bubble, i.e., surface tension force, buoyant force, and drag force, was used to determine the distance, Y_B, of the top of the bubble from the wall. Then, Martinelli's universal temperature profile was assumed as the temperature distribution from the wall to the top of the bubble. The liquid temperature at the top of the bubble was taken to be equal to the saturation temperature and the expression for single phase turbulent heat transfer coefficient was used to calculate the difference between the wall temperature and the liquid bulk temperature. The local subcooling at the point of net vapor generation was finally given by

Reproduced with permission of the copyright owner. Further reproduction prohibited without permission.

$$\Delta T_{\lambda} = (T_W - T_{\lambda}) - (T_W - T_{sat}) \tag{4.2}$$

$$= \frac{\dot{q}''_W}{h_f} - \frac{\dot{q}''_W \, T_B^+}{c_{pf} \rho_f \sqrt{\tau_w/\rho_f}}$$

where,

$$\left.\begin{aligned} T_B^+ &= Pr_f \, Y_B^+ && \text{if } 0 \le Y_B^+ \le 5 \\ T_B^+ &= 5\left\{ Pr_f + \ln\left[1 + Pr_f\left(\frac{Y_B^+}{5} - 1\right)\right]\right\} && \text{if } 5 \le Y_B^+ \le 30 \\ T_B^+ &= 5\left\{ Pr_f + \ln\left[1 + 5\,Pr_f\right] + 0.5 \ln\left[\frac{Y_B^+}{30}\right]\right\} && \text{if } Y_B^+ \ge 30 \end{aligned}\right\} \tag{4.3}$$

$$Y_B^+ = 0.015 \left(\sigma D_h \rho_f\right)^{1/2} \frac{1}{\mu_f} \tag{4.4}$$

$$h_f = 0.023 \, Re_f^{0.8} \, Pr_f^{0.4} \, \frac{k_f}{D_h} \tag{4.5}$$

$$\tau_w = \frac{f_f}{8} \rho_f v_{fi}^2 \tag{4.6}$$

$$f_f = 0.0055 \left\{ 1 + \left[20000 \left(\frac{\epsilon}{D_h}\right) + 10^6 / Re_f \right]^{1/3} \right\} \tag{4.7}$$

and, the channel relative roughness parameter, ϵ/D_h, was taken to be that of drawn tubing, i.e., equal to 10^{-4}. The constant 0.015 in equation (4.4) was determined from the then existing steam-water data.

Reproduced with permission of the copyright owner. Further reproduction prohibited without permission.

This model, besides being very complicated to use, raises several basic questions. First, there is no justification for using the expression for the single-phase heat-transfer coefficient in a region where the value of heat-transfer coefficient is much higher due to bubble agitation. This is why this model predicts unrealistically high values for wall temperature, especially at low mass-flow rates [25]. Secondly, the use of Martinelli's temperature profile near the wall, i.e., in the bubble boundary layer, is highly questionable. The model has met with reasonable success for high mass-flux data mainly because the constant in Equation (4.4) was determined from such data.

Staub's Model [24]

Staub assumed an essentially hemispherical departure geometry for the bubble that still allowed for a variable contact angle at the heated surface. A force balance, similar to that of Levy, was used to determine the mean diameter of the departing bubbles. The liquid temperature at the top of the bubble was taken to be equal to the saturation temperature, and Martinelli's universal temperature profile was used as the temperature distribution from the top of the departing bubble to the center line of the channel. The local subcooling at the point of bubble detachment was given by:

$$\Delta T_\lambda = \frac{\dot{q}''_w}{c_{pf}\,\rho_f\,v_{fi}\sqrt{f_f/8}}\left\{ Pr_f\left(5-Y_d^+\right) - 5\ln\left(1+5\,Pr_f\right) + 2.5\left[\frac{\ln\left(Y_{cL}^+/30\right)}{1-30/Y_{cL}^+}-1\right]\right\} \quad \text{if } 0\le Y_d^+ \le 5 \tag{4.8}$$

$$\Delta T_\lambda = \frac{\dot{q}''_w}{c_{pf}\,\rho_f\,v_{fi}\sqrt{f_f/8}}\left\{5\ln\frac{\left(1+5\,Pr_f\right)}{\left[1+Pr_f\left(Y_d^+/5-1\right)\right]}\right. \quad \text{(continued)}$$

Reproduced with permission of the copyright owner. Further reproduction prohibited without permission.

$$+ 2.5\left[\frac{\ln(Y_{cL}^{+}/30)}{1-30/Y_{cL}^{+}} - 1\right]\Bigg\} \quad \text{if } 5 \le Y_d^{+} \le 30$$

$$\Delta T_\lambda = \frac{2.5\,\dot{q}''_w}{c_{pf}\,\rho_f\,v_{fi}\sqrt{f_f/8}} \left\{\frac{\ln(Y_{cL}^{+}/Y_d^{+})}{1-Y_d^{+}/Y_{cL}^{+}} - 1\right\}\left\{1 - \frac{Y_d^{+}}{Y_{cL}^{+}}\right\} \quad \text{if } Y_d^{+} > 30$$

where,

$$Y_d^{+} = \frac{(D_d/2)\,\rho_f\,v_{fi}\sqrt{f_f/8}}{\mu_f} \tag{4.9}$$

The bubble diameter, D_d, is determined from:

$$\frac{f_f\,\rho_f\,v_{fi}^2\,D_d}{32\,g\,\sigma\,f(\beta)} + \frac{D_d^2\,(\rho_f - \rho_g)}{12\,\sigma\,f(\beta)} = 1 \tag{4.10}$$

The friction factor, f_f, is determined by taking $(D_d/2D_h)$ as the relative roughness parameter, which calls for an iterative procedure. Besides, the value of bubble contact angle function, $f(\beta)$, is not available yet. Staub suggested a value of 0.02-0.03 for $f(\beta)$, based on steam-water data; but, nothing can be said for other fluids. This model is more complicated than that of Levy and its use in dynamic studies is impractical.

Ahmad's Model [25,26]

Ahmad postulated that, because of the growth and collapse cycle of nucleating bubbles, the liquid-phase heat-transfer coefficient increases significantly in region 1 (see Figure 11). He assumed that this heat-transfer coefficient attains a maximum value of h_1 at the point of bubble detachment and then remains constant. As the amount of net vapor formation at the point of bubble detachment is negligible, all the heat added is still being utilized in raising the liquid bulk temperature. Therefore, the subcooling at the point of net vapor generation was given by:

Reproduced with permission of the copyright owner. Further reproduction prohibited without permission.

$$\Delta T_{\lambda} = \frac{\dot{q}''_w}{h_1} \tag{4.11}$$

where, h_1 was determined from the best fit of Costa's [27] and Maurer's [28] experimental data, and was expressed in the form:

$$h_1 = 2.44\,(Re_f)^{1/2}(Pr_f)^{1/3}\left(\frac{i_1}{i_{fs}}\right)^{1/3}\left(\frac{\Delta i_{fg}}{i_{fs}}\right)^{1/3} \tag{4.12}$$

The results predicted by this model, although good for high mass-flow rates, are not satisfactory for low mass-flux data of Dix [22] and Rouhani [29].

Dix's Model [22]

Dix correlated his own low flow rate data (only two different flow rates) by the expression:

$$\Delta T_{\lambda} = 0.00135\,\frac{\dot{q}''_w}{h_f}\,(Re_f)^{1/2} \tag{4.13}$$

where, h_f is the single-phase heat-transfer coefficient.

This correlation and a few others, namely those of Costa [27] and Rouhani [30,31] are restricted to the data from which they were derived. Therefore, these are of limited usefulness and will not be discussed further.

IV-3. Present Model for the Point of Net Vapor Generation

From the previous section it is clear that at present there is no general model or correlation which can predict accurately the point of net vapor generation for all mass flow rates. Moreover, the experimental

Reproduced with permission of the copyright owner. Further reproduction prohibited without permission.

observations of Dix [22] indicate that the bubble detachment criterion alone is not sufficient to represent the point of net vapor generation. This is because he observed a flowing bubble layer near the wall in the highly subcooled region, i.e., region 1 in Figure 11. The purpose of the present section is, therefore, to re-examine this problem and come up with a simple, easy-to-use general correlation.

It is apparent that the point of net vapor generation must satisfy both the thermal as well as the hydrodynamic restraints. If the situation is such that the bubbles are detached from the surface, but the local subcooling is so high that the bubbles are immediately condensed as they moved to the liquid core, then the void fraction profile cannot grow. In that case, to initiate a rapid increase in void fraction the bubbles have to flow further along the wall until the liquid subcooling is reduced significantly so that the effect of vapor condensation is compensated by the rate of evaporation close to the wall. This is in agreement with the observation of Dix [22]. On the other hand, if the bubbles do not detach from the surface even when the local subcooling is low, the void fraction cannot increase significantly. However, as soon as the hydrodynamic conditions will permit it, bubbles will start detaching from the wall. New bubbles will be formed at the wall and the process will manifest itself by the rapid increase in void fraction. This is the situation assumed in the bubble detachment models.

From experimental data [32,33], it has been observed that for high and moderate inlet subcooling, the initial point of net vapor generation is almost independent of the inlet subcooling. Dix [22] also observed that the bubble layer thickness at the point of initial bubble ejection

Reproduced with permission of the copyright owner. Further reproduction prohibited without permission.

was independent of liquid inlet temperature. Therefore, it can be argued that the point of net vapor generation is dependent only on the local thermal and hydrodynamic conditions which determine the rates of vapor condensation and evaporation at the wall. In order to make an estimate of these two rates we can assume that the rate of evaporation at the wall will be proportional to heat flux whereas the rate of condensation will be proportional to the local subcooling. Furthermore, at low mass-flow rates the condensation will be governed by a diffusion process. Consequently, for the thermally controlled region, i.e., at low mass-flow rates we can expect that the local Nusselt number,

$$Nu = \frac{\dot{q}''_w D_h}{k_f (T_{sat} - T_\lambda)} \tag{4.14}$$

will be the similarity parameter.

On the other hand, at high mass-flux rates, where the bubble detachment models have met with reasonable success, the phenomenon may be hydrodynamically controlled. If we regard that attached bubbles may affect the flow as surface roughness, then detaching bubbles should correspond to a particular scale of roughness. Furthermore, if we assume that Reynolds' analogy holds, then at high mass flow rates we could expect that the local Stanton number,

$$St = \frac{\dot{q}''_w}{G c_{pf} (T_{sat} - T_\lambda)} \tag{4-15}$$

will be the appropriate scaling group.

It can be noticed that according to the above expression, at

Reproduced with permission of the copyright owner. Further reproduction prohibited without permission.

high mass-flow rates the rate of condensation is governed by convection. This is in contrast with the case of low mass-flow rates where the condensation is likely to be governed by diffusion as described by Equation (4.14).

In order to determine whether or not (4.14) and (4.15) are the appropriate scaling groups, it is desirable to eliminate the dependent variable, i.e., the local subcooling, from one of these relations. This can be achieved by introducing the Peclet number which is, by definition, the ratio of the Nusselt number and the Stanton number. It is also the ratio of the flow velocity to the diffusion velocity of heat normal to the heated surface. This allows proper scaling of flow rate for various fluids with different thermal diffusivities.

Therefore, it was decided to plot various existing data for the point of net vapor generation on a St-Pe co-ordinate system. Data used for this purpose are shown in Table 8. It should be noted that three different fluids (water, Freon-22, and Freon-114) with wide range of system pressure, mass flow rate, heat flux, and various channel geometries have been considered. The result of the plot is shown in Figure 12.

Two distinct regions can be identified in Figure 12. Up to Peclet number equal to 70,000 data fall on a straight line having the slope of minus one which implies a constant value for the local Nusselt number. Beyond the Peclet number of 70,000 data fall on a constant Stanton number. The entire correlation for the point of net vapor generation can be expressed as:

$$Nu = \frac{\dot{q}''_w D_h}{k_f \Delta T_\lambda} = 455 \qquad \text{if } Pe \leq 70{,}000 \qquad (4.16)$$

Reproduced with permission of the copyright owner. Further reproduction prohibited without permission.

Reproduced with permission of the copyright owner. Further reproduction prohibited without permission.

Table 8. Data Used for the Present Correlation

Author [Ref]	Fluid	Channel Geometry	Pressure psia	Mass Velocity $G \times 10^{-6}$ lbm/hr-ft^2	Heat Flux $\dot{q}''_w \times 10^{-6}$ Btu/hr-ft^2	Symbol in Figure 12
Dix [22]	Freon-114	0.374"I.D. 0.734"O.D. Annular	45.8 and 123	0.075-0.153	0.002-0.017	●
Maurer [28]	Water	1" × 0.0876" Rectangular	1200 and 1600	0.299-0.904	0.097-0.606	×
Rouhani [29]	Water	0.473"I.D. 0.984"O.D. Annular	142-566	0.077-1.061	0.092-0.282	○
Egen, et al. [33]	Water	1" × 0.103" Rectangular	2000	0.640-0.850	0.150-0.400	■
Martin [34]	Water	1.97" × 0.11" Rectangular	1153 and 2005	0.553-1.624	0.127-0.539	△
Staub, et al. [35]	Water	2.50" × 0.25" Rectangular	17 and 44.7	0.253-2.078	0.098-0.251	◇
Staub, et al. [35]	Water	0.4"I.D. Circular	600 and 1000	0.572-2.039	0.251-0.376	□
Staub, et al. [35]	Freon-22	0.4"I.D. Circular	188-493	0.133-1.026	0.006-0.020	▼
Bartolemei, et al. [36]	Water	0.606"I.D. and 0.945"I.D. Circular	218-653	0.644	0.121-0.254	⊗
Evangelisti, et al. [37]	Water	0.276"I.D., 0.512"O.D. Annular	14.7	0.450-1.045	0.139-0.281	▽

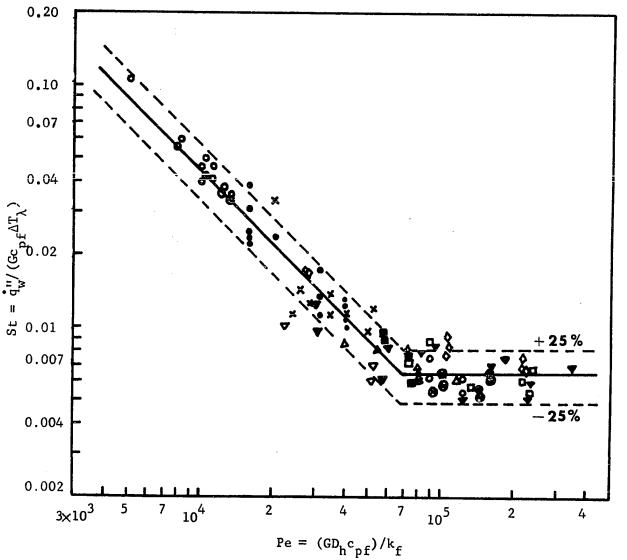

Figure 12. Peclet Number versus Stanton Number at the Point of Net Vapor Generation

Reproduced with permission of the copyright owner. Further reproduction prohibited without permission.

and,

$$St = \frac{\dot{q}''_w}{G c_{pf} \Delta T_\lambda} = 0.0065 \qquad \text{if} \quad Pe \geq 70{,}000 \qquad (4.17)$$

In the stability analysis, which is presented in the next chapter, the above criteria shall be used to determine the boiling boundary between the single-phase liquid region and the two-phase mixture region. For convenience of the analysis, Equations (4.16) and (4.17) are re-written as:

$$\Delta i_\lambda = i_{fs} - i_\lambda = 0.0022 \frac{\dot{q}''_w D_h c_{pf}}{k_f} \qquad \text{if} \quad Pe \leq 70{,}000 \qquad (4.18)$$

and,

$$\Delta i_\lambda = i_{fs} - i_\lambda = 154 \frac{\dot{q}''_w}{\rho_f v_{fi}} \qquad \text{if} \quad Pe \geq 70{,}000 \qquad (4.19)$$

Recognizing that the equilibrium vapor quality at the point of net vapor generation, x_λ, is given by

$$x_\lambda = - \frac{c_{pf} \Delta T_\lambda}{\Delta i_{fg}} \qquad (4.20)$$

one can also express the above correlation as:

$$x_\lambda = -0.0022 \frac{\dot{q}''_w}{\rho_f \Delta i_{fg}} \frac{D_h}{a_f} \qquad \text{if} \quad Pe \leq 70{,}000 \qquad (4.21)$$

and,

Reproduced with permission of the copyright owner. Further reproduction prohibited without permission.

$$z_\lambda = -154 \frac{\dot{q}''_w}{\rho_f \Delta i_{fg}} \frac{1}{v_{fi}} \qquad \text{if } Pe \geq 70{,}000 \qquad (4.22)$$

Interpretation of the Correlation

It can be recognized that for Peclet number less than 70,000 the local subcooling, ΔT_λ, at the point of net vapor generation is independent of flow velocity. Therefore, this is the thermally controlled region. On the other hand, for Peclet number greater than 70,000 the local Stanton number is found to be a constant. From the analogy between heat and momentum transfer, this implies that the friction factor at the point of net vapor generation is a constant. This behavior is very similar to that of turbulent flow in sand-roughened pipes [38]. Therefore, it appears that the bubbles, attached to the wall act like roughness heights. The attached bubbles will grow until a characteristic value of roughness parameter, k_s/D, is reached at which point they detach from the surface. For Prandtl number equal to one, this characteristic value of roughness parameter, k_s/D, is about 0.02 which corresponds to a Stanton number of 0.0065.

From the above criterion, the bubble will be detached from the surface as soon as the local Stanton number becomes 0.0065. At low mass-flow rates, i.e., $Pe < 70{,}000$, local Nusselt number still remains below 455. This means that the local subcooling is still high and the detached bubbles are forced to stay near the heated wall. The bubbles flow downstream while remaining close to the wall, until the local Nusselt number becomes 455. At this point the local subcooling is low enough to initiate a rapid increase in void fraction. This was precisely what Dix observed

Reproduced with permission of the copyright owner. Further reproduction prohibited without permission.

in his experiments [22]. We denote this region (Pe < 70,000) as the thermally controlled region. On the other hand, for high mass-flow rates, i.e., Pe > 70,000, Stanton number reaches the value of 0.0065 at a point where Nusselt number is already higher than 455. Therefore, as soon as the bubbles are detached from the wall they can move to the liquid core without being rapidly condensed. This results in a rapid increase in vapor void fraction at the point of bubble detachment. This also explains why the previous bubble detachment models were reasonably successful at high mass-flow rates. We denote this region (Pe > 70,000) as the hydrodynamically controlled region.

IV-4. Prediction of True Vapor Void Fraction

The time-smoothed and area-averaged conservation equation for mass of the vapor phase in a two-phase mixture in thermodynamic non-equilibrium is given by [2,16,19]:

$$\frac{\partial}{\partial t}\langle \alpha \rho_g \rangle + \frac{\partial}{\partial z}\langle \alpha \rho_g v_g \rangle = \langle \Gamma_g \rangle \tag{4.23}$$

where, $\langle \Gamma_g \rangle$ is the mass rate of vapor generation per unit volume of the mixture. This is the source term similar to the rate of reaction term in a chemically reacting binary gas mixture.

For steady state and constant vapor phase density, the above equation takes the form:

$$\langle \alpha v_g \rangle = \int_{\lambda}^{z} \frac{\langle \Gamma_g \rangle}{\rho_g} dz \tag{4.24}$$

where, λ is the initial point of net vapor generation.

Reproduced with permission of the copyright owner. Further reproduction prohibited without permission.

Introducing the definition of vapor drift velocity, i.e.,

$$V_{gj} = v_g - j \tag{4.25}$$

we obtain,

$$\langle \alpha j \rangle + \langle \alpha V_{gj} \rangle = \int_{\lambda}^{z} \frac{\langle \Gamma_g \rangle}{\rho_g} dz \tag{4.26}$$

By introducing the definition of distribution parameter, C_o [39,40], i.e.,

$$C_o = \frac{\langle \alpha j \rangle}{\langle \alpha \rangle \langle j \rangle} \tag{4.27}$$

and, weighted mean vapor drift velocity, $\overline{V}_{gj}$, i.e.,

$$\overline{V_{gj}} = \frac{\langle \alpha V_{gj} \rangle}{\langle \alpha \rangle} \tag{4.28}$$

we obtain the expression for true area averaged vapor void fraction:

$$\langle \alpha \rangle = \frac{\int_{\lambda}^{z} \frac{\langle \Gamma_g \rangle}{\rho_g} dz}{C_o \langle j \rangle + \overline{V}_{gj}} \tag{4.29}$$

The volumetric flux density, $\langle j \rangle$, can be expressed in terms of the total mass flux, G, and the vapor mass flux, G_g, as follows:

Reproduced with permission of the copyright owner. Further reproduction prohibited without permission.

$$\langle j \rangle = \langle j_g \rangle + \langle j_f \rangle = \frac{G_g}{\rho_g} + \frac{(G - G_g)}{\rho_f} \tag{4.30}$$

where,

$$G = \rho_f v_{fi} = G_g + G_f \tag{4.31}$$

and,

$$G_g = \langle \alpha \rho_g v_g \rangle = \int_\lambda^z \langle \Gamma_g \rangle \, dz \tag{4.32}$$

Therefore, Equation (4.29) can be written as:

$$\langle \alpha \rangle = \frac{\int_\lambda^z \langle \Gamma_g \rangle \, dz}{C_o \left[\frac{\Delta \rho}{\rho_f} \int_\lambda^z \langle \Gamma_g \rangle \, dz + \frac{\rho_g}{\rho_f} G \right] + \rho_g \bar{V}_{gj}} \tag{4.33}$$

The true vapor quality, x, is defined as:

$$x = \frac{G_g}{G} = \frac{1}{G} \int_\lambda^z \langle \Gamma_g \rangle \, dz \tag{4.34}$$

Therefore, the true vapor void fraction, $\langle \alpha \rangle$, can also be expressed in terms of the true vapor quality, x, as:

Reproduced with permission of the copyright owner. Further reproduction prohibited without permission.

$$\langle \alpha \rangle = \frac{x}{C_0\left[x\frac{\Delta\rho}{\rho_f} + \frac{\rho_g}{\rho_f}\right] + \frac{\rho_g \bar{V}_{gj}}{G}} \tag{4.35}$$

It is evident from Equations (4.33) and (4.34) that the ability to predict the vapor void fraction, $\langle \alpha \rangle$, and the true vapor quality, x, depends on the ability to determine: a) the rate of vapor generation per unit volume, $\langle \Gamma_g \rangle$, and b) the point of net vapor generation, λ. In the previous section a model has been developed for determining λ; in the section that follows we shall consider the problem of predicting $\langle \Gamma_g \rangle$.

IV-5. Constitutive Relation for the Rate of Vapor Generation

The constitutive equations for chemical reactions are given in terms of reaction rates. For a two-phase mixture the problem is more complicated, because the constitutive equation will depend not only on the mode of heat transfer, but also on the topology of the interface, i.e., the flow regime.

The formal approach to determine the rate of vapor generation per unit volume, $\langle \Gamma_g \rangle$, in the bubbly flow regime has been described in [40,41,42]. At a position z downstream of λ, i.e., the point of net vapor generation, there will be bubbles of varying sizes depending on the distance from the point at which they nucleated. Let J(z') be the rate of bubble nucleation per unit area at z', a location in between λ and z. Let m(z, z') be the bubble growth law, i.e., the mass of a bubble at z that nucleated at z'. Therefore, for a duct of constant cross section, the mass flow rate of vapor passing through the point z can be given by [40]:

$$G_g(z) = \frac{\xi_h}{A_c} \int_{\lambda}^{z} m(z, z')\, J(z')\, dz' \tag{4.36}$$

Reproduced with permission of the copyright owner. Further reproduction prohibited without permission.

By differentiating the above expression one can obtain the mass rate of vapor formation per unit volume, Γ_g (henceforth, the notation $< >$ is deleted for the sake of simplicity):

$$\Gamma_g(z) = \frac{dG_g}{dz} = \frac{\mathcal{F}_h}{A_c}\int_{\lambda}^{z} \frac{dm(z,z')}{dz} J(z')\, dz' \tag{4.37}$$

Since both the bubble nucleation rate, J(z'), and the bubble growth law, m(z, z'), depend on liquid temperature, which varies with distance, it is necessary to solve the energy equation simultaneously with Equation (4.37) in order to be able to evaluate Γ_g. Neglecting the effects of kinetic and potential energy, and assuming the steady state condition with constant vapor phase enthalpy (equal to the corresponding saturation value), the mixture energy equation can be written as [40,42]:

$$(G-G_g)\frac{di_f}{dz} + \Gamma_g(i_g - i_f) = \frac{\dot{q}''_w \mathcal{F}_h}{A_c} \tag{4.38}$$

It is now clear that because Γ_g and i_f are interdependent, one needs to know one of the two to determine the other.

To evaluate Γ_g from Equation (4.37) one must know: (a) the location λ, (b) the rate of heterogeneous nucleation, J(z'), and (c) the bubble growth law, m(z, z'). A new general correlation for the location λ has been presented in section IV-3 of the present thesis, but, as of today, there is no accurate model to determine theoretically any of the other two terms, i.e., J(z') and m(z, z'). Although several assumptions could be made in order to evaluate the integral in Equation (4.37), experimental

Reproduced with permission of the copyright owner. Further reproduction prohibited without permission.

data are not available which could be used to support these assumptions [40].

Another approach would be to make a realistic assumption about the liquid bulk enthalpy, i_f, and then determine Γ_g from Equation (4.38). For a constant property liquid, the following boundary conditions can be deduced from Figure 11:

at $z = \lambda$,

$$i_f = i_\lambda \tag{4.39}$$

and,

$$\frac{di_f}{dz} = \frac{i_{fs} - i_\lambda}{\lambda_{eq} - \lambda} = \frac{\Delta i_\lambda}{\Delta \ell}$$

at $z \to \infty$,

$$i_f \to i_{fs} \tag{4.40}$$

and,

$$\frac{di_f}{dz} \to 0$$

One of the liquid enthalpy distributions that satisfies the above set of boundary conditions is:

$$\frac{i_f(z) - i_\lambda}{i_{fs} - i_\lambda} = 1 - \exp\left\{-\frac{z - \lambda}{\Delta \ell}\right\} \tag{4.41}$$

where, the characteristic length, $\Delta \ell$, is given by:

Reproduced with permission of the copyright owner. Further reproduction prohibited without permission.

$$\Delta l = \lambda_{eq} - \lambda = \frac{G A_c (i_{fs} - i_\lambda)}{\dot{q}''_w \xi_h} \tag{4.42}$$

This distribution was first suggested by Zuber, et al. [40,42] and was also obtained by Ahmad [26], neglecting the effect of bubble condensation.

The Equation (4.38) can be re-written as:

$$\Gamma_g(z) = \frac{\frac{\dot{q}''_w \xi_h}{A_c} - G(1-x)\frac{di_f(z)}{dz}}{\Delta i_{fg} + (i_{fs} - i_f(z))} \tag{4.43}$$

The following approximations can simplify the above expression to a great extent:

1. $$(1-x)\frac{di_f(z)}{dz} \approx \frac{di_f(z)}{dz} \tag{4.44}$$

At the beginning of void formation, where $\frac{di_f(z)}{dz}$ is large, the value of x is much less than one; subsequently, as x increases, $\frac{di_f(z)}{dz} \to 0$. Therefore, the error caused by the above simplification will not be significant.

2. $$\Delta i_{fg} + (i_{fs} - i_f(z)) \approx \Delta i_{fg} \tag{4.45}$$

Since, Δi_λ is usually much smaller than Δi_{fg} the above approximation is also in order. These simplifications, however, have already been introduced by Ahmad [26].

From Equations (4.41) and (4.42),

$$\frac{di_f(z)}{dz} = \frac{\dot{q}''_w \xi_h}{G A_c} \exp\left\{-\frac{z-\lambda}{\Delta l}\right\} \tag{4.46}$$

Reproduced with permission of the copyright owner. Further reproduction prohibited without permission.

Utilizing (4.44), (4.45), and (4.46), one can write the final expression for Γ_g as:

$$\Gamma_g(z) = \frac{\dot{q}''_w \xi_h}{A_c \Delta i_{fg}} \left[1 - \exp\left\{-\frac{z-\lambda}{\Delta \ell}\right\}\right] \tag{4.47}$$

The above relation for the rate of vapor generation can be used in Equation (4.33) to calculate the true vapor void fraction. However, it is more convenient if a relation between the true vapor quality, x, and the equilibrium vapor quality, x_{eq}, can be found, because most of the experimental data on void fraction is plotted against x_{eq}. In that case, Equation (4.35) can be used to predict the vapor void fraction.

Using the definition of true vapor quality, i.e., Equation (4.34), and the expression (4.47), one obtains:

$$x = \frac{\dot{q}''_w \xi_h \Delta \ell}{G A_c \Delta i_{fg}} \left[\left(\frac{z-\lambda}{\Delta \ell}\right) - \left\{1 - \exp\left(-\frac{z-\lambda}{\Delta \ell}\right)\right\}\right] \tag{4.48}$$

The equilibrium quality, i.e., the vapor quality based on thermodynamic equilibrium model, is given by:

$$x_{eq} = \frac{\dot{q}''_w \xi_h \Delta \ell}{G A_c \Delta i_{fg}} \left[\frac{z-\lambda}{\Delta \ell} - 1\right] \tag{4.49}$$

Furthermore, the equilibrium quality at the point of net vapor generation is given by:

Reproduced with permission of the copyright owner. Further reproduction prohibited without permission.

$$x_\lambda = -\frac{\Delta i_\lambda}{\Delta i_{fg}} = -\frac{\dot{q}''_w \xi_h \Delta l}{G A_c \Delta i_{fg}} \tag{4.50}$$

Using Equation (4.49) and (4.50), one can write the expression for true vapor quality as:

$$x = x_{eq} - x_\lambda \exp\left\{\frac{x_{eq}}{x_\lambda} - 1\right\} \tag{4.51}$$

where, x_λ can be determined from Equation (4.21) or (4.22).

The expression (4.51) was assumed by Levy [23] in his prediction of vapor void fraction. In the present case, however, this has been derived from a logical choice of liquid bulk enthalpy.

IV-6. Comparison of Predicted Vapor Void Fraction with Experimental Data

The vapor void fraction, $<\alpha>$, can now be predicted theoretically from Equations (4.35), (4.51), and (4.21) or (4.22). The value for the distribution parameter, C_o, is taken to be equal to 1.13 [23,42]. The weighted mean vapor drift velocity, $\bar{V}_{gj}$, for upward bubbly churn flow is calculated from [42]:

$$\bar{V}_{gj} = 1.41\left[\frac{\sigma g \Delta\rho}{\rho_f^2}\right]^{1/4} \tag{4.52}$$

The predicted results are compared with various experimental data in Figures 13 through 15. It can be seen that the agreement between the theoretical prediction and the experimental data is quite satisfactory.

Reproduced with permission of the copyright owner. Further reproduction prohibited without permission.

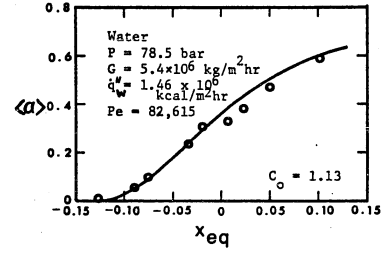

Figure 13. Comparison between Predicted and Measured Vapor Void Fraction; Data of Martin [34]

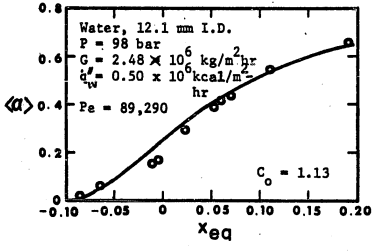

Figure 14. Comparison between Predicted and Measured Vapor Void Fraction; Data of Lobachev, et al. [43]

Reproduced with permission of the copyright owner. Further reproduction prohibited without permission.

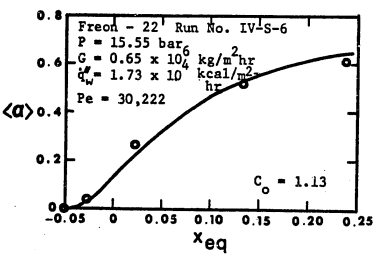

Figure 15. Comparison between Predicted and Measured Vapor Void Fraction; Data of Staub, et al. [35]

Reproduced with permission of the copyright owner. Further reproduction prohibited without permission.

CHAPTER V

STABILITY ANALYSIS

V-1. Formulation of the Problem

The mathematical representation of a heated boiling channel with a large by-pass is shown in Figure 16. The components at the upstream of the inlet of the heated channel are lumped together and considered as an inlet restriction with orifice coefficient k_i. Similarly, the components at the downstream of the exit of the heated channel are considered as an exit restriction with orifice coefficient k_e. The length of the boiling channel is ℓ. Liquid enters the channel with a velocity v_{fi} and at a temperature lower than the corresponding saturation temperature. Due to heat addition, liquid bulk temperature increases, and significant vapor generation starts at a distance λ from the inlet. The location of this point, which is the boiling boundary between the single-phase liquid region and the two-phase mixture region, can be determined from the correlation presented in section IV-3. The distance of this point from the inlet, however, can be a function of time because of the inlet flow fluctuation. The large unheated by-pass imposes a constant pressure drop boundary condition across the boiling channel at the onset of flow instabilities. This is the same as having a flat pump characteristic, i.e.,

$$\frac{\partial \Delta P_{ex}}{\partial v_{fi}} = 0 \tag{5.1}$$

Reproduced with permission of the copyright owner. Further reproduction prohibited without permission.

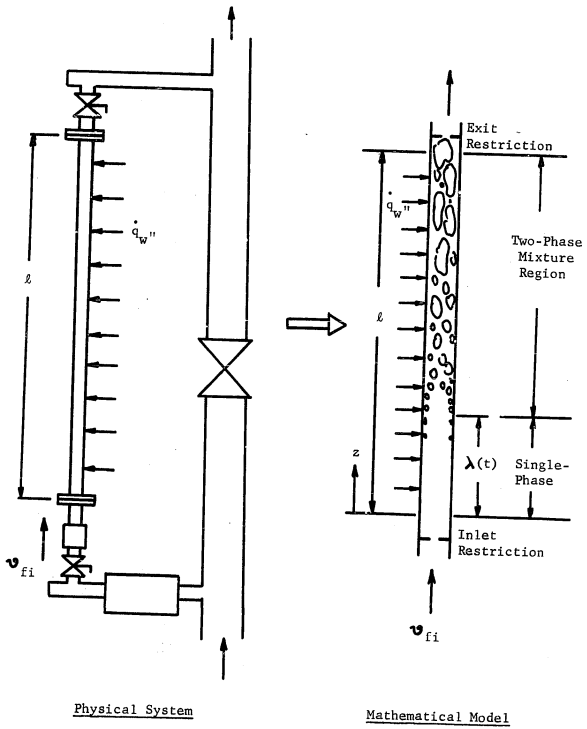

Figure 16. Mathematical Representation of the Physical System

Reproduced with permission of the copyright owner. Further reproduction prohibited without permission.

Single-Phase Liquid Region

The liquid is considered to be incompressible with constant thermodynamic and transport properties. Therefore, the conservation equations are:

1. Continuity:

$$\frac{\partial v_f}{\partial z} = 0 \tag{5.2}$$

2. Momentum:

$$-\frac{\partial P}{\partial z} = \rho_f \left\{ \frac{\partial v_f}{\partial t} + v_f \frac{\partial v_f}{\partial z} \right\} + \frac{f_f}{2D_h} \rho_f v_f^2 + g \rho_f \tag{5.3}$$

3. Energy:

$$\frac{\partial i_f}{\partial t} + v_f \frac{\partial i_f}{\partial z} = \frac{\dot{q}''_w \xi_h}{\rho_f A_c} \tag{5.4}$$

As the liquid density, ρ_f , is a constant, the variables v_f, i_f, and P can be determined from the above conservation equations, if the heat flux, $\dot{q}''_w$, and the single-phase liquid friction factor, f_f, are specified.

Two-Phase Mixture Region

In general, a two-phase mixture can be formulated by using any of the two following models:

1. Two Fluid Model
2. Mixture or Diffusion or Drift Model

In the two fluid model [44], each phase is treated as a continuum with an interface in between. Three conservation equations, namely

Reproduced with permission of the copyright owner. Further reproduction prohibited without permission.

continuity, momentum, and energy, are written for each phase. In addition, three "jump" conditions at the interface as well as several constitutive equations are needed to complete the formulation. The model is suitable for studies of interfacial phenomena, but is not recommended for studies of system dynamics.

In the mixture model, the entire mixture is transformed to a continuum. Two continuity equations are still required; but, only one mixture momentum equation and one mixture energy equation along with appropriate constitutive relations are sufficient to formulate the problem. The model is capable of taking into account the effects of relative velocity and thermal non-equilibrium between the phases. This is similar to the binary reacting gas mixture model, and is suitable for studies of system dynamics. This model is, therefore, chosen here to formulate the flow in the two-phase mixture region.

The time-smoothed and area-averaged conservation equations as derived by Zuber [16] and Ishii [2,19] shall be used. These are:

1. Conservation of mass of the mixture:

$$\frac{\partial \rho_m}{\partial t} + \frac{\partial}{\partial z}\left[\rho_m v_m\right] = 0 \tag{5.5}$$

2. Conservation of mass of the vapor phase:

$$\frac{\partial}{\partial t}\left[\alpha \rho_g\right] + \frac{\partial}{\partial z}\left[\alpha \rho_g v_g\right] = \Gamma_g \tag{5.6}$$

3. Conservation of momentum of the mixture (neglecting the effect of surface tension):

Reproduced with permission of the copyright owner. Further reproduction prohibited without permission.

$$\rho_m \left[\frac{\partial v_m}{\partial t} + v_m \frac{\partial v_m}{\partial z} \right] = - \frac{\partial P_m}{\partial z} - \frac{f_m}{2D_h} \rho_m v_m^2 \qquad (5.7)$$

$$- g \rho_m - \frac{\partial}{\partial z} \left[\frac{\rho_f - \rho_m}{\rho_m - \rho_g} \frac{\rho_f \rho_g}{\rho_m} V_{gj}^2 \right]$$

4. Conservation of energy of the mixture (neglecting the effect of kinetic and potential energy):

$$\rho_m \left[\frac{\partial i_m}{\partial t} + v_m \frac{\partial i_m}{\partial z} \right] = \frac{\dot{q}''_w \xi_h}{A_c} + \frac{\partial P_m}{\partial t} \qquad (5.8)$$

$$- \frac{\partial}{\partial z} \left[\frac{\rho_f - \rho_m}{\rho_m} \frac{\rho_f \rho_g}{\Delta \rho} V_{gj} (i_g - i_f) \right]$$

The mixture density, ρ_m, the mixture pressure, P_m, the mixture velocity, v_m, and the mixture enthalpy, i_m, are defined as:

$$\rho_m = \alpha \rho_g + (1-\alpha) \rho_f \qquad (5.9)$$

$$P_m = \alpha P_g + (1-\alpha) P_f \qquad (5.10)$$

$$v_m = \frac{\alpha \rho_g}{\rho_m} v_g + \frac{(1-\alpha) \rho_f}{\rho_m} v_f \qquad (5.11)$$

$$i_m = \frac{\alpha \rho_g}{\rho_m} i_g + \frac{(1-\alpha) \rho_f}{\rho_m} i_f \qquad (5.12)$$

It should be noticed that the mixture density and the mixture pressure are obtained by weighing the corresponding phase properties with corresponding volumetric concentrations. The mixture velocity and the

Reproduced with permission of the copyright owner. Further reproduction prohibited without permission.

mixture enthalpy, however, are obtained by weighing the phase velocities and the phase enthalpies with corresponding mass concentrations. Therefore, v_m and i_m represent the velocity and the enthalpy of the center of mass of the mixture, respectively. This implies that the mixture momentum equation (5.7) and the mixture energy equation (5.8) are indeed written in terms of the center of mass of the mixture and, therefore, suitable for dynamic studies.

The relative velocity between the phases has been taken into consideration by introducing the vapor drift velocity, V_{gj}, which can be expressed as:

$$V_{gj} = v_g - j = (1-\alpha)(v_g - v_f) \tag{5.13}$$

where j, the volumetric flux density or the velocity of the center of volume of the mixture is given by:

$$j = \alpha v_g + (1-\alpha) v_f \tag{5.14}$$

Before trying to solve the problem in general form, several simplifying assumptions will be introduced. These are:

1. At any particular time and location, there is no pressure difference between the phases, i.e.,

$$P_g - P_f = 0$$

or

$$P_g = P_f = P \tag{5.15}$$

Reproduced with permission of the copyright owner. Further reproduction prohibited without permission.

Therefore,

$$P_m = \alpha P + (1-\alpha) P = P \tag{5.16}$$

2. The pressure drop across the channel is small compared to the system pressure, i.e., the inlet pressure. Therefore, the saturation temperature can be considered to be a constant throughout the length of the channel.
3. The enthalpy of the vapor phase is a constant and is equal to the corresponding saturation value.
4. Because of constant vapor phase enthalpy and small system pressure drop, the vapor phase density is assumed to be a constant. The liquid phase density has already been taken as a constant. This implies that the mixture density, ρ_m, is a function of vapor void fraction only, i.e.,

$$\rho_m = \rho_m(\alpha) \tag{5.17}$$

It can be seen from equations (5.5) through (5.8) that the two continuity equations are written in Eulerian form, whereas the momentum and energy equations are in Lagrangian form. For convenience of solution, it is preferable to transform the continuity equations to the Lagrangian form. The mixture continuity equation (5.5) can be written as:

$$\frac{\partial \rho_m}{\partial t} + v_m \frac{\partial \rho_m}{\partial z} = -\rho_m \frac{\partial v_m}{\partial z} \tag{5.18}$$

Reproduced with permission of the copyright owner. Further reproduction prohibited without permission.

The term $\frac{\partial v_m}{\partial z}$ can be evaluated from the vapor phase continuity equation (5.6) as shown below.

Due to the assumption of constant phase densities, equation (5.6) can be written as:

$$\frac{\partial \alpha}{\partial t} + \frac{\partial}{\partial z}\left[\alpha v_g\right] = \frac{\Gamma_g}{\rho_g} \tag{5.19}$$

Introducing the vapor drift velocity, V_{gj}, from equation (5.13), and the definition of void fraction, α, from equation (5.9), i.e.,

$$\alpha = \frac{\rho_f - \rho_m}{\Delta\rho} \tag{5.20}$$

one can express equation (5.19) as:

$$\frac{\partial \rho_m}{\partial t} + \frac{\partial}{\partial z}\left[\rho_m\left(j + V_{gj}\right)\right] - \rho_f \frac{\partial}{\partial z}\left(j + V_{gj}\right) = -\frac{\Gamma_g \Delta\rho}{\rho_g} \tag{5.21}$$

Using the identify [2],

$$j = v_m + \left(\frac{\rho_f}{\rho_m} - 1\right) V_{gj} \tag{5.22}$$

and the mixture continuity, i.e., equation (5.5), one can transform equation (5.21) to:

$$\frac{\partial v_m}{\partial z} = \frac{\Gamma_g \Delta\rho}{\rho_g \rho_f} + \frac{\partial V_{gj}}{\partial z} - \frac{\partial}{\partial z}\left[\frac{\rho_f}{\rho_m} V_{gj}\right] \tag{5.23}$$

Reproduced with permission of the copyright owner. Further reproduction prohibited without permission.

Substituting the above expression for $\frac{\partial v_m}{\partial z}$ in mixture continuity, i.e., equation (5.18), and using the identity (5.22), one obtains:

$$\frac{\partial \rho_m}{\partial t} + \left(j + V_{gj}\right) \frac{\partial \rho_m}{\partial z} + \left(\rho_m - \rho_f\right) \frac{\partial V_{gj}}{\partial z} = - \rho_m \frac{\Gamma_g \Delta\rho}{\rho_f \rho_g} \tag{5.24}$$

Assume that V_{gj} can at best be a function of α only. In that case,

$$\frac{\partial V_{gj}}{\partial z} = \frac{\partial V_{gj}}{\partial \alpha} \frac{\partial \alpha}{\partial z} = - \frac{1}{\Delta\rho} \frac{\partial V_{gj}}{\partial \alpha} \frac{\partial \rho_m}{\partial z} \tag{5.25}$$

Substituting equation (5.25) into equation (5.24), one can finally transform the mixture continuity equation to the Lagrangian form and it is given in terms of kinematic wave velocity, C_k:

$$\frac{\partial \rho_m}{\partial t} + C_k \frac{\partial \rho_m}{\partial z} = - \rho_m \frac{\Gamma_g \Delta\rho}{\rho_f \rho_g} \tag{5.26}$$

where

$$C_k = j + V_{gj} + \alpha \frac{\partial V_{gj}}{\partial \alpha} \tag{5.27}$$

Equation (5.26) is called the Density Propagation Equation.

For bubbly churn and slug flow, V_{gj} is independent of α [39].

Reproduced with permission of the copyright owner. Further reproduction prohibited without permission.

Therefore,

$$C_k = j + V_{gj} \tag{5.28}$$

For other flow regimes, like the annular or the mist flow, we assume:

$$\alpha \frac{\partial V_{gj}}{\partial \alpha} \ll j + V_{gj} \tag{5.29}$$

Therefore, the density propagation equation can be written as:

$$\frac{\partial \rho_m}{\partial t} + (j + V_{gj}) \frac{\partial \rho_m}{\partial z} = - \rho_m \frac{\Gamma_g \Delta \rho}{\rho_f \rho_g} \tag{5.30}$$

The expression for $\frac{\partial v_m}{\partial z}$, i.e., equation (5.23), has been derived from the vapor phase continuity equation (5.6). However, in the present form, it is not convenient for obtaining a solution. From the identity (5.22):

$$\frac{\partial v_m}{\partial z} = \frac{\partial j}{\partial z} + \frac{\partial V_{gj}}{\partial z} - \frac{\partial}{\partial z}\left[\frac{\rho_f}{\rho_m} V_{gj}\right] \tag{5.31}$$

Comparing equations (5.23) and (5.31), one obtains:

$$\frac{\partial j}{\partial z} = \frac{\Gamma_g \Delta \rho}{\rho_f \rho_g} \tag{5.32}$$

This is the equation for volumetric flux density, j, which according to the above equation, increases along the direction of the flow solely due

Reproduced with permission of the copyright owner. Further reproduction prohibited without permission.

to the phase change. This equation replaces the continuity equation for the vapor phase in the present analysis.

It has been mentioned before that, in the present analysis, the mixture density, ρ_m, is a function of void fraction only. Since the phase densities are constant, it can be seen from equations (4.33) and (4.47) that the void fraction does not explicitly depend on pressure. Therefore, in the present case, the mixture density is not a function of pressure. This allows us to decouple the momentum equation from the continuity and energy equations. In other words, the kinematics of the flow can be solved first without considering the dynamics. This, however, could not be done for the analysis of acoustic instabilities, because in that case the effect of pressure wave propagation on the mixture density could not be neglected.

In summary, we now have the following:

Equation for volumetric flux density,

$$\frac{\partial j}{\partial z} = \frac{\Gamma_g \, \Delta\rho}{\rho_f \, \rho_g} \tag{5.32}$$

Density propagation equation,

$$\frac{\partial \rho_m}{\partial t} + \left(j + V_{gj}\right) \frac{\partial \rho_m}{\partial z} = -\rho_m \frac{\Gamma_g \, \Delta\rho}{\rho_f \, \rho_g} \tag{5.30}$$

and the identity,

$$v_m \equiv j - \left(\frac{\rho_f}{\rho_m} - 1\right) V_{gj} \tag{5.22}$$

Reproduced with permission of the copyright owner. Further reproduction prohibited without permission.

Therefore, if the vapor drift velocity, V_{gj}, and the mass rate of vapor generation per unit volume, Γ_g, can be specified, we can solve the above set of equations to determine j, ρ_m, and v_m. We can then find the pressure drop by integrating the momentum equation (5.7). This essentially completes the formulation of the problem.

The difficulties of determining the mass rate of vapor generation per unit area, Γ_g, in a formal way, have been enumerated in section IV-5. In the same section, a constitutive relation for the rate of vapor generation, equation (4.47), has been derived from an assumed liquid bulk enthalpy distribution. Recognizing that the boiling boundary, λ, is a function of time during flow oscillations, we can modify the constitutive equation of section IV-5 as:

$$\Gamma_g = \frac{\dot{q}''_w \xi_h}{A_c \Delta i_{fg}} \left[1 - \exp\left\{ - \frac{z - \lambda(t)}{\Delta \ell} \right\} \right] \tag{5.33}$$

where the characteristic length $\Delta \ell$ still corresponds to the steady state characteristic length $(\bar{\lambda}_{eq} - \bar{\lambda})$.

The above formulation is similar to that of Ishii [2]. However, there are two prime differences between the present analysis and that of Ishii, because Ishii assumed the thermodynamic equilibrium model. According to the equilibrium model, vapor generation starts at a distance λ_{eq} from the inlet of the heated channel and the mass rate of vapor generation per unit volume is:

$$\Gamma_{g,eq} = \frac{\dot{q}''_w \xi_h}{A_c \Delta i_{fg}} \tag{5.34}$$

Reproduced with permission of the copyright owner. Further reproduction prohibited without permission.

In the present model, i.e., thermodynamic non-equilibrium model, vapor generation starts at a distance λ from the inlet and the mass rate of vapor generation per unit volume, in view of equation (5.34), becomes:

$$\Gamma_g = \Gamma_{g,eq}\left[1 - \exp\left\{-\frac{z-\lambda}{a\ell}\right\}\right] \tag{5.35}$$

For better understanding, the contrast between the two models is depicted in Figure 17.

V-2. Method of Solution

As mentioned earlier, there are two approaches that can be followed to obtain a solution of the instability problem. In the first approach, the system of nonlinear governing equations is linearized by assuming a small disturbance around a steady state situation. The system response to various perturbations, as well as the stability criterion, is then obtained by using standard techniques of control theory. In the second case, the set of nonlinear partial differential equations is solved by numerical technique.

The objective of the present analysis is to predict the system stability boundary; not the ultimate system behavior in the unstable region. According to the Liapunov theorem [45], the stability of the linearized system corresponds to the stability of the nonlinear system operating under quasi-equilibrium conditions. On the basis of this theorem and several other instability analyses [2,13,16,46], the linearization technique is chosen in this analysis. The disturbance shall be

Reproduced with permission of the copyright owner. Further reproduction prohibited without permission.

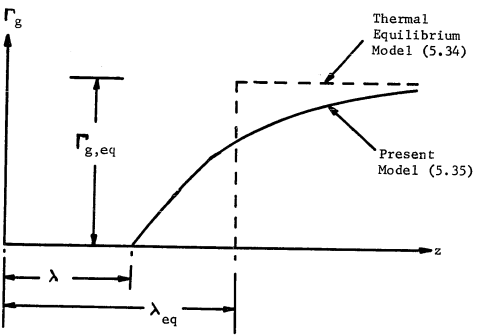

Figure 17. Comparison between the Present Non-Equilibrium Model and the Equilibrium Model for the Rate of Vapor Generation

Reproduced with permission of the copyright owner. Further reproduction prohibited without permission.

given in the form of an inlet velocity perturbation, and the following boundary and initial conditions are imposed on the density, pressure, enthalpy, and velocity:

$$\rho_f = \rho_f(P_s) \qquad \text{at } z = 0,\ t \geq 0 \qquad (5.36)$$

$$P = P_s = \text{Constant} \qquad \text{at } z = 0,\ t \geq 0 \qquad (5.37)$$

$$i_f = i_1 = \text{Constant} \qquad \text{at } z = 0,\ t \geq 0 \qquad (5.38)$$

$$v_f = v_{fi}(t) = \bar{v}_{fi} + \delta v_{fi}(t) \qquad \text{at } z = 0,\ t \geq 0 \qquad (5.39)$$

The steady state inlet velocity is denoted by $\bar{v}_{fi}$ and the perturbation on the velocity is given by $\delta v_{fi}(t)$. As the frequency response method shall be used in the current analysis, the inlet velocity perturbation is taken in the form:

$$\delta v_{fi}(t) = \epsilon e^{st} \qquad (5.40)$$

where $s = \alpha + j\omega$; $j = \sqrt{-1}$

(This j should not be confused with the volumetric flux density.)

In equation (5.40), s is a complex number, the real part gives the amplification coefficient of the particular oscillation mode, whereas the imaginary part represents the angular frequency ω. It is assumed that $\epsilon/\bar{v}_{fi}$ is much smaller than unity, i.e., ϵ is infinitesimal compared to

Reproduced with permission of the copyright owner. Further reproduction prohibited without permission.

finite $\bar{v}_{fi}$. In the following analysis, therefore, only the first order terms in ϵ shall be retained; the second and higher order terms shall be neglected.

As mentioned before, in the present case, the kinematics of the flow, i.e., the density and velocity fields can be solved first. Then the momentum equation can be integrated to obtain the system characteristic equation.

V-3. Kinematics of the Flow

Single-Phase Liquid Region

The continuity equation with constant phase density is:

$$\frac{\partial v_f}{\partial z} = 0 \tag{5.2}$$

Integrating the above equation and using the boundary condition (5.39), one obtains:

$$v_f = v_f(t) = v_{fi}(t) = \bar{v}_{fi} + \epsilon e^{st} \tag{5.41}$$

That is, the fluid velocity in the single-phase region is a function of time only.

As mentioned earlier, the model developed in section IV-3 shall be used to determine the starting point of the two-phase mixture region, i.e., the boiling boundary between the single-phase liquid region and the two-phase mixture region. The energy equation in the single-phase region is:

Reproduced with permission of the copyright owner. Further reproduction prohibited without permission.

$$\frac{\partial i_f}{\partial t} + v_f \frac{\partial i_f}{\partial z} = \frac{\dot{q}''_w \xi_h}{\rho_f A_c} \tag{5.4}$$

Using the method of characteristics, one can express the above equation as:

Along the particle path, i.e.,

$$\frac{dz}{dt} = v_f \quad , \tag{5.42}$$

$$di_f = \frac{\dot{q}''_w \xi_h}{\rho_f A_c} dt \tag{5.43}$$

Let a fluid particle enter the heated liquid region at time τ_1. Therefore, in view of (5.38), the boundary condition is:

$$i_f = i_1 \quad \text{at} \quad t = \tau_1 \quad \text{and} \quad z = 0 \tag{5.44}$$

Integrating equations (5.43) and (5.42), assuming a uniform heat flux distribution, $\dot{q}''_w$, and using the above boundary condition, one obtains:

$$(i_f - i_1) = \frac{\dot{q}''_w \xi_h}{\rho_f A_c} (t - \tau_1) \tag{5.45}$$

and

$$z = \bar{v}_{fi} (t - \tau_1) + \epsilon e^{st} \frac{\left[1 - e^{-s(t-\tau_1)}\right]}{s} \tag{5.46}$$

As discussed in section IV-3, the boiling boundary is the point where the liquid bulk enthalpy attains a value of i_λ, which can be determined from equation (4.18) or (4.19) depending on the flow Peclet number. The

Reproduced with permission of the copyright owner. Further reproduction prohibited without permission.

distance of this point from the inlet is λ. Let the fluid particle that entered the heated liquid region at time τ_1, reach the boiling boundary at time τ_2. Therefore, from equation (5.45):

$$(i_\lambda - i_1) = \frac{\dot{q}''_w \xi_h}{\rho_f A_c} (\tau_2 - \tau_1) \tag{5.47}$$

or the residence time of the fluid particle in the single-phase region τ_{12}, is:

$$\tau_{12} = \tau_2 - \tau_1 = \frac{\rho_f A_c}{\dot{q}''_w \xi_h} (i_\lambda - i_1) \tag{5.48}$$

The distance of the boiling boundary from the inlet is obtained from (5.46):

$$\lambda(t) = \bar{v}_{fi} \tau_{12} + \epsilon e^{st} \frac{\left[1 - e^{-s\tau_{12}}\right]}{s} \tag{5.49}$$

It can be noted from equations (4.18) and (4.19) that, in the case of Pe $<$ 70,000, i_λ is independent of the inlet velocity, whereas for Pe $>$ 70,000, i_λ does depend on the inlet velocity. Therefore, from equation (5.48), the residence time, τ_{12}, can be a function of inlet velocity if the Peclet number is greater than 70,000. In general, the residence time consists of a steady state part, $\bar{\tau}_{12}$, and a perturbed part, $\delta\tau_{12}$, i.e.,

$$\tau_{12} = \bar{\tau}_{12} + \delta\tau_{12} \tag{5.50}$$

Reproduced with permission of the copyright owner. Further reproduction prohibited without permission.

where

$$\bar{\tau}_{12} = \frac{P_f A_c (\bar{i}_\lambda - i_1)}{\dot{q}''_w S_h} = \frac{P_f A_c (\Delta i_{sub} - \overline{\Delta i}_\lambda)}{\dot{q}''_w S_h} \qquad (5.51)$$

$\overline{\Delta i}_\lambda$ is determined from equation (4.18) or (4.19); and,

$$\delta\tau_{12} = 0 \qquad \text{if} \quad Pe < 70{,}000 \qquad (5.52)$$

$$\delta\tau_{12} = 154 \frac{A_c}{S_h} \frac{\delta v_{fi}}{\bar{v}_{fi}^2} \qquad \text{if} \quad Pe > 70{,}000 \qquad (5.53)$$

Therefore, if the transfer function $\mathcal{L}_o$ is defined by $\frac{\delta\tau_{12}}{\delta v_{fi}}$,

$$\mathcal{L}_o = 0 \qquad \text{if} \quad Pe < 70{,}000 \qquad (5.54)$$

$$\mathcal{L}_o = 154 \frac{A_c}{S_h} \frac{1}{\bar{v}_{fi}^2} \qquad \text{if} \quad Pe > 70{,}000 \qquad (5.55)$$

Substituting (5.50) into equation (5.49), and resolving into the steady state and perturbed parts, neglecting the second and higher order terms in ϵ, one obtains:

$$\bar{\lambda} = \bar{v}_{fi} \bar{\tau}_{12} \qquad (5.56)$$

and

$$\delta\lambda(t) = \epsilon e^{st} \left[\bar{v}_{fi} \mathcal{L}_o + \frac{1}{s} \left\{ 1 - e^{-s\bar{\tau}_{12}} \right\} \right] \qquad (5.57)$$

Defining the transfer function $\mathcal{L}_1(s)$ such that,

$$\mathcal{L}_1(s) = \frac{\delta\lambda(t)}{\delta v_{fi}(t)} \qquad (5.58)$$

Reproduced with permission of the copyright owner. Further reproduction prohibited without permission.

one gets:

$$\mathcal{L}_1(s) = \bar{v}_{fi}\,\mathcal{L}_o + \frac{1}{s}\left[1 - e^{-s\bar{\tau}_{12}}\right] \qquad (5.59)$$

Therefore, in general, the boiling boundary can fluctuate due to two reasons: (a) fluctuation in the inlet velocity only, i.e., the second term in (5.59), and (b) fluctuation in the local subcooling at the boiling boundary due to an inlet flow fluctuation, i.e., the first term in (5.59). In the analysis, assuming thermodynamic equilibrium between the phases [2,16], only one term, similar to the second term in (5.59), appears.

All the above developments for the residence time and the boiling boundary make sense only if the inlet subcooling, Δi_{sub}, is greater than Δi_λ. On the other hand, if the inlet subcooling, Δi_{sub}, is lower than Δi_λ, it is assumed that boiling starts right from the inlet of the heated channel. In that case, one has:

$$\tau_{12} = 0 \quad , \quad \lambda(t) = 0 \quad \text{if} \quad \Delta i_{sub} < \Delta i_\lambda \qquad (5.60)$$

Consequently,

$$\bar{\tau}_{12} = 0 \quad , \quad \bar{\lambda} = 0 \qquad (5.61)$$

and

$$\mathcal{L}_o = 0 \quad , \quad \mathcal{L}_1(s) = 0 \qquad (5.62)$$

Reproduced with permission of the copyright owner. Further reproduction prohibited without permission.

Two-Phase Mixture Region

As developed in section V-1, the governing equations for the kinematics of the flow in the two-phase region are:

Equation for volumetric flux density:

$$\frac{\partial j}{\partial z} = \frac{\Gamma_g \Delta\rho}{\rho_g \rho_f} \tag{5.32}$$

Density propagation equation:

$$\frac{\partial \rho_m}{\partial t} + C_k \frac{\partial \rho_m}{\partial z} = -\rho_m \frac{\Gamma_g \Delta\rho}{\rho_g \rho_f} \tag{5.30}$$

where

$$C_k = j + \dot{V}_{gj} \tag{5.63}$$

and the constitutive equation for phase change:

$$\Gamma_g(z,t) = \Gamma_{g,eq}\left[1 - \exp\left\{-\frac{z-\lambda(t)}{\Delta l}\right\}\right] \tag{5.35}$$

Notice that $\frac{\Gamma_g \Delta\rho}{\rho_f \rho_g}$ has a dimension of frequency, and it is called the Characteristic Frequency of Phase Change, Ω. This is similar to the characteristic reaction frequency in a chemically reacting gas mixture system. Let Ω_{eq} be the characteristic frequency of phase change under the thermodynamic equilibrium assumption. In view of equation (5.35):

Reproduced with permission of the copyright owner. Further reproduction prohibited without permission.

$$\Omega(z,t) = \Gamma_g(z,t)\,\frac{\Delta\rho}{\rho_f\rho_g} = \Gamma_{g,eq}\,\frac{\Delta\rho}{\rho_f\rho_g}\left[1-\exp\left\{-\frac{z-\lambda(t)}{\Delta\ell}\right\}\right] \qquad (5.64)$$

$$= \Omega_{eq}\left[1-\exp\left\{-\frac{z-\lambda(t)}{\Delta\ell}\right\}\right]$$

Resolving the above equation into the steady state part and the perturbed part, one obtains:

$$\bar{\Omega}(z) = \Omega_{eq}\left[1-\exp\left\{-\frac{z-\bar{\lambda}}{\Delta\ell}\right\}\right] \qquad (5.65)$$

and

$$\delta\Omega(z,t) = -\Omega_{eq}\,e^{-\frac{z-\bar{\lambda}}{\Delta\ell}}\,\frac{\delta\lambda(t)}{\Delta\ell} \qquad (5.66)$$

It should be noticed that, in the equilibrium model, the characteristic frequency of phase change is a constant. However, in the present model, the characteristic frequency consists of a non-uniform steady part, i.e., equation (5.65), as well as a perturbed part, i.e., equation (5.66).

At the boiling boundary, the void fraction, α, is zero. Therefore, from the definition of volumetric flux density, i.e., equation (5.14):

$$j = v_f = v_{fi}(t) \qquad \text{at} \quad z = \lambda(t) \qquad (5.67)$$

Integrating equation (5.32) and utilizing the above boundary condition, one can write the steady state and the perturbed part, neglecting second and higher order terms, of the volumetric flux density, in general, as:

Reproduced with permission of the copyright owner. Further reproduction prohibited without permission.

$$\bar{j}(\bar{z}) = \bar{v}_{fi} + \int_{\bar{\lambda}}^{\bar{z}} \bar{\Omega}(\bar{z})\, d\bar{z} \tag{5.68}$$

and

$$\delta j(\bar{z},t) = \delta v_{fi}(t) - \bar{\Omega}(\bar{\lambda})\,\delta\lambda + \int_{\bar{\lambda}}^{\bar{z}} \delta\Omega(\bar{z},t)\, d\bar{z} \tag{5.69}$$

As mentioned earlier, V_{gj} is considered to be a constant along the length of the channel, and is assigned an average value of $\bar{V}_{gj}$. Therefore, in view of equations (5.63), (5.68), and (5.69), the steady state and the perturbed part of the kinematic wave velocity become:

$$\bar{C}_k(\bar{z}) = \bar{v}_{fi} + \bar{V}_{gj} + \int_{\bar{\lambda}}^{\bar{z}} \bar{\Omega}(\bar{z})\, d\bar{z} \tag{5.70}$$

and

$$\delta C_k(\bar{z},t) = \delta v_{fi}(t) - \bar{\Omega}(\bar{\lambda})\,\delta\lambda + \int_{\bar{\lambda}}^{\bar{z}} \delta\Omega(\bar{z},t)\, d\bar{z} \tag{5.71}$$

Now that the expression for kinematic wave velocity is known, the mixture density can be determined from the density propagation equation (5.30). For convenience of solution, a new variable, ϕ, is introduced such that:

$$\phi(\bar{z},t) = \ln\left[\frac{\rho_m(\bar{z},t)}{\rho_f}\right] \tag{5.72}$$

Resolving ϕ into the steady state and perturbed parts, one obtains:

$$\bar{\phi}(\bar{z}) + \delta\phi(\bar{z},t) = \ln\left[\frac{\bar{\rho}_m(\bar{z})}{\rho_f}\right] + \frac{\delta\rho_m(\bar{z},t)}{\bar{\rho}_m(\bar{z})} \tag{5.73}$$

Reproduced with permission of the copyright owner. Further reproduction prohibited without permission.

In view of equation (5.72), the density propagation equation (5.30) becomes:

$$\frac{\partial \phi(z,t)}{\partial t} + C_k(z,t)\,\frac{\partial \phi(z,t)}{\partial z} = -\Omega(z,t) \tag{5.74}$$

The steady state part of equation (5.74):

$$\bar{C}_k(z)\,\frac{d\bar{\phi}(z)}{dz} = -\bar{\Omega}(z) \tag{5.75}$$

Recognizing from equation (5.70) that,

$$\frac{d\bar{C}_k(z)}{dz} = \bar{\Omega}(z) \tag{5.76}$$

and, substituting (5.76) into (5.75), one obtains:

$$d\bar{\phi}(z) = -\frac{d\bar{C}_k(z)}{\bar{C}_k(z)} \tag{5.77}$$

The boundary condition is:

$$\bar{\phi}(z) = 0 \qquad at \qquad z = \bar{\lambda} \tag{5.78}$$

Integrating equation (5.77) and using the above boundary condition, one obtains the steady state solution for the mixture density as:

$$\bar{\phi}(z) = \ln\left[\frac{\bar{C}_k(\lambda)}{\bar{C}_k(z)}\right] \tag{5.79}$$

Reproduced with permission of the copyright owner. Further reproduction prohibited without permission.

or

$$\frac{\bar{\rho}_m(z)}{\rho_f} = \frac{\bar{C}_k(\lambda)}{\bar{C}_k(z)} = \frac{\bar{v}_{fi} + \bar{V}_{gj}}{\bar{v}_{fi} + \bar{V}_{gj} + \int_{\lambda}^{z} \bar{\Omega}(z)\, dz} \tag{5.80}$$

The perturbed part of equation (5.74), neglecting second order terms, and using equation (5.75), is:

$$\frac{\partial}{\partial t}\left[\delta\phi(z,t)\right] + \bar{C}_k(z)\frac{\partial}{\partial z}\left[\delta\phi(z,t)\right] = -\delta\Omega(z,t) + \frac{\bar{\Omega}(z)}{\bar{C}_k(z)}\delta C_k(z,t) \tag{5.81}$$

Using the method of characteristics, one can write equation (5.81) as:

Along
$$\frac{dz}{dt} = \bar{C}_k(z) \tag{5.82}$$

$$\frac{d}{dt}(\delta\phi) = -\delta\Omega(z,t) + \frac{\bar{\Omega}(z)}{\bar{C}_k(z)}\delta C_k(z,t) \tag{5.83}$$

or

$$d(\delta\phi) = \left[-\frac{\delta\Omega(z,t)}{\bar{C}_k(z)} + \frac{\bar{\Omega}(z)}{\left\{\bar{C}_k(z)\right\}^2}\delta C_k(z,t)\right] dz \tag{5.84}$$

Now, τ_2 is the time when the fluid particle enters the two-phase mixture region. Therefore, integrating (5.82), one gets

$$t - \tau_2 = \int_{\lambda(t)}^{z} \frac{dz}{\bar{C}_k(z)} \tag{5.85}$$

Defining a new function, E(z), such that:

$$E(z) = \int \frac{dz}{\bar{C}_k(z)} \tag{5.86}$$

Reproduced with permission of the copyright owner. Further reproduction prohibited without permission.

one can write equation (5.85) as:

$$t - \tau_2 = E(z) - E(\bar{\lambda}) - \frac{\delta\lambda(\tau_2)}{\bar{c}_k(\bar{\lambda})} \tag{5.87}$$

The above equation can be used to determine the residence time of the kinematic wave in the mixture region.

Now, defining the transfer functions $\mathcal{L}_2$ and $\mathcal{L}_3$ such that:

$$\mathcal{L}_2(z,s) = \frac{\delta\Omega(z,t)}{\delta v_{fi}(t)} \tag{5.88}$$

and

$$\mathcal{L}_3(z,s) = \frac{\delta C_k(z,t)}{\delta v_{fi}(t)} \tag{5.89}$$

and neglecting second and higher order terms in ϵ, one can write equation (5.84) as:

$$d(\delta\phi) = \epsilon e^{s\tau_2} e^{s[E(z)-E(\bar{\lambda})]} \left\{ -\frac{\mathcal{L}_2(z,s)}{\bar{c}_k(z)} + \frac{\mathcal{L}_3(z,s)}{[\bar{c}_k(z)]^2} \frac{d\bar{c}_k(z)}{dz} \right\} dz \tag{5.90}$$

Defining,

$$H(z,s) = \int e^{s[E(z)-E(\bar{\lambda})]} \left\{ -\frac{\mathcal{L}_2(z,s)}{\bar{c}_k(z)} + \frac{\mathcal{L}_3(z,s)}{[\bar{c}_k(z)]^2} \frac{d\bar{c}_k(z)}{dz} \right\} dz \tag{5.91}$$

and using the boundary condition,

$$\phi(\bar{\lambda}(\tau_2), \tau_2) = 0 \tag{5.92}$$

Reproduced with permission of the copyright owner. Further reproduction prohibited without permission.

one gets the solution to equation (5.90) as:

$$\delta\phi(\bar{z},\tau_2) = \epsilon e^{s\tau_2}\left[\frac{\bar{\Omega}(\bar{\lambda})\mathcal{L}_1(s)}{\bar{C}_k(\bar{z})} + \left\{H(\bar{z},s) - H(\bar{\lambda},s)\right\}\right] \quad (5.93)$$

In terms of the independent variables z and t, equation (5.93) becomes:

$$\delta\phi(\bar{z},t) = \epsilon e^{st}\, e^{-s\left[E(\bar{z})-E(\bar{\lambda})\right]}\left[\frac{\bar{\Omega}(\bar{z})\mathcal{L}_1(s)}{\bar{C}_k(\bar{z})} + \left\{H(\bar{z},s) - H(\bar{\lambda},s)\right\}\right] \quad (5.94)$$

From (5.73) and the steady state mixture density, i.e., equation (5.80), the perturbed part of the mixture density is given by:

$$\frac{1}{\rho_f}\frac{\delta\rho_m(\bar{z},t)}{\delta v_{fj}(t)} = \mathcal{L}_4(\bar{z},s) \quad (5.95)$$

$$= \left[\frac{\bar{C}_k(\bar{\lambda})}{\bar{C}_k(\bar{z})}\right] e^{-s\left[E(\bar{z})-E(\bar{\lambda})\right]}\left[\frac{\bar{\Omega}(\bar{\lambda})\mathcal{L}_1(s)}{\bar{C}_k(\bar{\lambda})} + \left\{H(\bar{z},s) - H(\bar{\lambda},s)\right\}\right]$$

Solution for the mixture velocity, v_m, can now be obtained from the identity:

$$v_m \equiv j - \left(\frac{\rho_f}{\rho_m} - 1\right) V_{gj} \quad (5.22)$$

Recalling the definition of C_k, i.e., equation (5.63), and neglecting second and higher order terms, one gets:

$$v_m(\bar{z},t) = \left[\bar{C}_k(\bar{z}) - \frac{\rho_f}{\bar{\rho}_m(\bar{z})}\bar{V}_{gj}\right] + \left[\delta C_k(\bar{z},t) + \frac{\rho_f}{\bar{\rho}_m^2(\bar{z})}\bar{V}_{gj}\,\delta\rho_m(\bar{z},t)\right] \quad (5.96)$$

Reproduced with permission of the copyright owner. Further reproduction prohibited without permission.

Using (5.80), (5.89), and (5.95), one can now write the steady state and the perturbed parts of the mixture velocity as:

$$\frac{\bar{v}_m(\bar{z})}{\bar{v}_{fi}} = \frac{\bar{C}_k(\bar{z})}{\bar{C}_k(\bar{1})} = \frac{\rho_f}{\bar{\rho}_m(\bar{z})} \tag{5.97}$$

and

$$\frac{\delta v_m(\bar{z},t)}{\delta v_{fi}(t)} = \mathcal{L}_5(\bar{z},s) = \mathcal{L}_3(\bar{z},s) + \left\{\frac{\bar{C}_k(\bar{z})}{\bar{C}_k(\bar{1})}\right\}^2 V_{gj}\, \mathcal{L}_4(\bar{z},s) \tag{5.98}$$

This completes the solution for the kinematics, i.e., the density and velocity fields, of the flow. One can now proceed to solve the dynamics, i.e., the pressure drop, of the system.

V-4. Dynamics of the Flow

In this section the procedure of Ishii [2] shall be followed.

Single-Phase Liquid Region

The inlet pressure drop is assumed to be solely due to the inlet restriction shown in Figure 16, and is given by:

$$\Delta P_i = k_i \rho_f v_{fi}^2 \tag{5.99}$$

Resolving into the steady state and perturbed part, and neglecting second order terms, one obtains:

$$\overline{\Delta P_i} = k_i \rho_f \bar{v}_{fi}^2 \tag{5.100}$$

Reproduced with permission of the copyright owner. Further reproduction prohibited without permission.

and

$$\delta \Delta P_i = 2 k_i \rho_f \bar{v}_{fi} \delta v_{fi}(t) \tag{5.101}$$

The pressure drop in the heated liquid region, ΔP_{12}, is obtained by integrating the momentum equation (5.3):

$$\Delta P_{12} = \int_0^{\bar{\lambda}+\delta\lambda} \left[\rho_f \left\{ \frac{\partial v_{fi}}{\partial t} + v_{fi} \frac{\partial v_{fi}}{\partial z} \right\} + \frac{f_f}{2D_h} \rho_f v_{fi}^2 + g \rho_f \right] dz \tag{5.102}$$

Resolving into the steady state and the perturbed parts, and neglecting the second order terms, one has:

$$\overline{\Delta P}_{12} = \rho_f \left[\frac{f_f}{2D_h} \bar{v}_{fi}^2 + g \right] \bar{\lambda} \tag{5.103}$$

and

$$\delta \Delta P_{12} = \rho_f \left[s\bar{\lambda} + \frac{f_f}{D_h} \bar{v}_{fi} \bar{\lambda} + \frac{f_f}{2D_h} \bar{v}_{fi}^2 \mathcal{L}_1(s) + g \mathcal{L}_1(s) \right] \delta v_{fi}(t) \tag{5.104}$$

Two-Phase Mixture Region

The pressure drop in the heated two-phase mixture region, ΔP_{24}, is obtained by integrating the mixture momentum equation (5.7):

$$\Delta P_{24} = \int_{\bar{\lambda}+\delta\lambda}^{\ell} \left\{ \rho_m \left[\frac{\partial v_m}{\partial t} + v_m \frac{\partial v_m}{\partial z} \right] + g \rho_m + \rho_m \frac{f_m}{2D_h} v_m^2 + \frac{\partial}{\partial z} \left[\frac{\rho_f - \rho_m}{\rho_m - \rho_g} \frac{\rho_f \rho_g}{\rho_m} V_{gj}^2 \right] \right\} dz \tag{5.105}$$

Reproduced with permission of the copyright owner. Further reproduction prohibited without permission.

The terms in the right hand side of the above equation can be identified as the local acceleration term, convective acceleration term, gravitational term, frictional term, and the drift term, respectively. For convenience, each term shall be considered separately, and shall be resolved into the steady state part and the perturbed part.

1. Local Acceleration Term

$$\Delta P_{24la} = \int_{\bar{\lambda}+\delta\lambda}^{\ell} \rho_m \frac{\partial v_m}{\partial t} \, dz \tag{5.106}$$

Using equation (5.98), and retaining only the first order terms in ϵ, one obtains:

the steady state part:

$$\overline{\Delta P}_{24la} = 0 \tag{5.107}$$

and the perturbed part:

$$\delta \Delta P_{24la} = \delta v_{fi}(t) \; \Lambda_8(s) \tag{5.108}$$

where

$$\Lambda_8(s) = \rho_f \, s \int_{\bar{\lambda}}^{\ell} \left[\frac{\bar{c}_k(\bar{\lambda})}{\bar{c}_k(z)} \right] \Lambda_5(z,s) \, dz \tag{5.109}$$

2. Convective Acceleration Term

$$\Delta P_{24ca} = \int_{\bar{\lambda}+\delta\lambda}^{\ell} \rho_m v_m \frac{\partial v_m}{\partial z} \, dz \tag{5.110}$$

Reproduced with permission of the copyright owner. Further reproduction prohibited without permission.

or

$$\Delta P_{24ca} = \left(\rho_m v_m^2\right)\Big|_{\bar{\lambda}+\delta\lambda}^{\ell} - \int_{\bar{\lambda}+\delta\lambda}^{\ell} v_m \frac{\partial}{\partial z}\left(\rho_m v_m\right) dz \tag{5.111}$$

Using the mixture continuity, i.e., equation (5.5), one obtains:

$$\Delta P_{24ca} = \left(\rho_m v_m^2\right)\Big|_{\bar{\lambda}+\delta\lambda}^{\ell} + \int_{\bar{\lambda}+\delta\lambda}^{\ell} \frac{\partial \rho_m}{\partial t} v_m \, dz \tag{5.112}$$

Now, using the solutions for the mixture density and the mixture velocity, as obtained in section V-3, one has:

the steady state part:

$$\overline{\Delta P}_{24ca} = \rho_f \bar{v}_{fi}^2 \left[\frac{\bar{c}_k(\ell)}{\bar{c}_k(\bar{\lambda})} - 1\right] \tag{5.113}$$

and the perturbed part:

$$\delta \Delta P_{24ca} = \delta v_{fi}(t)\, \mathcal{L}_9(s) \tag{5.114}$$

where

$$\mathcal{L}_9(s) = \rho_f \bar{v}_{fi}^2 \left\{ \mathcal{L}_4(\ell,s)\left[\frac{\bar{c}_k(\ell)}{\bar{c}_k(\bar{\lambda})}\right]^2 + \frac{2}{\bar{v}_{fi}}\left[\mathcal{L}_5(\ell,s) - 1\right] \right. \tag{5.115}$$
$$\left. + \frac{s}{\bar{v}_{fi}} \int_{\bar{\lambda}}^{\ell} \left[\frac{\bar{c}_k(z)}{\bar{c}_k(\bar{\lambda})}\right] \mathcal{L}_4(z,s)\, dz \right\}$$

3. Gravitational Term

$$\Delta P_{24g} = \int_{\bar{\lambda}+\delta\lambda}^{\ell} g \rho_m \, dz \tag{5.116}$$

Reproduced with permission of the copyright owner. Further reproduction prohibited without permission.

The steady state part:

$$\overline{\Delta P}_{24g} = g\rho_f \int_{\bar{\lambda}}^{\ell} \left[\frac{\bar{C}_k(\bar{\lambda})}{\bar{C}_k(\bar{z})} \right] dz \tag{5.117}$$

and the perturbed part:

$$\delta \Delta P_{24g} = \delta v_{fi}(t) \left[\mathcal{L}_{10}(s) - g\rho_f \mathcal{L}_1(s) \right] \tag{5.118}$$

where

$$\mathcal{L}_{10}(s) = g\rho_f \int_{\bar{\lambda}}^{\ell} \mathcal{L}_4(z,s)\, dz \tag{5.119}$$

4. Frictional Term

$$\Delta P_{24f} = \int_{\bar{\lambda}+\delta\lambda}^{\ell} \frac{f_m}{2D_h} \rho_m v_m^2 \, dz \tag{5.120}$$

$$= \int_{\bar{\lambda}}^{\ell} \frac{f_m}{2D_h} \rho_m v_m^2 \, dz - \frac{f_f}{2D_h} \rho_f v_f^2 \, \delta\lambda(t)$$

In general, the two-phase friction factor, f_m, may consist of a steady state part and a perturbed part. Therefore,

$$f_m = \bar{f}_m(\bar{z}) + \delta f_m(z,t) = \bar{f}_m(\bar{z}) + \mathcal{L}_7(z,s)\, \delta v_{fi}(t) \tag{5.121}$$

The steady state part of the frictional pressure drop:

Reproduced with permission of the copyright owner. Further reproduction prohibited without permission.

$$\overline{\Delta P}_{24f} = \int_{\bar{\lambda}}^{\ell} \frac{\bar{f}_m(\bar{z})}{2D_h} \rho_f \bar{v}_{fi}^2 \left[\frac{\bar{C}_k(\bar{z})}{\bar{C}_k(\bar{\lambda})} \right] d\bar{z} \tag{5.122}$$

and the perturbed part:

$$\delta \Delta P_{24f} = \delta v_{fi}(t) \left[\mathcal{L}_{11}(s) - \frac{f_f}{2D_h} \rho_f \bar{v}_{fi}^2 \mathcal{L}_1(s) \right] \tag{5.123}$$

where

$$\mathcal{L}_{11}(s) = \int_{\bar{\lambda}}^{\ell} \frac{1}{2D_h} \left\{ \bar{f}_m(\bar{z}) \rho_f \bar{v}_{fi}^2 \left[\frac{\bar{C}_k(\bar{z})}{\bar{C}_k(\bar{\lambda})} \right]^2 \mathcal{L}_4(\bar{z},s) \right. \tag{5.124}$$

$$\left. + 2\bar{f}_m(\bar{z}) \rho_f \bar{v}_{fi} \mathcal{L}_5(\bar{z},s) + \rho_f \bar{v}_{fi}^2 \left[\frac{\bar{C}_k(\bar{z})}{\bar{C}_k(\bar{\lambda})} \right] \mathcal{L}_7(\bar{z},s) \right\} d\bar{z}$$

5. Drift Term

$$\Delta P_{24d} = \int_{\bar{\lambda}+\delta\lambda}^{\ell} \frac{\partial}{\partial \bar{z}} \left\{ \frac{\rho_f - \rho_m}{\rho_m - \rho_g} \frac{\rho_f \rho_g}{\rho_m} V_{gj}^2 \right\} d\bar{z} \tag{5.125}$$

At the boiling boundary, i.e.,

$$\text{at} \quad \bar{z} = \bar{\lambda} + \delta\lambda \quad , \qquad \rho_m = \rho_f \tag{5.126}$$

Therefore,

$$\Delta P_{24d} = \frac{\rho_f - \rho_m(\ell,t)}{\rho_m(\ell,t) - \rho_g} \frac{\rho_f \rho_g}{\rho_m(\ell,t)} V_{gj}^2(\ell,t) \tag{5.127}$$

Reproduced with permission of the copyright owner. Further reproduction prohibited without permission.

For the case, $x \to 1$,

$$\frac{v_{gj}^2(\ell,t)}{\rho_m(\ell,t)-\rho_g} \approx \frac{\bar{V}_{gj}^2}{\rho_m(\ell,t)} \tag{5.128}$$

Therefore, the steady state part:

$$\overline{\Delta P}_{2d} = \left[\frac{\bar{C}_k(\ell)}{\bar{C}_k(\bar{x})}\right]\left[\frac{\bar{C}_k(\ell)}{\bar{C}_k(\bar{x})} - 1\right]\rho_g \bar{V}_{gj}^2 \tag{5.129}$$

and the perturbed part:

$$\delta\Delta P_{2d} = \delta v_{fi}(t)\ \mathcal{A}_{12}(s) \tag{5.130}$$

where

$$\mathcal{A}_{12}(s) = \left[\frac{\bar{C}_k(\ell)}{\bar{C}_k(\bar{x})}\right]\left[1 - 2\,\frac{\bar{C}_k(\ell)}{\bar{C}_k(\bar{x})}\right]\mathcal{A}_4(\ell,s)\,\rho_g\,\bar{V}_{gj}^2 \tag{5.131}$$

As in the inlet, the exit pressure drop is also assumed to be solely due to the exit restriction shown in Figure 16. Therefore,

$$\Delta P_e = k_e\,\rho_m(\ell,t)\,v_m^2(\ell,t) \tag{5.132}$$

The steady state part:

$$\overline{\Delta P}_e = k_e\,\rho_f\,\bar{v}_{fi}^2\left[\frac{\bar{C}_k(\ell)}{\bar{C}_k(\bar{x})}\right] \tag{5.133}$$

Reproduced with permission of the copyright owner. Further reproduction prohibited without permission.

and the perturbed part:

$$\delta \Delta P_e = \delta v_{fi}(t) \mathcal{A}_{13}(s) \tag{5.134}$$

where

$$\mathcal{A}_{13}(s) = k_e \rho_f \bar{v}_{fi}^2 \left\{ \left[\frac{\bar{c}_k(t)}{\bar{c}_k(\lambda)} \right]^2 \mathcal{A}_4(t,s) + \frac{2}{\bar{v}_{fi}} \mathcal{A}_5(t,s) \right\} \tag{5.135}$$

Therefore, the steady state channel pressure drop is obtained by adding (5.100), (5.103), (5.107), (5.113), (5.117), (5.122), (5.129), and (5.133):

$$\overline{\Delta P}_s = \overline{\Delta P}_i + \overline{\Delta P}_{12} + \overline{\Delta P}_{24a} + \overline{\Delta P}_{24a} + \overline{\Delta P}_{24g} + \overline{\Delta P}_{24f} + \overline{\Delta P}_{24d} + \overline{\Delta P}_e \tag{5.136}$$

Similarly, the perturbed part of the channel, i.e., system, pressure drop is obtained by adding equations (5.101), (5.104), (5.108), (5.114), (5.118), (5.123), (5.130), and (5.134):

$$\delta \Delta P_s = Q(s) \delta v_{fi}(t) \tag{5.137}$$

where

Reproduced with permission of the copyright owner. Further reproduction prohibited without permission.

$$Q(s) = 2k_i \rho_f \bar{v}_{fi} + \rho_f \left[s\bar{\lambda} + \frac{f_f}{D_h} \bar{v}_{fi} \bar{\lambda} \right] \qquad (5.138)$$

$$+ \mathcal{L}_8(s) + \mathcal{L}_9(s) + \mathcal{L}_{10}(s)$$

$$+ \mathcal{L}_{11}(s) + \mathcal{L}_{12}(s) + \mathcal{L}_{13}(s)$$

Equation (5.137), along with equation (5.138), gives the response of the system pressure drop to the inlet flow fluctuation.

V-5. General Characteristic Equation

In the previous section, an expression for the perturbation of system pressure drop has been obtained by assuming a small fluctuation in the inlet velocity. In reality, however, it is the fluctuation in system pressure drop that causes a variation in the inlet flow. Therefore, equation (5.137) can be rewritten as:

$$\delta v_{fi} = \left[\frac{1}{Q(s)} \right] \delta \Delta P_s \qquad (5.139)$$

where Q(s) is given by equation (5.138).

In terms of control theory, $\delta \Delta P_s$ is the generalized input force, δv_{fi} is the output displacement, and $1/Q(s)$ is the system transfer function. Asymptotic stability of this system can be determined by the nature of the roots of the characteristic equation:

$$Q(s) = 0 \qquad (5.140)$$

Reproduced with permission of the copyright owner. Further reproduction prohibited without permission.

Therefore, at this point, the problem reduces to examining the nature of the roots in the complex s-plane for the above characteristic equation. If the characteristic equation has all its roots in the left half of the s-plane, every component of disturbance tends to zero as time approaches infinity. This is the necessary condition for the asymptotic stability, because if the characteristic equation has a root with positive real part, the disturbance grows with time, and eventually the system becomes unstable.

In view of the assumption of flat pump characteristic, i.e., equation (5.1), the condition for the excursive stability becomes:

$$\lim_{s \to 0} \frac{\delta \Delta P_s}{\delta v_{fi}} > 0 \tag{5.141}$$

or, in other words:

$$\lim_{s \to 0} Q(s) > 0 \tag{5.142}$$

V-6. Determination of Transfer Functions

It can be seen from equation (5.138) that, to solve the instability problem, it is now necessary to be able to obtain analytical expressions for various transfer functions, namely $\mathcal{L}_8(s)$ through $\mathcal{L}_{13}(s)$. During the present investigation, sincere efforts had been made to use the exponential form of the rate of vapor generation per unit volume, i.e., equation (5.35), to evaluate these transfer functions. Unfortunately, none of those efforts was fruitful. In fact, even the transfer function for

Reproduced with permission of the copyright owner. Further reproduction prohibited without permission.

the perturbation of mixture density, i.e., $\mathcal{A}_4(z,s)$, could not be determined due to the severe complexity involved in the integration defined in equation (5.91). Therefore, the two-phase mixture region has been divided into two regions as shown in Figure 18. In the first region, i.e., region C, Γ_g increases linearly up to a value of $\Gamma_{g,D}$. In the second region, i.e., region D, Γ_g remains constant at $\Gamma_{g,D}$. The physical basis of this partitioning is described below:

In region C, i.e., $\lambda \leq z \leq \lambda + \Delta\ell_c$,

$$\Gamma_{g,C}(z,t) = \Gamma_{g,eq}\left[\frac{z-\lambda(t)}{\Delta\ell}\right] \tag{5.143}$$

Note that the slope of the above distribution at the boiling boundary is the same as that of the exponential distribution.

In region D, i.e., $\lambda + \Delta\ell_c \leq z \leq \ell$,

$$\Gamma_{g,D} = \Gamma_{g,eq}\frac{\Delta\ell_c}{\Delta\ell} \tag{5.144}$$

The boundary between the two regions, i.e., the distance $\Delta\ell_c$ from the boiling boundary, is determined such that the steady state exit vapor quality under the present approximate model remains the same under the original exponential model. That is:

$$\int_{\bar{\lambda}}^{\ell}\Gamma_g(z)\,dz = \int_{\bar{\lambda}}^{\bar{\lambda}+\Delta\ell_c}\Gamma_{g,C}(z)\,dz + \int_{\bar{\lambda}+\Delta\ell_c}^{\ell}\Gamma_{g,D}\,dz \tag{5.145}$$

Reproduced with permission of the copyright owner. Further reproduction prohibited without permission.

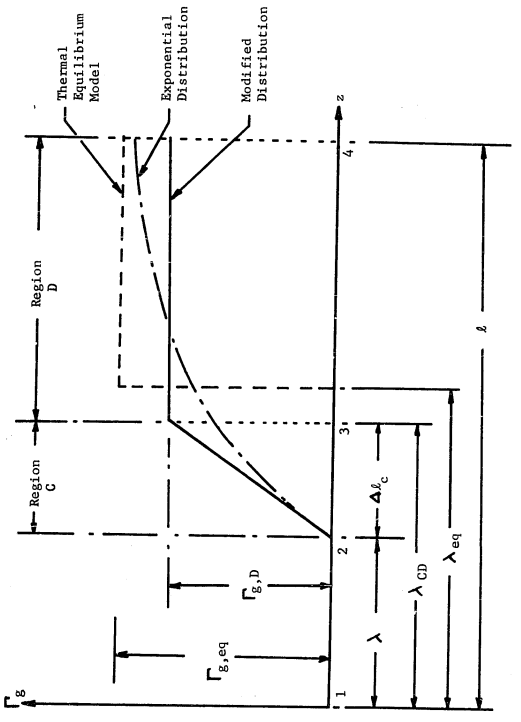

Figure 18. Modified Distribution for the Rate of Vapor Generation

Reproduced with permission of the copyright owner. Further reproduction prohibited without permission.

or

$$\int_{\bar{\lambda}}^{t}\left[1-e^{-\frac{z-\bar{\lambda}}{\Delta t}}\right]dz = \int_{\bar{\lambda}}^{\bar{\lambda}+\Delta t_c}\frac{z-\bar{\lambda}}{\Delta t}\,dz + \int_{\bar{\lambda}+\Delta t_c}^{t}\left(\frac{\Delta t_c}{\Delta t}\right)dz \qquad (5.146)$$

From the above equation, the physically realistic solution for Δt_c is:

$$\Delta t_c = (t-\bar{\lambda}) - \sqrt{(t-\bar{\lambda})^2 - 2\Delta t\left[(t-\bar{\lambda}) - \Delta t\left\{1-e^{-\frac{t-\bar{\lambda}}{\Delta t}}\right\}\right]} \qquad (5.147)$$

Analysis in Region C

In view of equation (5.143), the steady state and the perturbed part of the characteristic frequency of phase change in region C can be given by:

$$\bar{\Omega}_c(z) = \Omega_{eq}\left[\frac{z-\bar{\lambda}}{\Delta t}\right] \qquad (5.148)$$

and

$$\delta\Omega_c(t) = \mathcal{L}_{2,C}(s)\,\delta v_{fi}(t) = -\Omega_{eq}\frac{\mathcal{L}_1(s)}{\Delta t}\,\delta v_{fi}(t) \qquad (5.149)$$

Therefore, in view of equations (5.70) and (5.71), the steady state and the perturbed part of the kinematic wave velocity become:

$$\bar{C}_k(z) = \bar{C}_k(\bar{\lambda}) + \frac{1}{2}\Omega_{eq}\Delta t\left[\frac{z-\bar{\lambda}}{\Delta t}\right]^2 \qquad (5.150)$$

where

$$\bar{C}_k(\bar{\lambda}) = \bar{v}_{fi} + \bar{v}_{gj} \qquad (5.151)$$

and

$$\delta C_k(z,t) = \mathcal{L}_{3,C}(z,s)\,\delta v_{fi}(t) = \left[1-\bar{\Omega}_c(z)\mathcal{L}_1(s)\right]\delta v_{fi}(t) \qquad (5.152)$$

Reproduced with permission of the copyright owner. Further reproduction prohibited without permission.

The solution for the steady state mixture density, therefore, becomes:

$$\frac{\bar{\rho}_m(\bar{z})}{\rho_f} = \frac{\bar{C}_k(\bar{\lambda})}{\bar{C}_k(\bar{\lambda}) + \frac{1}{2}\Omega_{eq}\,\Delta\ell\left[\frac{\bar{z}-\bar{\lambda}}{\Delta\ell}\right]^2} \tag{5.153}$$

The perturbed part of the mixture density is evaluated following the solution procedure developed in section V-3. However, to keep the integration tractable, the condition that $\frac{\bar{z}-\bar{\lambda}}{\Delta\ell}$ is smaller than unity has been invoked. The final expression for the transfer function, $\mathcal{L}_{4,C}$, which describes the perturbation of the mixture density in region C, is given by:

$$\mathcal{L}_{4,C}(\bar{z},s) = \frac{1}{\rho_f}\,\frac{\delta\rho_m(\bar{z},t)}{\delta v_{fi}(t)} \tag{5.154}$$

$$= \left[\frac{\bar{C}_k(\bar{\lambda})}{\bar{C}_k(\bar{z})}\right]\left\{\frac{\Omega_{eq}\,\mathcal{L}_1(s)}{\bar{C}_k(\bar{\lambda})}\left(\frac{\bar{z}-\bar{\lambda}}{\Delta\ell}\right) + \left[1 - s\mathcal{L}_1(s)\right]\frac{1}{2}\,\frac{\Omega_{eq}\,\Delta\ell}{\left\{\bar{C}_k(\bar{\lambda})\right\}^2}\left(\frac{\bar{z}-\bar{\lambda}}{\Delta\ell}\right)^2\right\}$$

In view of equations (5.97) and (5.98), the steady state part and the perturbed part of the mixture velocity can be given by:

$$\bar{v}_m(\bar{z}) = \bar{v}_{fi}\,\frac{\bar{C}_k(\bar{z})}{\bar{C}_k(\bar{\lambda})} \tag{5.155}$$

and

$$\mathcal{L}_{5,C}(\bar{z},s) = \frac{\delta v_m(\bar{z},t)}{\delta v_{fi}(t)} \tag{5.156}$$

$$= 1 - \Omega_{eq}\left(\frac{\bar{z}-\bar{\lambda}}{\Delta\ell}\right)\mathcal{L}_1(s) + \left\{\frac{\bar{C}_k(\bar{z})}{\bar{C}_k(\bar{\lambda})}\right\}\bar{V}_{gj}\,\mathcal{L}_{4,C}(\bar{z},s)$$

Reproduced with permission of the copyright owner. Further reproduction prohibited without permission.

Analysis in Region D

In this region, the characteristic frequency of phase change is a constant, i.e.,

$$\bar{\Omega}_D = \Omega_D = \Omega_{eq} \frac{\Delta l_c}{\Delta l} = \Omega_{eq}\, l_c^* \tag{5.157}$$

and

$$\delta\Omega_D = \mathcal{L}_{2,D}\, \delta v_{fi} = 0 \tag{5.158}$$

Due to the "rigidness" of the modified Γ_g profile, the boundary between the region C and the region D fluctuates in the same was as the boiling boundary, i.e.,

$$\delta\lambda_{CD}(t) = \delta\lambda(t) = \mathcal{L}_1(s)\, \delta v_{fi}(t) \tag{5.159}$$

Therefore, the steady state and the perturbed part of the kinematic wave velocity can be written as:

$$\bar{C}_k(z) = \bar{C}_k(\bar{\lambda}_{CD}) + \Omega_D(z - \bar{\lambda}_{CD}) \tag{5.160}$$

where

$$\bar{C}_k(\bar{\lambda}_{CD}) = \bar{C}_k(\bar{\lambda}) + \tfrac{1}{2}\Omega_{eq}\Delta l\,(l_c^*)^2 \tag{5.161}$$

and

$$\delta C_k(t) = \mathcal{L}_{3,D}(s)\, \delta v_{fi}(t) = \left[1 - \Omega_D \mathcal{L}_1(s)\right] \delta v_{fi}(t) \tag{5.162}$$

The steady state mixture density is, therefore:

Reproduced with permission of the copyright owner. Further reproduction prohibited without permission.

$$\frac{\bar{\rho}_m(z)}{\rho_f} = \frac{\bar{c}_k(\bar{x})}{\bar{c}_k(\bar{x}_{cD}) + \Omega_D (z - \bar{x}_{cD})} \tag{5.163}$$

The perturbed part of the mixture density is finally expressed as:

$$\mathcal{A}_{4,D}(z,s) = \frac{1}{\rho_f} \frac{\delta \rho_m(z,t)}{\delta v_{fi}(t)} = \left[\frac{\bar{c}_k(\bar{x})}{\bar{c}_k(\bar{x}_{cD})}\right] \left\{ \left[\frac{\bar{c}_k(z)}{\bar{c}_k(\bar{x}_{cD})}\right]^{-\frac{s}{\Omega_D}-1} K(s) \right. \tag{5.164}$$

$$\left. + \mathcal{A}_{3,D}(s) \frac{\Omega_D}{s - \Omega_D} \frac{1}{\bar{c}_k(\bar{x}_{cD})} \left[\left\{ \frac{\bar{c}_k(z)}{\bar{c}_k(\bar{x}_{cD})} \right\}^{-2} - \left\{ \frac{\bar{c}_k(z)}{\bar{c}_k(\bar{x}_{cD})} \right\}^{-\frac{s}{\Omega_D}-1} \right] \right\}$$

where

$$K(s) = \frac{\Omega_{eq} \mathcal{A}_1(s) \ell_c^*}{\bar{c}_k(\bar{x})} + \left[1 - s\mathcal{A}_1(s)\right] \frac{1}{2} \frac{\Omega_{eq} \Delta\ell}{\left\{\bar{c}_k(\bar{x})\right\}^2} \left(\ell_c^*\right)^2 \tag{5.165}$$

For thermodynamic equilibrium model,

$$\Delta\ell = 0 \qquad ; \qquad \ell_c^* = 1 \tag{5.166}$$

Substituting (5.166) into (5.165) and (5.164), one can get exactly what Ishii obtained assuming equilibrium model (equation VIII.6 in reference 2).

The steady state and the perturbed part of the mixture velocity are given by:

$$\bar{v}_m(z) = \bar{v}_{fi} \frac{\bar{c}_k(z)}{\bar{c}_k(\bar{x})} \tag{5.167}$$

and

Reproduced with permission of the copyright owner. Further reproduction prohibited without permission.

$$\mathcal{L}_{5,D}(\bar{z},s) = \frac{\delta v_m(\bar{z},t)}{\delta v_{fi}(t)} = \mathcal{L}_{3,D}(s)\left[1+\frac{\bar{v}_{gj}}{\bar{c}_k(\bar{x})}\frac{\Omega_D}{s-\Omega_D}\right] \qquad (5.168)$$

$$+\frac{\bar{c}_k(\bar{x}_{cD})}{\bar{c}_k(\bar{x})}\left[\frac{\bar{c}_k(\bar{z})}{\bar{c}_k(\bar{x}_{cD})}\right]^{-\frac{s}{\Omega_D}+1}\bar{v}_{gj}\left\{K(s)-\mathcal{L}_{3,D}(s)\frac{\Omega_D}{s-\Omega_D}\frac{1}{\bar{c}_k(\bar{x}_{cD})}\right\}$$

Transfer Functions $\mathcal{L}_8(s)$ through $\mathcal{L}_{13}(s)$

Now that the perturbation of mixture density and mixture velocity has been determined in both regions C and D, the transfer functions $\mathcal{L}_8(s)$ through $\mathcal{L}_{13}(s)$ can be evaluated from the integrals presented in section V-4. For the two-phase friction factor, f_m, a lumped parameter model shall be taken.

In region C:

$$f_{m,c} = \bar{C}_{m,c}\, f_f \qquad (5.169)$$

and in region D:

$$f_{m,D} = \bar{C}_{m,D}\, f_f \qquad (5.170)$$

where $\bar{C}_{m,c}$ and $\bar{C}_{m,D}$ are two constants, not necessarily of the same value. Note that there is no perturbed part of the friction factor, i.e., $\mathcal{L}_7(\bar{z},s) = 0$.

The final expressions for the required transfer functions are:

Reproduced with permission of the copyright owner. Further reproduction prohibited without permission.

$$\mathcal{A}_8(s) = \rho_f s \left[\frac{\Delta l}{\sqrt{\frac{1}{2}\frac{\Omega_{eq}\Delta l}{\bar{c}_k(\bar{x})}}} \tan^{-1}\left(l_c^* \sqrt{\frac{1}{2}\frac{\Omega_{eq}\Delta l}{\bar{c}_k(\bar{x})}} \right) - \right. \tag{5.171}$$

$$\left. \mathcal{A}_1(s)\, \bar{c}_k(\bar{x}) \ln\left(c^*_{k,cD}\right) \right]$$

$$+ \rho_f \bar{v}_{gj} s \left[\frac{\mathcal{A}_1(s)\Omega_{eq}\Delta l}{2\,\bar{c}_k(\bar{x})} \left(l_c^*\right)^2 + \left\{ 1 - s\mathcal{A}_1(s) \right\} \frac{1}{6} \frac{\Omega_{eq}(\Delta l)^2}{\left\{\bar{c}_k(\bar{x})\right\}^2} \left(l_c^*\right)^3 \right]$$

$$+ \rho_f \frac{s}{\Omega_D} \bar{c}_k(\bar{x})\, \mathcal{A}_{3,D}(s) \left[1 + \frac{\bar{v}_{gj}}{\bar{c}_k(\bar{x})} \frac{\Omega_D}{s-\Omega_D} \right] \ln\left(c^*_{k,DE}\right)$$

$$+ \rho_f \bar{v}_{gj} \frac{s}{s-\Omega_D} \left[K(s)\, \bar{c}_k(\bar{x}_{cD}) - \mathcal{A}_{3,D}(s) \frac{\Omega_D}{s-\Omega_D} \right] \left[1 - c^*_{k,DE} e^{-s\bar{\tau}_{34}} \right]$$

where

$$c^*_{k,cD} = \frac{\bar{c}_k(\bar{x}_{cD})}{\bar{c}_k(\bar{x})} \tag{5.172}$$

$$c^*_{k,DE} = \frac{\bar{c}_k(\ell)}{\bar{c}_k(\bar{x}_{cD})} \tag{5.173}$$

$$\bar{\tau}_{34} = \frac{1}{\Omega_D} \ln\left[\frac{\bar{c}_k(\ell)}{\bar{c}_k(\bar{x}_{cD})} \right] \tag{5.174}$$

$$\mathcal{A}_9(s) = \rho_f \bar{v}_{fi}^2 \left[c^*_{k,cD} \left\{ c^*_{k,DE} e^{-s\bar{\tau}_{34}} K(s) \right. \right. \tag{5.175}$$

$$\left. + \mathcal{A}_{3,D}(s) \frac{\Omega_D}{s-\Omega_D} \frac{1}{\bar{c}_k(\bar{x}_{cD})} \left(1 - c^*_{k,DE} e^{-s\bar{\tau}_{34}} \right) \right\}$$

$$+ \frac{2}{\bar{v}_{fi}} \left\{ \mathcal{A}_{3,D}(s) \left[1 + \frac{\bar{v}_{gj}}{\bar{c}_k(\bar{x})} \frac{\Omega_D}{s-\Omega_D} \right] + c^*_{k,cD} c^*_{k,DE} e^{-s\bar{\tau}_{34}} \bar{v}_{gj} \right. \cdot$$

(continued)

Reproduced with permission of the copyright owner. Further reproduction prohibited without permission.

$$\left(K(s) - \mathcal{L}_{3,D}(s)\frac{\Omega_D}{s-\Omega_D}\frac{1}{\bar{C}_k(\bar{\lambda}_{cD})}\right) - 1\Bigg\} + \frac{1}{\bar{v}_{fi}}\left\{\frac{s\mathcal{L}_1(s)\Omega_{eq}\Delta l}{2\bar{C}_k(\bar{\lambda})}(l_c^*)^2\right.$$

$$+\left[s - s^2\mathcal{L}_1(s)\right]\frac{1}{6}\frac{\Omega_{eq}(\Delta l)^2}{\{\bar{C}_k(\bar{\lambda})\}^2}(l_c^*)^3 + \frac{s}{s-\Omega_D}\mathcal{L}_{3,D}(s)\ln\left(C^*_{k,DE}\right)$$

$$\left.+\frac{s}{s-\Omega_D}\left[K(s)\bar{C}_k(\bar{\lambda}_{cD}) - \mathcal{L}_{3,D}(s)\frac{\Omega_D}{s-\Omega_D}\right]\left[1 - C^*_{k,DE}e^{-s\bar{\tau}_{34}}\right]\right\}\Bigg]$$

$$\mathcal{L}_{10}(s) = g\rho_f\left[\mathcal{L}_1(s)\ln\left(C^*_{k,cD}\right)\right. \tag{5.176}$$

$$+\left[1 - s\mathcal{L}_1(s)\right]\left\{\frac{\Delta l_c}{\bar{C}_k(\bar{\lambda})} - \frac{\Delta l}{\bar{C}_k(\bar{\lambda})}\frac{1}{\sqrt{\frac{\Omega_{eq}\Delta l}{2\bar{C}_k(\bar{\lambda})}}}\tan^{-1}\left(l_c^*\sqrt{\frac{\Omega_{eq}\Delta l}{2\bar{C}_k(\bar{\lambda})}}\right)\right\}$$

$$+\frac{\mathcal{L}_{3,D}(s)}{s-\Omega_D}\left\{\frac{1}{C^*_{k,cD}} - \frac{1}{C^*_{k,cE}}\right\}$$

$$\left.+\frac{\bar{C}_k(\bar{\lambda})}{s}\left\{K(s) - \mathcal{L}_{3,D}(s)\frac{\Omega_D}{s-\Omega_D}\frac{1}{\bar{C}_k(\bar{\lambda}_{cD})}\right\}\left\{1 - e^{-s\bar{\tau}_{34}}\right\}\right]$$

$$\mathcal{L}_{11}(s) = \frac{\bar{C}_{m,c}\frac{f_f}{2D_h}}{\rho_f\bar{v}_{fi}^2}\left[\frac{2\Delta l_c}{\bar{v}_{fi}}\left\{1 - \frac{1}{2}\Omega_{eq}\mathcal{L}_1(s)l_c^*\right\}\right. \tag{5.177}$$

$$\left.+\left(1 + \frac{2\bar{V}_{gj}}{\bar{v}_{fi}}\right)I_1\right]$$

$$+\frac{\bar{C}_{m,D}\frac{f_f}{2D_h}}{\rho_f\bar{v}_{fi}^2}\left[\frac{2}{\bar{v}_{fi}}\mathcal{L}_{3,D}(s)\left(t - \bar{\lambda}_{cD}\right) + \left(1 + \frac{2\bar{V}_{gj}}{\bar{v}_{fi}}\right)I_2\right]$$

where

$$I_1 = \frac{\Omega_{eq}\Delta l}{2\bar{C}_k(\bar{\lambda})}\mathcal{L}_1(s)(l_c^*)^2 + \frac{1}{8}\frac{\Omega_{eq}^2(\Delta l)^2}{\{\bar{C}_k(\bar{\lambda})\}^2}\mathcal{L}_1(s)(l_c^*)^4 \tag{5.178}$$

(continued)

Reproduced with permission of the copyright owner. Further reproduction prohibited without permission.

$$+\left[1-s\mathcal{A}_1(s)\right]\frac{1}{6}\frac{\Omega_{eq}(\Delta t)^2}{\left\{\bar{C}_k(\bar{\lambda})\right\}^2}\left(k_c^*\right)^3+\left[1-s\mathcal{A}_1(s)\right]\frac{1}{20}\frac{\Omega_{eq}^2(\Delta t)^3}{\left\{\bar{C}_k(\bar{\lambda})\right\}^3}\left(k_c^*\right)^5$$

and

$$I_2 = C^*_{k,CD}\,\mathcal{A}_{3,D}(s)\,\frac{\Omega_D}{s-\Omega_D}\,\frac{(1-\bar{\lambda}_{cD})}{\bar{C}_k(\bar{\lambda}_{cD})} \tag{5.179}$$

$$+\,C^*_{k,CD}\left[K(s)-\mathcal{A}_{3,D}(s)\,\frac{\Omega_D}{s-\Omega_D}\,\frac{1}{\bar{C}_k(\bar{\lambda}_{cD})}\right]\frac{\bar{C}_k(\bar{\lambda}_{cD})}{(s-2\Omega_D)}\cdot$$

$$\left[1-\left(C^*_{k,DE}\right)^2 e^{-s\bar{\tau}_{34}}\right]$$

$$\mathcal{A}_{12}(s) = \left(C^*_{k,CE}\right)^2\left(1-2C^*_{k,CE}\right)\left[\frac{\bar{C}_k(\bar{\lambda})}{\bar{C}_k(\bar{\lambda}_{cD})}\right]\rho_g\bar{V}_{gj}^2 \tag{5.180}$$

$$\left\{\left(C^*_{k,DE}\right)^{-1} e^{-s\bar{\tau}_{34}}\left(K(s)-\mathcal{A}_{3,D}(s)\,\frac{\Omega_D}{s-\Omega_D}\,\frac{1}{\bar{C}_k(\bar{\lambda}_{cD})}\right)\right.$$

$$\left.+\,\mathcal{A}_{3,D}(s)\,\frac{\Omega_D}{s-\Omega_D}\,\frac{1}{\bar{C}_k(\bar{\lambda}_{cD})}\left(C^*_{k,DE}\right)^{-2}\right\}$$

where

$$C^*_{k,CE} = C^*_{k,CD}\;C^*_{k,DE} \tag{5.181}$$

$$\mathcal{A}_{13}(s) = k_e\,\rho_f\,\bar{v}_{fi}^2\left[\left(1+\frac{2\bar{V}_{gj}}{\bar{v}_{fi}}\right)C^*_{k,DE}\,e^{-s\bar{\tau}_{34}}\right. \tag{5.182}$$

$$\left(C^*_{k,CD}\,K(s)-\mathcal{A}_{3,D}(s)\,\frac{\Omega_D}{s-\Omega_D}\,\frac{1}{\bar{C}_k(\bar{\lambda})}\right)$$

$$\left.+\,\mathcal{A}_{3,D}(s)\,\frac{\Omega_D}{s-\Omega_D}\,\frac{1}{\bar{C}_k(\bar{\lambda})}\left(1+\frac{2\bar{V}_{gj}}{\bar{v}_{fi}}\right)+\frac{2}{\bar{v}_{fi}}\,\mathcal{A}_{3,D}(s)\right]$$

Reproduced with permission of the copyright owner. Further reproduction prohibited without permission.

V-7. Non-Dimensional Characteristic Equation

The characteristic equation (5.140) is non-dimensionalized using the length of the heated channel, ℓ , and the equilibrium reaction time, $1/\Omega_{eq}$, as the scaling parameters for length and time, respectively. Based on the above fundamental scales, the following dimensionless parameters are defined to non-dimensionalize the characteristic equation:

The geometrical parameters:

$$z^* = \frac{z}{\ell} \quad ; \quad D_h^* = \frac{D_h}{\ell} \tag{5.183}$$

The boiling length, $\bar{\lambda}^*$:

$$\bar{\lambda}^* = \frac{\bar{\lambda}}{\ell} = \frac{\rho_f A_c \bar{v}_{fi} (\Delta i_{sub} - \bar{\Delta i}_\lambda)}{\xi_h \dot{q}''_w \ell} \tag{5.184}$$

The equilibrium boiling length, $\bar{\lambda}^*_{eq}$:

$$\bar{\lambda}^*_{eq} = \frac{\bar{\lambda}_{eq}}{\ell} = \frac{\rho_f A_c \bar{v}_{fi} \Delta i_{sub}}{\dot{q}''_w \xi_h \ell} \tag{5.185}$$

The characteristic length, $\Delta\ell^*$:

$$\Delta\ell^* = \frac{\Delta\ell}{\ell} = \frac{\bar{\lambda}_{eq} - \bar{\lambda}}{\ell} = \frac{\rho_f A_c \bar{v}_{fi} \bar{\Delta i}_\lambda}{\dot{q}''_w \xi_h \ell} \tag{5.186}$$

The inlet velocity, $\bar{v}^*_{fi}$:

Reproduced with permission of the copyright owner. Further reproduction prohibited without permission.

$$\bar{v}_{fi}^{*} = \frac{\bar{v}_{fi}}{\Omega_{eq}\, \ell} \tag{5.187}$$

where Ω_{eq} is given by:

$$\Omega_{eq} = \Gamma_{g,eq}\, \frac{\Delta\rho}{\rho_g \rho_f} = \frac{\dot{q}''_w\, \bar{s}_h}{A_c\, \Delta i_{fg}}\, \frac{\Delta\rho}{\rho_g \rho_f} \tag{5.188}$$

The drift velocity, V_{gj}^{*} :

$$V_{gj}^{*} = \frac{\bar{V}_{gj}}{\bar{v}_{fi}} = \frac{\bar{V}_{gj}}{\Omega_{eq}\, \ell\, \bar{v}_{fi}^{*}} \tag{5.189}$$

The kinematic wave velocity, C_k^{*} :

$$C_k^{*}(\bar{z}) = \frac{\bar{C}_k(\bar{z})}{\Omega_{eq}\, \ell} \tag{5.190}$$

Therefore,

$$C_k^{*}(\bar{\lambda}) = \bar{v}_{fi}^{*}\,(1 + V_{gj}^{*}) \tag{5.191}$$

$$C_{k,CD}^{*} = 1 + A^{*}\,(\ell_c^{*})^2 \tag{5.192}$$

and

$$C_{k,DE}^{*} = 1 + \frac{\ell_c^{*}\,(1 - \bar{\lambda}_{CD}^{*})}{C_{k,CD}^{*}\, C_k^{*}(\bar{\lambda})} \tag{5.193}$$

where

$$A^{*} = \frac{\Delta\ell^{*}}{2\, C_k^{*}(\bar{\lambda})} \tag{5.194}$$

and

$$\bar{\lambda}_{CD}^{*} = \bar{\lambda}^{*} + \ell_c^{*}\, \Delta\ell^{*} \tag{5.195}$$

Reproduced with permission of the copyright owner. Further reproduction prohibited without permission.

The residence time in the single-phase region:

$$\tau_{12}^{*} = \bar{\tau}_{12}\,\Omega_{eq} = \frac{\bar{\lambda}^{*}}{\bar{v}_{fi}^{*}} \tag{5.196}$$

The residence time in region D:

$$\tau_{34}^{*} = \bar{\tau}_{34}\,\Omega_{eq} = \frac{1}{\ell_c^{*}} \ln\left(C_{k,DE}^{*}\right) \tag{5.197}$$

The independent variable, s^{*}:

$$s^{*} = \frac{s}{\Omega_{eq}} = \frac{a}{\Omega_{eq}} + j\,\frac{\omega}{\Omega_{eq}} = a^{*} + j\,\omega^{*} \tag{5.198}$$

The density ratio:

$$\rho_g^{*} = \frac{\rho_g}{\rho_f} \tag{5.199}$$

The acceleration due to gravity:

$$g^{*} = \frac{g}{\Omega_{eq}^{2}\,\ell} \tag{5.200}$$

The pressure drop:

$$\Delta P^{*} = \frac{\Delta P}{\Omega_{eq}^{2}\,\ell^{2}\,\rho_f} \tag{5.201}$$

The transfer function for the boiling boundary:

Reproduced with permission of the copyright owner. Further reproduction prohibited without permission.

$$\mathcal{L}_1^*(s) = \Omega_{eq}\,\mathcal{L}_1(s) = \Omega_{eq}\bar{v}_{fi}\,\mathcal{L}_o + \frac{\Omega_{eq}}{s}\left[1-e^{-s\bar{\tau}_{12}}\right] \quad (5.202)$$

$$= \mathcal{L}_o^* + \frac{1}{s^*}\left(1-e^{-s^*\tau_{12}^*}\right)$$

where $\mathcal{L}_o^*$ represents the fluctuation of the local subcooling at the boiling boundary due to an inlet flow fluctuation.

Using the above set of dimensionless parameters, one can write the non-dimensionalized characteristic equation as:

$$\frac{Q(s)}{(\rho_f \Omega_{eq} \ell)\bar{v}_{fi}^*} \equiv Q^*(s^*) = \frac{1}{s^{*2}\cdot(s^*-\mathcal{L}_c^*)^2(s^*-2\mathcal{L}_c^*)} \cdot \quad (5.203)$$

$$\left\{\left(D_1 s^{*7} + D_2 s^{*6} + D_3 s^{*5} + D_4 s^{*4} + D_5 s^{*3} + D_6 s^{*2} + D_7 s^* + D_8\right)\right.$$

$$+ \left(D_9 s^{*6} + D_{10} s^{*5} + D_{11} s^{*4} + D_{12} s^{*3} + D_{13} s^{*2} + D_{14} s^* + D_{15}\right) e^{-s^*\tau_{12}^*}$$

$$+ \left(D_{16} s^{*6} + D_{17} s^{*5} + D_{18} s^{*4} + D_{19} s^{*3} + D_{20} s^{*2} + D_{21} s^* + D_{22}\right) e^{-s^*\tau_{34}^*}$$

$$\left. + \left(D_{23} s^{*5} + D_{24} s^{*4} + D_{25} s^{*3} + D_{26} s^{*2} + D_{27} s^* + D_{28}\right) e^{-s^*(\tau_{12}^*+\tau_{34}^*)}\right\}$$

Notice that the characteristic equation is expressed in the form of a seventh order polynomial with three time delays. The coefficients D_i are composed of another set of coefficients C_i. Both sets of coefficients as well as several identities are presented in Appendix A. It should be noted, however, that if the transfer function $\mathcal{L}_o^*$ is zero, the character-

Reproduced with permission of the copyright owner. Further reproduction prohibited without permission.

istic equation takes the form of a sixth order polynomial with three time delays.

V-8. Determination of Stability Boundary

Following the analysis of Ishii [2], the shifted characteristic equation for the present case is:

$$Z^*(s^*) \equiv (s^* - L_c^*)^2 (s^* - 2L_c^*) Q^*(s^*) = 0 \tag{5.204}$$

The stability boundary is determined by using the D-partition method, a discussion of which can be found in references [2, 45, and 47]. The shifted characteristic function Z^* can be expressed as:

$$Z^*(s^*, \alpha_1, \alpha_2, \cdots\cdots, \alpha_m) = 0 \tag{5.205}$$

where α_1 to α_m represents the parameters which can be changed independently. For harmonic oscillations,

$$s^* = j\omega^* \tag{5.206}$$

Substituting (5.206) into (5.205), and resolving into the real and imaginary parts, one obtains:

$$Z^*_{Re}(\omega^*, \alpha_1, \alpha_2, \cdots\cdots, \alpha_m) = 0 \tag{5.207}$$

and

$$Z^*_{Im}(\omega^*, \alpha_1, \alpha_2, \cdots\cdots, \alpha_m) = 0 \tag{5.208}$$

Reproduced with permission of the copyright owner. Further reproduction prohibited without permission.

Equations (5.207) and (5.208) give the harmonic frequency surfaces in m-dimensional space, i.e., α_1, α_2, ..., α_m as co-ordinates, with ω^* as an auxiliary parameter. Since the complex roots are always conjugate for the functions with real coefficients, the domain of interest for ω^* becomes:

$$0 < \omega^* < \infty \tag{5.209}$$

Due to the practical difficulties of working in an m-dimensional space, the two-dimensional stability plane introduced by Ishii [2,19] and shown in Figure 19 shall be used here. The subcooling number, $\frac{\Delta\rho}{\rho_g}\frac{\Delta i_{sub}}{\Delta i_{fg}}$, scales the inlet subcooling and it is the dimensionless residence time in the single-phase region under the equilibrium assumption. The equilibrium phase change number, $\frac{\Omega_{eq}\, l}{\bar{v}_{fi}}$, scales the change of phase due to heat addition and this corresponds to Damkoeler's group I in chemical kinetics. One of the advantages of using these groups as the co-ordinates is that the stability boundary predicted by the present analysis can be compared easily with the results predicted by the equilibrium theory as well as with the experimental data. The other parameters, i.e., k_i, k_e, Re_{fs}, etc., are kept constant for one stability map. Therefore, equations (5.207) and (5.208) reduce to:

$$Z^*_{Re}\left(\omega^*,\ N_{sub},\ N_{pch,eq}\right) = 0 \tag{5.210}$$

and

$$Z^*_{Im}\left(\omega^*,\ N_{sub},\ N_{pch,eq}\right) = 0 \tag{5.211}$$

Reproduced with permission of the copyright owner. Further reproduction prohibited without permission.

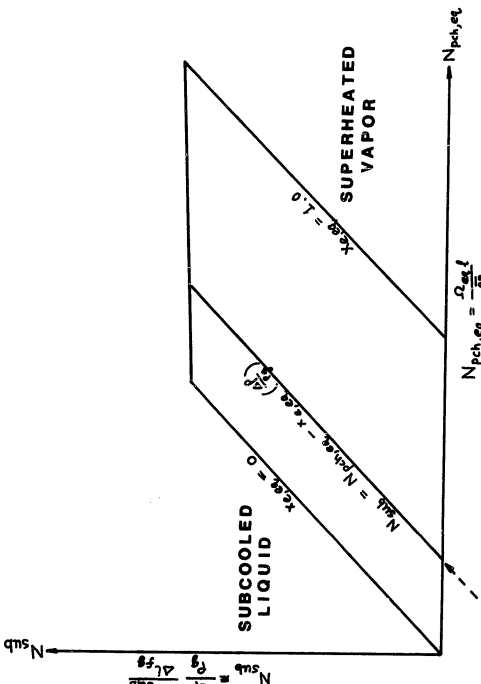

Figure 19. The Stability Plane

Reproduced with permission of the copyright owner. Further reproduction prohibited without permission.

Equations (5.210) and (5.211) give the neutral stability boundaries which divide the stability plane in several regions. Stability of each of these regions is then determined by using the Mikhailov Criterion or the Encirclement Theorem [2,45,47]. According to this theorem, the number of roots with positive real parts is given by:

$$k = \frac{1}{2}\left\{ n - \frac{2}{\pi}\left[\Delta Z^*\right]_0^{\infty} \right\} \tag{5.212}$$

where n is the highest order of the polynomial in Z^*, and $\left[\Delta Z^*\right]_0^{\infty}$ is the change of argument of $Z^*(j\omega^*)$ in the counterclockwise direction when ω^* travels from zero to ∞.

It can be seen from (5.204) that three positive roots have already been introduced artificially in the shifted characteristic function Z^*. Therefore, for the stability of a region, the value of k should not be more than three.

In view of (5.204), the condition for excursive stability, i.e., (5.142), now becomes:

$$\lim_{s^* \to 0} Z^*(s^*) < 0 \tag{5.213}$$

Putting s^* equal to $j\omega^*$ in equation (5.203), and resolving into the real and imaginary parts, one can write the parametric equations (5.210) and (5.211) for the neutral stability boundaries as:

Reproduced with permission of the copyright owner. Further reproduction prohibited without permission.

$$Z^*_{Re} = -\frac{1}{\omega^{*2}}\left\{\left(-D_2\omega^{*6} + D_4\omega^{*4} - D_6\omega^{*2} + D_8\right)\right. \tag{5.214}$$

$$+ \left(-D_9\omega^{*6} + D_{11}\omega^{*4} - D_{13}\omega^{*2} + D_{15}\right)\cos\left(\omega^*\tau^*_{12}\right)$$

$$+ \left(D_{10}\omega^{*5} - D_{12}\omega^{*3} + D_{14}\omega^*\right)\sin\left(\omega^*\tau^*_{12}\right)$$

$$+ \left(-D_{16}\omega^{*6} + D_{18}\omega^{*4} - D_{20}\omega^{*2} + D_{22}\right)\cos\left(\omega^*\tau^*_{34}\right)$$

$$+ \left(D_{17}\omega^{*5} - D_{19}\omega^{*3} + D_{21}\omega^*\right)\sin\left(\omega^*\tau^*_{34}\right)$$

$$+ \left(D_{24}\omega^{*4} - D_{26}\omega^{*2} + D_{28}\right)\cos\left[\omega^*\left(\tau^*_{12} + \tau^*_{34}\right)\right]$$

$$\left. + \left(D_{23}\omega^{*5} - D_{25}\omega^{*3} + D_{27}\omega^*\right)\sin\left[\omega^*\left(\tau^*_{12} + \tau^*_{34}\right)\right]\right\} = 0$$

and $$Z^*_{Im} = -\frac{1}{\omega^{*2}}\left\{\left(-D_1\omega^{*7} + D_3\omega^{*5} - D_5\omega^{*3} + D_7\omega^*\right)\right. \tag{5.215}$$

$$+ \left(D_{10}\omega^{*5} - D_{12}\omega^{*3} + D_{14}\omega^*\right)\cos\left(\omega^*\tau^*_{12}\right)$$

$$+ \left(D_9\omega^{*6} - D_{11}\omega^{*4} + D_{13}\omega^{*2} - D_{15}\right)\sin\left(\omega^*\tau^*_{12}\right)$$

$$+ \left(D_{17}\omega^{*5} - D_{19}\omega^{*3} + D_{21}\omega^*\right)\cos\left(\omega^*\tau^*_{34}\right)$$

$$\left. + \left(D_{16}\omega^{*6} - D_{18}\omega^{*4} + D_{20}\omega^{*2} - D_{22}\right)\sin\left(\omega^*\tau^*_{34}\right)\right.$$

(continued)

Reproduced with permission of the copyright owner. Further reproduction prohibited without permission.

$$+\left(D_{23}\omega^{*5}-D_{25}\omega^{*3}+D_{27}\omega^{*}\right)\cos\left[\omega^{*}\left(\tau_{12}^{*}+\tau_{34}^{*}\right)\right]$$

$$+\left(-D_{24}\omega^{*4}+D_{26}\omega^{*2}-D_{28}\right)\sin\left[\omega^{*}\left(\tau_{12}^{*}+\tau_{34}^{*}\right)\right]\Big\}=0$$

By taking the limit $\omega^{*}\to 0$ in equations (5.214) and (5.215) and using the identities given in Appendix A, one obtains:

$$Z_{Re}^{*}(0)=\left(D_{6}+D_{13}+D_{20}+D_{26}\right)-\left(D_{14}+D_{27}\right)\tau_{12}^{*}-\left(D_{21}+D_{27}\right)\tau_{34}^{*} \qquad (5.216)$$

and

$$Z_{Im}^{*}(0)=0 \qquad (5.217)$$

Therefore, the condition for excursive stability reduces to:

$$Z_{Re}^{*}(0)<0 \qquad (5.218)$$

For numerical evaluation of the system stability boundary, two computer programs, namely, INSTAB and TEST, have been written. The program INSTAB generates the functional relationship between the subcooling number and the equilibrium phase change number which divides the stability plane in several regions. The program TEST is then used to determine the stability of each of these regions. The structure of these programs is given below:

Reproduced with permission of the copyright owner. Further reproduction prohibited without permission.

Program INSTAB

In this program the stability plane is divided by the constant subcooling and constant equilibrium quality lines, each of which is equally intervaled, so that the plane is covered with the meshes. At each intersection of the above lines, the coefficients C_i and D_i can be calculated. Then the crossover frequencies, ω_c^* (where Z_{Im}^* changes sign), are found by increasing ω^* stepwise and using the interpolation technique. These ω_c^* are substituted into the expression (5.212) to calculate Z_{Re}^*. The point where both $Z_{Re}^*(\omega_c^*)$ and $Z_{Im}^*(\omega_c^*)$ are zero represents a point on the neutral stability boundary. By changing the point systematically over the stability plane, the neutral stability boundaries can be mapped. The flow diagram and the listing of the program are provided in Appendix B.

Program TEST

This program is very straightforward. A point with known subcooling number and equilibrium phase change number is chosen in a region whose stability is to be determined. The values of $Z_{Re}^*(\omega^*)$ and $Z_{Im}^*(\omega^*)$ are then calculated from ω^* equal to zero to a fairly high value. The program is used to calculate $[\Delta Z^*]_0^\infty$ for equation (5.212), and to check the condition (5.218) for excursive stability.

Reproduced with permission of the copyright owner. Further reproduction prohibited without permission.

CHAPTER VI

RESULTS AND DISCUSSIONS

VI-1. Results of the Theoretical Analysis

The analysis presented in the previous chapter is used to predict theoretically the system stability boundary. The required input data are the system pressure, liquid, and vapor properties corresponding to the system saturation temperature, flow Reynolds number, and the channel geometry including the values for the inlet and exit orifice coefficients. Following the analysis of Ishii [2], the values for $\overline{C}_{m,c}$ as well as $\overline{C}_{m,D}$ in equations (5.169) and (5.170) are taken to be equal to two.† The expression (4.52) is used for the vapor drift velocity, $\overline{V}_{gj}$.

As pointed out earlier, for Pe > 70,000 the local subcooling at the point of net vapor generation is inversely proportional to the inlet velocity. This was discovered from the steady state void fraction data which were used in the St-Pe plot shown in Figure 12. It is the characteristic Strouhal number which dictates whether the same conclusion can be extended to the transient problem. It is, therefore, decided that two different cases shall be examined for Pe > 70,000:

Case I. Assume that the local subcooling at the boiling boundary, in the transient analysis, does not change with inlet velocity, i.e., $\Delta\mathcal{L}_o^* = 0$.

†The single-phase friction factor is calculated from:

$$f_f = \frac{0.184}{Re_{fs}^{0.2}} \tag{6.1}$$

Reproduced with permission of the copyright owner. Further reproduction prohibited without permission.

Case II. Assume that the local subcooling at the boiling boundary changes according to equation (4.19), i.e.,

$$\Lambda_o^* = 154 \frac{A_c}{\xi_h} \frac{Q_{eq}}{v_{fi}} \quad .$$

In Figure 20, the stability map for case I, i.e., $\Lambda_o^* = 0$, is shown for the input data corresponding to the set number I. The neutral stability boundaries are obtained from the program INSTAB and the number of roots having positive real part, k, in various regions is obtained from program TEST and equation (5.212). As found in [2], in the present analysis also, the first neutral stability boundary is found to be the system stability boundary. The value of k in equation (5.212) is found to be equal to three on the left hand side of the first neutral stability boundary. This value of k increases by two every time one crosses a neutral stability boundary and goes to the right hand side. The condition for excursive stability, i.e., $Z_{Re}^*(0) < 0$, has also been checked in each region. For clarity of presentation, only the first neutral stability boundary, i.e., the system stability boundary, shall be shown hereafter.

In Figure 21, the stability boundaries for both cases I and II, corresponding to the set number I, have been shown. It can be seen that case II predicts a more unstable system than case I. This is due to the fact that, in case II, the non-zero positive value of Λ_o^* adds to the fluctuation of the boiling boundary which has a destabilizing effect on the system. Another interesting feature observed in case II is that, at a higher subcooling number, the second neutral stability boundary overtakes the first neutral stability boundary and becomes the system stability boundary.

Reproduced with permission of the copyright owner. Further reproduction prohibited without permission.

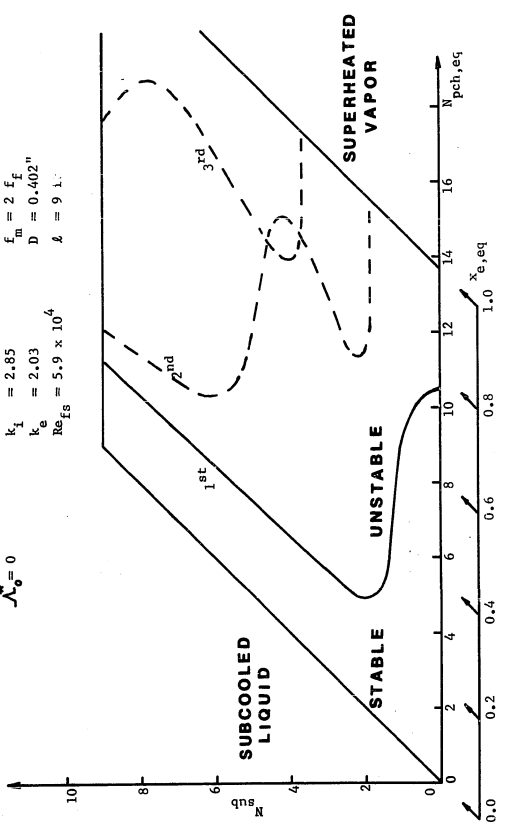

Figure 20. The Stability Map for Case I

Reproduced with permission of the copyright owner. Further reproduction prohibited without permission.

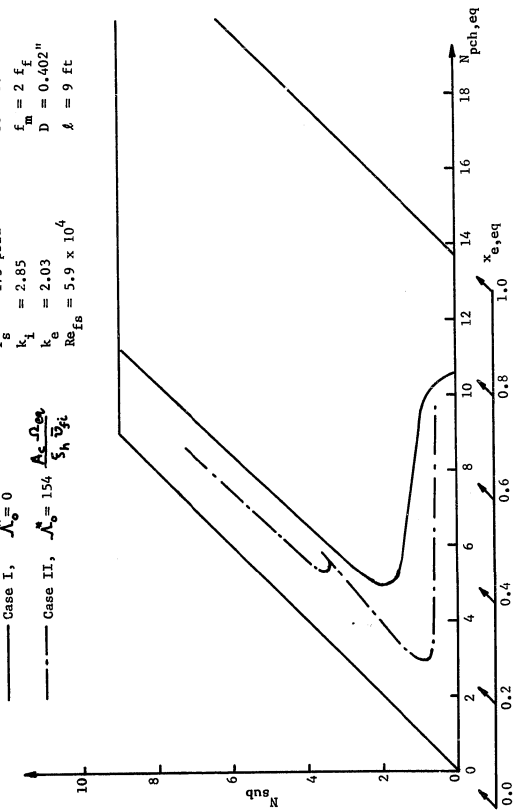

Figure 21. The System Stability Boundaries for Case I and Case II

Reproduced with permission of the copyright owner. Further reproduction prohibited without permission.

In Figure 22, the results of the non-equilibrium theory (both cases I and II) are compared with the latest equilibrium theory of Ishii [2,19]. The simplified criterion of Ishii [2], which is valid only for a high subcooling number, is also shown. For the case of zero inlet subcooling, where the system is under thermal equilibrium, the prediction of the non-equilibrium theory coincides with that of the equilibrium theory as expected. As the subcooling number increases, the non-equilibrium model starts to predict a more stable system because for $\Delta i_{sub} < \Delta i_{\lambda}$, vapor generation still starts at the inlet of the heated channel which implies that there is no time delay in the single-phase region (in fact, there is no single-phase region at all). As the subcooling number increases beyond a certain value, the non-equilibrium model predicts a more unstable system because the region occupied by the two-phase mixture is longer than that under the equilibrium model. It can be noticed, however, that, like the equilibrium model, the non-equilibrium stability boundary is also almost parallel to the constant equilibrium exit quality line at a high subcooling number.

VI-2. Comparison with Experimental Data

In Figure 23, the experimental data on the onset of flow oscillation corresponding to set number I are compared with the present non-equilibrium theories (both case I and case II) as well as with the equilibrium theory of Ishii [2,19]. In Figure 24, the non-dimensional frequency of oscillation obtained from experimental investigation is compared with the predictions of the non-equilibrium as well as the equilibrium theories. The values of N_{sub}, $N_{pch,eq}$, and ω^* for sets I through VII are

Reproduced with permission of the copyright owner. Further reproduction prohibited without permission.

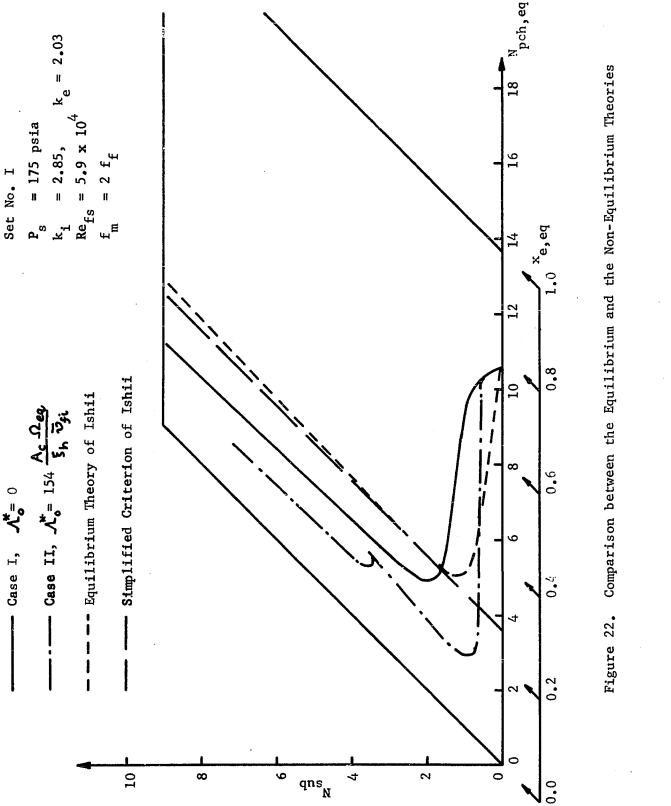

Figure 22. Comparison between the Equilibrium and the Non-Equilibrium Theories

Reproduced with permission of the copyright owner. Further reproduction prohibited without permission.

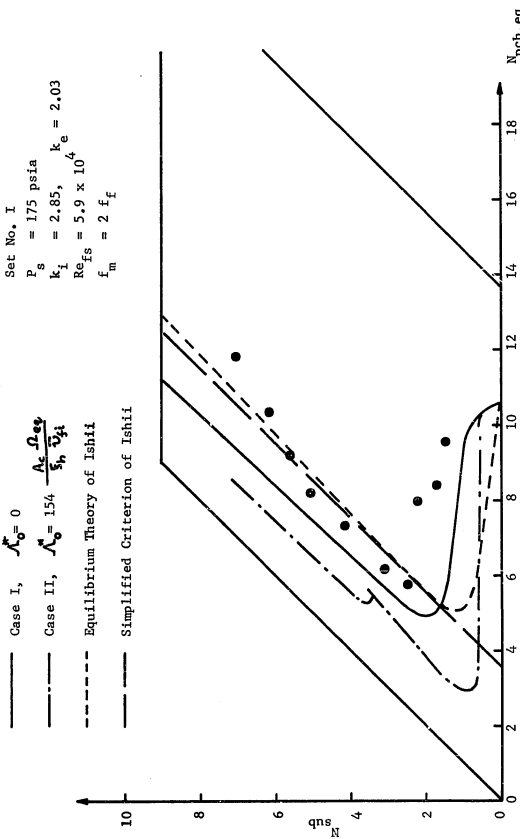

Figure 23. Comparison of Experimental Data on the Onset of Flow Oscillation with Various Theoretical Predictions

Reproduced with permission of the copyright owner. Further reproduction prohibited without permission.

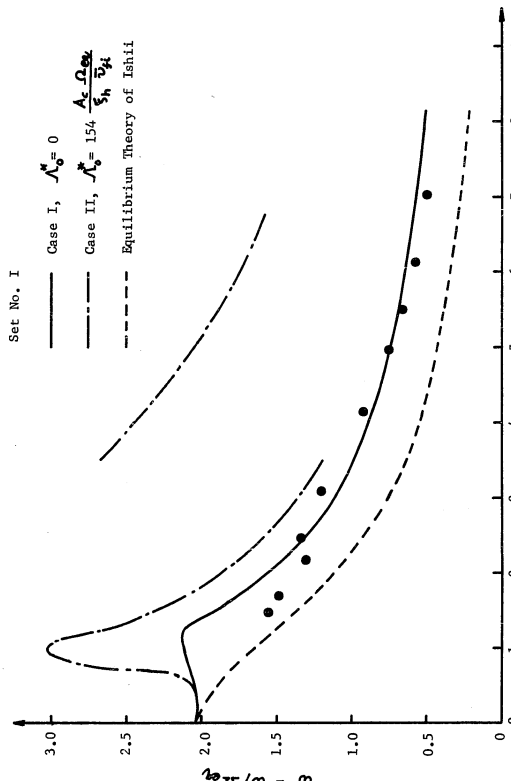

Figure 24. Comparison of Experimental Data on the Frequency of Oscillation with Various Theoretical Predictions

Reproduced with permission of the copyright owner. Further reproduction prohibited without permission.

tabulated in Appendix C. It can be seen from Figure 23 that, on the whole, the non-equilibrium theory with $\mathcal{N}_o^* = 0$, i.e., case I, predicts results which are conservative but in closer agreement with the system stability boundary formed by the experimental data. The equilibrium theory of Ishii is more conservative at low subcooling numbers and is unsafe at moderate subcooling numbers. On the other hand, the non-equilibrium theory with $\mathcal{N}_o^* = 154 \frac{A_c}{\xi_h} \frac{\Omega_{eq}}{\bar{v}_{fi}}$, i.e., case II, is very conservative at every subcooling number. From Figure 24 also, it can be seen that the non-equilibrium theory with $\mathcal{N}_o^* = 0$ predicts the frequency of oscillation best.

To check the above findings further, another set of experimental data (set number IV) is compared with the non-equilibrium as well as the equilibrium theories in Figures 25 and 26. From these figures, it can be seen that the non-equilibrium theory with $\mathcal{N}_o^* = 0$ is again the best choice for predicting the system stability boundary. This implies that it is more appropriate to assume that, in the transient case, the local subcooling at the boiling boundary does not change due to a small perturbation in inlet velocity. It should also be kept in mind that, for density wave oscillations, where the frequency of oscillation, f, is on the order of $\bar{v}_{fi}/\ell$, the characteristic Strouhal number, $(2\pi f \Delta z)/\bar{v}_{fi}$, is not negligible compared to unity. Therefore, one cannot a priori extend the conclusions derived from steady state data to the non-steady situation.

The effect of system pressure is shown in Figure 27. Although the experimental data show slight variation in the stability boundary, the theory does not predict any change in the chosen stability plane. It

Reproduced with permission of the copyright owner. Further reproduction prohibited without permission.

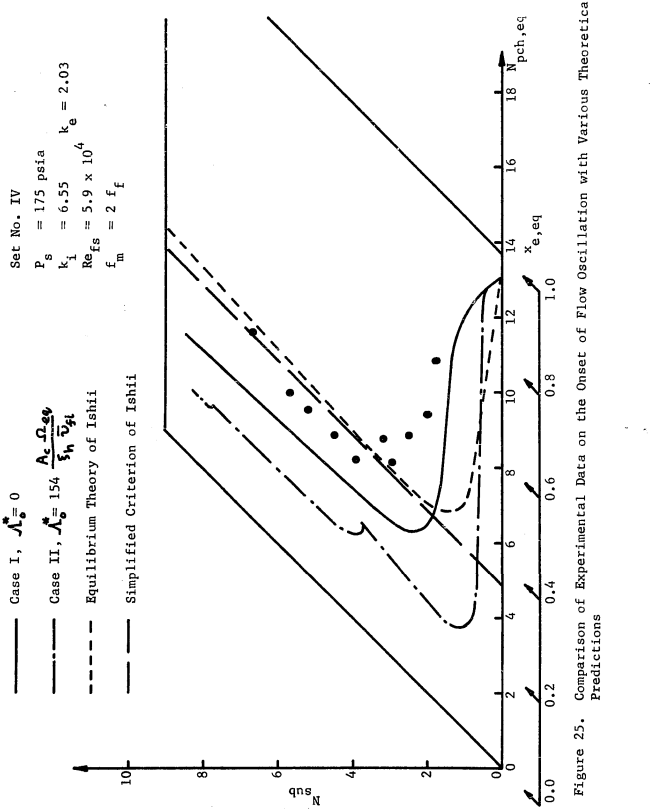

Figure 25. Comparison of Experimental Data on the Onset of Flow Oscillation with Various Theoretical Predictions

Reproduced with permission of the copyright owner. Further reproduction prohibited without permission.

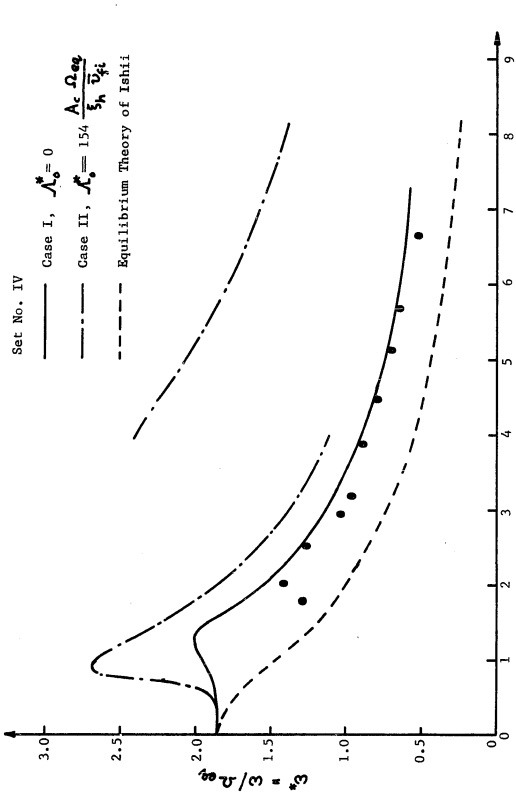

Figure 26. Comparison of Experimental Data on the Frequency of Oscillation with Various Theoretical Predictions

Reproduced with permission of the copyright owner. Further reproduction prohibited without permission.

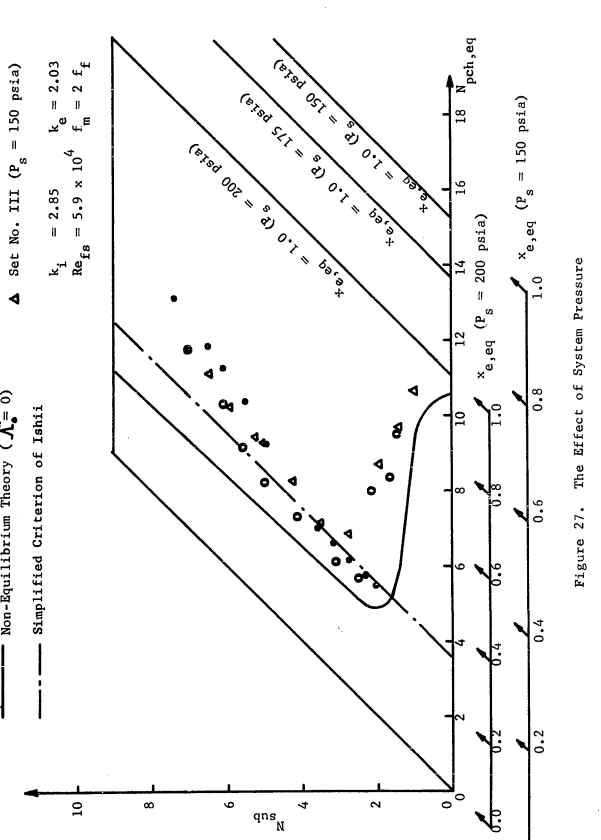

Figure 27. The Effect of System Pressure

Reproduced with permission of the copyright owner. Further reproduction prohibited without permission.

should be noticed, however, that the higher the pressure the higher is the value of exit quality at the onset of oscillation.

The effects of the inlet and exit restrictions are shown in Figures 28 and 29. Like the equilibrium model, the non-equilibrium theory as well as the experimental data indicate a more stable system when the inlet throttling is increased, as shown in Figure 28. On the other hand, the models predict a more unstable system as the exit throttling is increased (see Figure 29). The experimental data corresponding to set number VII, however, indicate a more unstable system only at lower subcooling number and almost no change at higher subcooling number.

The effect of flow Reynolds number is shown in Figure 30. Although there is very little difference in the theoretical prediction, experimental data show significant change with respect to the Reynolds number.

One common feature can be observed from the experimental data presented in this section. As the subcooling number is increased beyond a critical value, the stability boundary formed by the experimental data always bends towards the right hand side from a constant equilibrium exit quality line. This trend has also been observed in other experimental investigations (for example, see Solberg's data as presented in Figure 25 of Reference 2). The theoretical prediction, however, remains almost parallel to a constant equilibrium exit quality line, i.e., the onset of flow oscillation according to the theory takes place at a characteristic equilibrium exit quality.

Two possible aspects can be examined for this discrepancy. First, the two-phase friction factor is actually a function of vapor void fraction which increases along the length of the channel. In the theoretical

Reproduced with permission of the copyright owner. Further reproduction prohibited without permission.

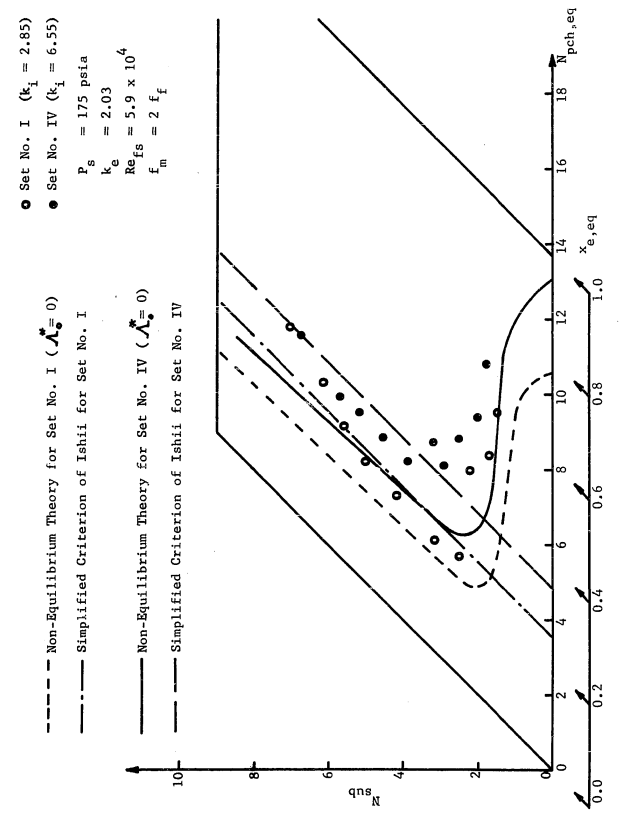

Figure 28. The Effect of Inlet Restriction

Reproduced with permission of the copyright owner. Further reproduction prohibited without permission.

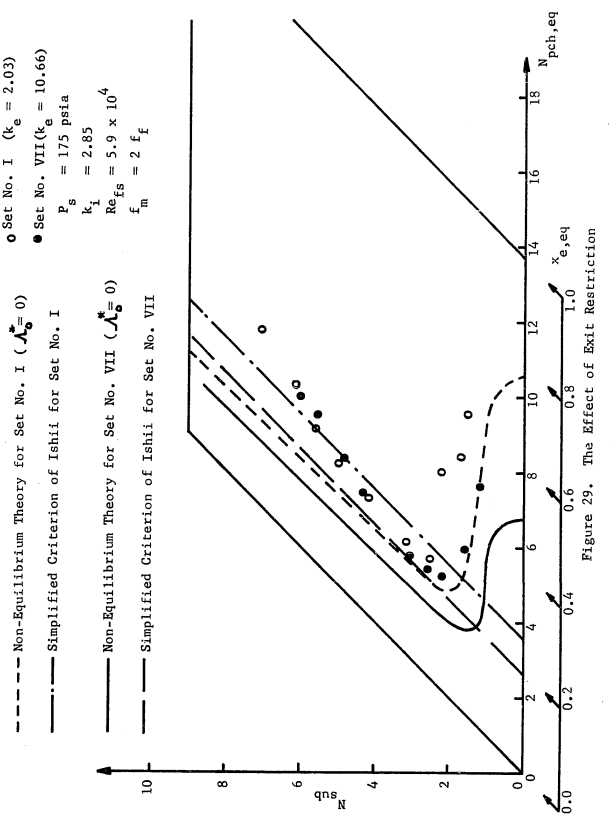

Figure 29. The Effect of Exit Restriction

Reproduced with permission of the copyright owner. Further reproduction prohibited without permission.

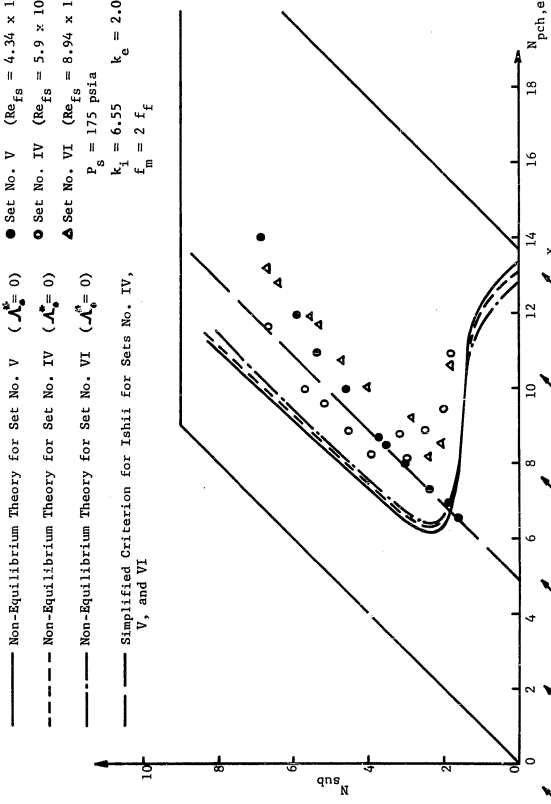

Figure 30. The Effect of Reynolds Number

Reproduced with permission of the copyright owner. Further reproduction prohibited without permission.

analysis, the friction factor is taken to be a constant. However, according to the analysis of Ishii [2], the friction factor has very little influence on the system stability boundary at high subcooling number. Secondly, from the flow regime diagram on page 15 of Reference 5, it is found that, at the onset of flow oscillation, the flow pattern at the exit is annular for all cases reported here. In the analysis, however, a weighted mean vapor drift velocity corresponding to the bubbly churn flow has been used. Due to higher relative velocity between the phases, the vapor drift velocity in the annular flow regime can be much higher than the value taken in the present analysis. Ishii [2] showed that the vapor drift velocity has a stabilizing effect on the system. Therefore, it is apparent that the higher values of the vapor drift velocity in the actual system cause the data to bend towards the right hand side from a constant equilibrium exit quality line.

Reproduced with permission of the copyright owner. Further reproduction prohibited without permission.

CHAPTER VII

SIMPLIFIED STABILITY CRITERION

In addition to the rigorous computer solution presented in the previous chapter, it is desirable to have a simplified stability criterion that can be used for preliminary estimation of the stability boundary. The simplified criterion of Ishii [2] used in the previous chapter for comparison with experimental data is expressed by:

$$x_{e,eq}\frac{\Delta\rho}{\rho_g} = N_{pch,eq} - N_{sub} = \frac{2\left[k_i + \frac{C_m f_f}{2D_h^*} + k_e\right]}{1 + \frac{1}{2}\left[\frac{C_m f_f}{2D_h^*} + 2k_e\right]} \tag{7.1}$$

The above criterion predicts that the onset of flow oscillation occurs at a constant equilibrium exit quality condition. However, this criterion was derived for high subcooling number ($N_{sub} > \pi$) and, therefore, cannot be expected to show good agreement with the experimental data at low subcooling number. This is why the above criterion predicts a very conservative estimate of the stability boundary at low subcooling number, as shown in the previous chapter. Therefore, an additional simple criterion, particularly for the low subcooling number, should be of great help for preliminary estimation of the system stability boundary. Such a criterion shall be developed in what follows.

As mentioned in section VI-1, there is a basic difference between

Reproduced with permission of the copyright owner. Further reproduction prohibited without permission.

the equilibrium and the non-equilibrium models at low subcooling number. In the equilibrium model there is a single-phase liquid region, i.e., a time lag τ_{12} , as soon as the subcooling number becomes greater than zero; whereas in the non-equilibrium model there is no single-phase liquid region, i.e., no time lag τ_{12} , until the subcooling number is greater than $\frac{\Delta\rho}{\rho_g}\frac{\Delta i_\lambda}{\Delta i_{fg}}$. This is the reason why the non-equilibrium model as well as the experimental data show a more stable system at low subcooling number compared to the equilibrium model.

From the criteria for the point of net vapor generation, i.e., equations (4.18) and (4.19), the corresponding critical subcooling number, $(N_{sub})_{cr}$, below which vapor generation starts from the inlet of the heated channel, i.e., $\bar{\lambda}$ is equal to zero, can be given by:

$$(N_{sub})_{cr} = 0.0022\ Pe\ \left(\frac{A_c}{\xi_h \ell}\right) N_{pch,eq} \qquad (7.2)$$

for $Pe < 70{,}000$

and

$$(N_{sub})_{cr} = 154\ \left(\frac{A_c}{\xi_h \ell}\right) N_{pch,eq} \qquad (7.3)$$

for $Pe > 70{,}000$

The above criterion for the critical subcooling number is shown in Figure 31 along with the experimental data for set number I, simplified criterion of Ishii and the prediction of the non-equilibrium model. It can be seen that, once the equilibrium phase change number corresponding to the zero subcooling number, i.e., $(N_{pch,eq})_o$, is determined, say

Reproduced with permission of the copyright owner. Further reproduction prohibited without permission.

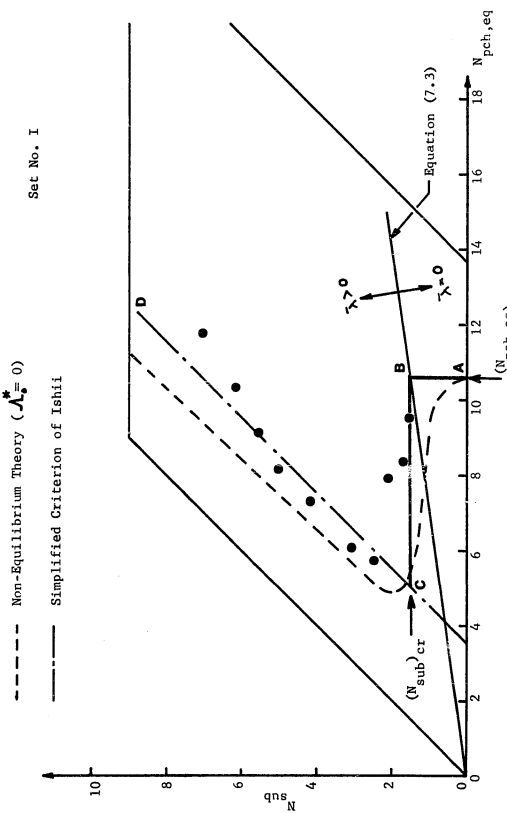

Figure 31. Critical Subcooling Number and Construction of the Simplified Stability Criterion

Reproduced with permission of the copyright owner. Further reproduction prohibited without permission.

by running the computer program INSTAB for N_{sub} equal to zero, the following algorithm can be used to generate a simplified stability boundary:

1. Determine $(N_{sub})_{cr}$ corresponding to $(N_{pch,eq})_o$ using equation (7.2) or (7.3).
2. $N_{pch,eq} = (N_{pch,eq})_o$ for $N_{sub} < (N_{sub})_{cr}$ (7.4)
3. $$N_{pch,eq} = N_{sub} + \frac{2\left[k_i + \frac{C_m f_z}{2D_h^*} + k_e\right]}{1 + \frac{1}{2}\left[\frac{C_m f_z}{2D_h^*} + 2k_e\right]} \quad \text{for } N_{sub} > (N_{sub})_{cr} \tag{7.1}$$

The construction of the simplified stability boundary is shown in Figures 31 and 32. It consists of three parts:

1. A constant equilibrium phase change number $(N_{pch,eq})_o$, for $N_{sub} < (N_{sub})_{cr}$, i.e., the part AB,
2. A constant subcooling number, $(N_{sub})_{cr}$, i.e., the part BC, and
3. A constant equilibrium exit quality line, equation (7.1) for $N_{sub} > (N_{sub})_{cr}$, i.e., the part CD.

An alternative, at the same more conservative, stability boundary for $N_{sub} < (N_{sub})_{cr}$ could be the straight line AC, as shown in Figure 32.

Reproduced with permission of the copyright owner. Further reproduction prohibited without permission.

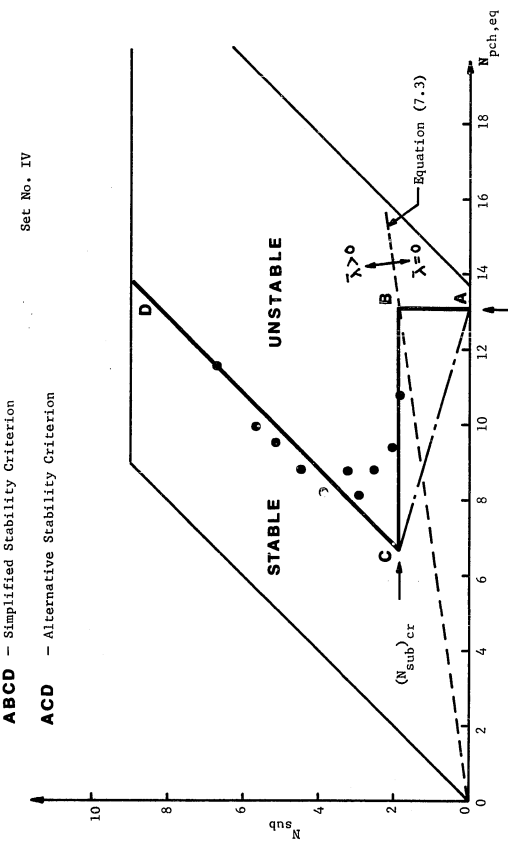

Figure 32. Construction of the Simplified Stability Criterion

Reproduced with permission of the copyright owner. Further reproduction prohibited without permission.

CHAPTER VIII

CONCLUSIONS

The following conclusions can be drawn in the context of the present investigation:

1. The point of net vapor generation in a boiling channel with inlet subcooling depends on local conditions--thermal and hydrodynamic. For low mass-flow rate (Pe < 70,000) the point of net vapor generation is governed by thermal conditions, whereas for high mass-flow rate (Pe > 70,000) the point is governed by hydrodynamic conditions. A new correlation has been found which can be used to determine this point accurately for all mass-flow rates.

2. A constitutive equation for the mass rate of vapor formation per unit volume has been derived for the thermodynamic (thermal) non-equilibrium region, i.e., the subcooled boiling region. This equation, together with the new correlation for the point of net vapor generation, can be used to predict the true vapor quality and the true vapor void fraction in a boiling channel.

3. The effect of thermal non-equilibrium has been incorporated in the transient analysis of a heated boiling channel with inlet subcooling. Using the small perturbation technique, a system characteristic equation in the form of a seventh order polynomial with three time delays has been derived.

4. The system stability boundary including the effect of thermal

Reproduced with permission of the copyright owner. Further reproduction prohibited without permission.

non-equilibrium predicts a more stable system at low subcooling number, and a more unstable system at high subcooling number when compared with the latest equilibrium theory of Ishii.

5. Experimental data on the onset of flow oscillation have been obtained from the boiling loop described in Chapter II. Comparison of these data with various theories indicates that the non-equilibrium theory (assuming no change in local subcooling at the boiling boundary) predicts the system stability boundary better than the equilibrium theory.

6. A simplified stability criterion for low subcooling number has been developed which can be used for preliminary estimation of the system stability boundary along with the simplified criterion of Ishii for high subcooling number.

Reproduced with permission of the copyright owner. Further reproduction prohibited without permission.

APPENDICES

Reproduced with permission of the copyright owner. Further reproduction prohibited without permission.

APPENDIX A

COEFFICIENTS OF THE NON-DIMENSIONAL CHARACTERISTIC EQUATION (5.203)

$$D_1 = C_1$$

$$D_2 = -4\ell_c^* C_1 + C_2 + C_6$$

$$D_3 = 5\ell_c^{*2} C_1 - 4\ell_c^* C_2 + C_3 - 3\ell_c^* C_6 + C_7 + C_8$$

$$D_4 = -2\ell_c^{*3} C_1 + 5\ell_c^{*2} C_2 - 4\ell_c^* C_3 + C_4 + 2\ell_c^{*2} C_6$$

$$- 3\ell_c^* C_7 - 2\ell_c^* C_8 + C_9 + C_{10} + C_{11}$$

$$D_5 = -2\ell_c^{*3} C_2 + 5\ell_c^{*2} C_3 - 4\ell_c^* C_4 + C_5 + 2\ell_c^{*2} C_7 + \ell_c^{*2} C_8$$

$$- 3\ell_c^* C_9 - 2\ell_c^* C_{10} - 2\ell_c^* C_{11} + C_{12} + C_{13} + C_{14} + C_{15}$$

$$D_6 = -2\ell_c^{*3} C_3 + 5\ell_c^{*2} C_4 - 4\ell_c^* C_5 + 2\ell_c^{*2} C_9 + \ell_c^{*2} C_{10}$$

$$- 2\ell_c^* C_{12} - 3\ell_c^* C_{13} - 2\ell_c^* C_{14} - \ell_c^* C_{15} + C_{16} + C_{17}$$

$$D_7 = -2\ell_c^{*3} C_4 + 5\ell_c^{*2} C_5 + 2\ell_c^{*2} C_{13} + \ell_c^{*2} C_{14} - \ell_c^* C_{16} - 3\ell_c^* C_{17}$$

Reproduced with permission of the copyright owner. Further reproduction prohibited without permission.

$$D_s = -2\ell_c^{*3} C_5 + 2\ell_c^{*2} C_{17}$$

where $C_1 = -\mathcal{N}_o^* (1+V_{gj}^*)\frac{2}{3}(A^*)^2 \ell_c^{*3}$

$$C_2 = \tau_{12}^* + \frac{\Delta\ell^*}{\bar{v}_{fi}^* \sqrt{A^*}} \tan^{-1}\left(\ell_c^* \sqrt{A^*}\right) - \mathcal{N}_o^* (1+V_{gj}^*) \ln C_{k,CD}^*$$
$$+ \mathcal{N}_o^* (1+V_{gj}^*) A^* \ell_c^{*2} + \frac{(1+V_{gj}^*)(1-\ell_c^* \mathcal{N}_o^*)}{\ell_c^*} \ln\left(C_{k,DE}^*\right)$$
$$- \frac{g^* \mathcal{N}_o^* \Delta\ell^*}{\bar{v}_{fi}^* C_k^*(\lambda)} \left\{ \ell_c^* - \frac{1}{\sqrt{A^*}} \tan^{-1}\left(\ell_c^* \sqrt{A^*}\right)\right\}$$
$$- \frac{\bar{C}_{m,c} f_f}{2 D_h} \bar{v}_{fi}^* (1+2V_{gj}^*) \mathcal{N}_o^* \left\{ \frac{2}{3}(A^*)^2 \ell_c^{*3} + \frac{2}{5}(A^*)^3 \ell_c^{*5} \right\}$$

$$C_3 = 2\left(k_i + \frac{f_f \bar{\lambda}^*}{2 D_h^*} + k_e\right) - 2\ell_c^* \mathcal{N}_o^* (1+k_e) - (1+V_{gj}^*) \ln C_{k,CE}^*$$
$$+ (1+V_{gj}^*) A^* \ell_c^{*2} + \frac{g^* \mathcal{N}_o^*}{\bar{v}_{fi}^*} \left[\ln C_{k,CD}^* - A^* \ell_c^{*2} \right]$$
$$+ \frac{\bar{C}_{m,c} f_f}{2 D_h^*} \left[\Delta\ell^* \ell_c^* \left(2 - \ell_c^* \mathcal{N}_o^*\right) + \bar{v}_{fi}^* (1+2V_{gj}^*) \mathcal{N}_o^* \cdot \right.$$
$$\left. \left\{ A^* \ell_c^{*2} + \frac{1}{2} A^{*2} \ell_c^{*4} \right\} \right] + \frac{\bar{C}_{m,D} f_f}{2 D_h^*} 2 (1 - \ell_c^* \mathcal{N}_o^*)(1 - \bar{\lambda}_{CD}^*)$$

$$C_4 = -2(1+k_e)\ell_c^* + \frac{g^*}{\bar{v}_{fi}^*} \left\{ \ln C_{k,CD}^* + \ell_c^* \mathcal{N}_o^* \right\}$$
$$+ \frac{\bar{C}_{m,c} f_f}{2 D_h^*} \left[-\Delta\ell^* \ell_c^{*2} + \bar{v}_{fi}^* (1+2V_{gj}^*) \left\{ A^* \ell_c^{*2} + \frac{1}{2} A^{*2} \ell_c^{*4} \right\} \right]$$

(continued)

Reproduced with permission of the copyright owner. Further reproduction prohibited without permission.

$$- \frac{\bar{C}_{m,D}\, f_f}{2 D_h^*}\, 2 \ell_c^* \left(1 - \bar{\lambda}_{CD}^*\right)$$

$$C_5 = \frac{g^* \ell_c^*}{\bar{v}_{fi}^*}$$

$$C_6 = - \mathcal{N}_o^* \left(1 + V_{gj}^*\right) A^* \ell_c^{*2} C_{k,CD}^*$$

$$C_7 = \left(1 + V_{gj}^*\right)\left(1 - \ell_c^* \mathcal{N}_o^*\right) \ln C_{k,DE}^* + \left(1 + V_{gj}^*\right) \ell_c^* \mathcal{N}_o^* C_{k,CD}^*$$

$$C_8 = - \frac{\bar{C}_{m,D}\, f_f}{2 D_h^*}\, \bar{v}_{fi}^* \left(1 + 2 V_{gj}^*\right) \mathcal{N}_o^* A^* \ell_c^{*2} \left(C_{k,CD}^*\right)^2$$

$$C_9 = - \left(1 + V_{gj}^*\right) \ell_c^* \ln C_{k,DE}^* + \left(1 + V_{gj}^*\right) \ell_c^* C_{k,CD}^*$$

$$+ \frac{g^*}{\bar{v}_{fi}^*} \left(1 - \ell_c^* \mathcal{N}_o^*\right) \left\{ \frac{1}{C_{k,CD}^*} - \frac{1}{C_{k,CE}^*} \right\} + \frac{\left(1 + k_e\right)\left(1 + 2 V_{gj}^*\right) \ell_c^* \left(1 - \ell_c^* \mathcal{N}_o^*\right)}{\left(1 + V_{gj}^*\right)}$$

$$+ \frac{\bar{C}_{m,D}\, f_f}{2 D_h^*} \frac{\left(1 + 2 V_{gj}^*\right)}{\left(1 + V_{gj}^*\right)} \ell_c^* \left(1 - \ell_c^* \mathcal{N}_o^*\right)\left(1 - \bar{\lambda}_{CD}^*\right)$$

$$+ \frac{\rho_g^* V_{gj}^{*2} \left(1 - 2 C_{k,CE}^*\right) \ell_c^* \left(1 - \ell_c^* \mathcal{N}_o^*\right)}{\left(1 + V_{gj}^*\right)}$$

$$C_{10} = \frac{\bar{C}_{m,D}\, f_f}{2 D_h^*}\, \bar{v}_{fi}^* \left(1 + 2 V_{gj}^*\right) \ell_c^* \mathcal{N}_o^* \left(C_{k,CD}^*\right)^2$$

$$C_{11} = - \left(1 + V_{gj}^*\right) \ell_c^* \left(1 - \ell_c^* \mathcal{N}_o^*\right)$$

$$C_{12} = \left(1 + V_{gj}^*\right) \ell_c^{*2}$$

Reproduced with permission of the copyright owner. Further reproduction prohibited without permission.

$$C_{13} = -\frac{(1+k_e)(1+2V_{gj}^*)}{(1+V_{gj}^*)}\,\ell_c^{*2} - \frac{g^*\ell_c^*}{\bar{v}_{fi}^*}\left\{\frac{1}{C_{k,CD}^*} - \frac{1}{C_{k,CE}^*}\right\}$$

$$- \frac{g^*\ell_c^*(1-\ell_c^*\mathcal{M}_o^*)}{\bar{v}_{fi}^* C_{k,CD}^*} - \frac{\bar{C}_{m,D}\, f_f}{2D_h^*}\frac{(1+2V_{gj}^*)}{(1+V_{gj}^*)}\,\ell_c^{*2}(1-\bar{\lambda}_{CD}^*)$$

$$- \rho_g^* V_{gj}^{*2}\,\frac{(1-2C_{k,CE}^*)\,\ell_c^{*2}}{(1+V_{gj}^*)}$$

$$C_{14} = \frac{\bar{C}_{m,D}\, f_f}{2D_h^*}\,\bar{v}_{fi}\,(1+2V_{gj}^*)\,\ell_c^*\,(C_{k,CD}^*)^2$$

$$C_{15} = -\frac{\bar{C}_{m,D}\, f_f}{2D_h^*}\,\bar{v}_{fi}^*\,(1+2V_{gj}^*)\,\ell_c^*\,(1-\ell_c^*\mathcal{M}_o^*)\,C_{k,CD}^*$$

$$C_{16} = \frac{\bar{C}_{m,D}\, f_f}{2D_h^*}\,\bar{v}_{fi}^*\,(1+2V_{gj}^*)\,\ell_c^{*2}\,C_{k,CD}^*$$

$$C_{17} = \frac{g^*(\ell_c^*)^2}{\bar{v}_{fi}^* C_{k,CD}^*}$$

$$D_9 = C_{18}$$

$$D_{10} = -4\ell_c^* C_{18} + C_{19} + C_{22}$$

$$D_{11} = 5\ell_c^{*2} C_{18} - 4\ell_c^* C_{19} + C_{20} - 3\ell_c^* C_{22} + C_{23} + C_{24}$$

$$D_{12} = -2\ell_c^{*3} C_{18} + 5\ell_c^{*2} C_{19} - 4\ell_c^* C_{20} + C_{21} + 2\ell_c^{*2} C_{22}$$

$$- 3\ell_c^* C_{23} - 2\ell_c^* C_{24} + C_{25} + C_{26} + C_{27}$$

Reproduced with permission of the copyright owner. Further reproduction prohibited without permission.

$$D_{13} = -2\ell_c^{*3} C_{19} + 5\ell_c^{*2} C_{20} - 4\ell_c^{*} C_{21} + 2\ell_c^{*2} C_{23} + \ell_c^{*2} C_{24}$$

$$-2\ell_c^{*} C_{25} - 3\ell_c^{*} C_{26} - 2\ell_c^{*} C_{27} + C_{28} + C_{29}$$

$$D_{14} = -2\ell_c^{*3} C_{20} + 5\ell_c^{*2} C_{21} + 2\ell_c^{*2} C_{26} + \ell_c^{*2} C_{27}$$

$$-\ell_c^{*} C_{28} - 3\ell_c^{*} C_{29}$$

$$D_{15} = -2\ell_c^{*3} C_{21} + 2\ell_c^{*2} C_{29}$$

where $C_{18} = (1+V_{jj}^{*})\frac{2}{3} A^{*2} \ell_c^{*3}$

$$C_{19} = (1+V_{jj}^{*}) \ln C_{k,CE}^{*} - (1+V_{jj}^{*}) A^{*} \ell_c^{*2} + \frac{g^{*}\Delta t^{*}}{\bar{v}_{fi}^{*} C_k^{*}(\bar{x})}\left\{\ell_c^{*} - \frac{1}{\sqrt{A^{*}}} \tan^{-1}\left(\ell_c^{*}\sqrt{A^{*}}\right)\right\}$$

$$+ \frac{\bar{C}_{m,c} f_f}{2D_h^{*}} \bar{v}_{fi}^{*} (1+2V_{jj}^{*})\left\{\frac{2}{3} A^{*2} \ell_c^{*3} + \frac{2}{5} A^{*3} \ell_c^{*5}\right\}$$

$$C_{20} = 2(1+k_e)\ell_c^{*} - \frac{g^{*}}{\bar{v}_{fi}^{*}} \ln\left(C_{k,CD}^{*}\right) + \frac{g^{*} A^{*} \ell_c^{*2}}{\bar{v}_{fi}^{*}}$$

$$+ \frac{\bar{C}_{m,c} f_f \Delta t^{*} \ell_c^{*2}}{2D_h^{*}} - \frac{\bar{C}_{m,c} f_f}{2D_h^{*}} \bar{v}_{fi}^{*} (1+2V_{jj}^{*})\left\{A^{*} \ell_c^{*2} + \frac{1}{2} A^{*2} \ell_c^{*4}\right\}$$

$$+ \frac{\bar{C}_{m,D} f_f}{2D_h^{*}} 2\ell_c^{*} (1-\bar{\lambda}_{CD}^{*})$$

$$C_{21} = -C_5$$

$$C_{22} = (1+V_{jj}^{*}) A^{*} \ell_c^{*2} C_{k,CD}^{*}$$

Reproduced with permission of the copyright owner. Further reproduction prohibited without permission.

$$C_{23} = (1+V_{gj}^*)\, \ell_c^*\, \ln C_{k,DE}^* - (1+V_{gj}^*)\, \ell_c^*\, C_{k,CD}^*$$

$$C_{24} = \frac{\bar{C}_{m,D}\, f_f}{2D_h^*}\, \bar{v}_{fi}^*\, (1+2V_{gj}^*)\, A^*\, \ell_c^{*2}\, (C_{k,CD}^*)^2$$

$$C_{25} = -C_{12}$$

$$C_{26} = \frac{(1+k_e)(1+2V_{gj}^*)}{(1+V_{gj}^*)}\, \ell_c^{*2} + \frac{g^*\ell_c^*}{\bar{v}_{fi}^*}\left\{\frac{1}{C_{k,CD}^*} - \frac{1}{C_{k,CE}^*}\right\}$$
$$+ \frac{\bar{C}_{m,D}\, f_f}{2D_h^*}\, \frac{(1+2V_{gj}^*)}{(1+V_{gj}^*)}\, \ell_c^{*2}\, (1-\bar{\lambda}_{CD}^*) + \frac{\rho_g^* V_{gj}^{*2}(1-2C_{k,CE}^*)\, \ell_c^{*2}}{(1+V_{gj}^*)}$$

$$C_{27} = -C_{14}$$

$$C_{28} = -C_{16}$$

$$C_{29} = -C_{17}$$

$$D_{16} = C_{30} + C_{34}$$

$$D_{17} = -4\ell_c^* C_{30} + C_{31} - 3\ell_c^* C_{34} + C_{35} + C_{36}$$

$$D_{18} = 5\ell_c^{*2} C_{30} - 4\ell_c^* C_{31} + C_{32} + 2\ell_c^{*2} C_{34} - 3\ell_c^* C_{35}$$
$$- 2\ell_c^* C_{36} + C_{37} + C_{38} + C_{39}$$

$$D_{19} = -2\ell_c^{*3} C_{30} + 5\ell_c^{*2} C_{31} - 4\ell_c^* C_{32} + C_{33} + 2\ell_c^{*2} C_{35}$$

(continued)

Reproduced with permission of the copyright owner. Further reproduction prohibited without permission.

$$+ \ell_c^{*2} C_{36} - 3\ell_c^* C_{37} - 2\ell_c^* C_{38} - 2\ell_c^* C_{39} + C_{40}$$

$$+ C_{41} + C_{42} + C_{43}$$

$$D_{20} = -2\ell_c^{*3} C_{31} + 5\ell_c^{*2} C_{32} - 4\ell_c^* C_{33} + 2\ell_c^{*2} C_{37}$$

$$+ \ell_c^{*2} C_{38} - 2\ell_c^* C_{40} - 3\ell_c^* C_{41} - 2\ell_c^* C_{42} - \ell_c^* C_{43}$$

$$+ C_{44} + C_{45}$$

$$D_{21} = -2\ell_c^{*3} C_{32} + 5\ell_c^{*2} C_{33} + 2\ell_c^{*2} C_{41} + \ell_c^{*2} C_{42}$$

$$- \ell_c^* C_{44} - 3\ell_c^* C_{45}$$

$$D_{22} = -2\ell_c^{*3} C_{33} + 2\ell_c^{*2} C_{45}$$

where

$$C_{30} = -\frac{(1+k_e)(1+2V_{gj}^*)}{(1+V_{gj}^*)} \mathcal{L}_o^* A^* \ell_c^{*2} C_{k,cE}^*$$

$$- \rho_g^* V_{gj}^{*2} \frac{(1-2C_{k,cE}^*)}{(1+V_{gj}^*)} C_{k,cE}^* \mathcal{L}_o^* A^* \ell_c^{*2}$$

$$C_{31} = \frac{(1+k_e)(1+2V_{gj}^*)}{(1+V_{gj}^*)} \ell_c^* \mathcal{L}_o^* C_{k,cE}^* + \frac{g^* \mathcal{L}_o^* A^* \ell_c^{*2}}{\bar{v}_{fi}^*}$$

$$+ \rho_g^* V_{gj}^{*2} \frac{(1-2C_{k,cE}^*)}{(1+V_{gj}^*)} C_{k,cE}^* \ell_c^* \mathcal{L}_o^*$$

Reproduced with permission of the copyright owner. Further reproduction prohibited without permission.

$$C_{32} = (1+k_e)\frac{(1+2V_{gj}^*)}{(1+V_{gj}^*)}\lambda_c^* C_{k,CE}^* - \frac{g^*\lambda_c^*\Lambda_o^*}{\bar{v}_{fi}^*} + \frac{\rho_g^* V_{gj}^{*2} C_{k,CE}^*(1-2C_{k,CE}^*)\lambda_c^*}{(1+V_{gj}^*)}$$

$$C_{33} = -C_5$$

$$C_{34} = (1+V_{gj}^*)\Lambda_o^* A^* \lambda_c^{*2} C_{k,CE}^*$$

$$C_{35} = -(1+V_{gj}^*)\lambda_c^*\Lambda_o^* C_{k,CE}^*$$

$$C_{36} = -C_8\left(C_{k,DE}^*\right)^2$$

$$C_{37} = -(1+V_{gj}^*)\lambda_c^* C_{k,CE}^* - (1+k_e)\frac{(1+2V_{gj}^*)}{(1+V_{gj}^*)}\lambda_c^*(1-\lambda_c^*\Lambda_o^*)C_{k,DE}^*$$
$$- \rho_g^* V_{gj}^{*2}\frac{(1-2C_{k,CE}^*)}{(1+V_{gj}^*)} C_{k,DE}^*\lambda_c^*(1-\lambda_c^*\Lambda_o^*)$$

$$C_{38} = -C_{10}\left(C_{k,DE}^*\right)^2$$

$$C_{39} = -C_{11} C_{k,DE}^*$$

$$C_{40} = -C_{12} C_{k,DE}^*$$

$$C_{41} = (1+k_e)\frac{(1+2V_{gj}^*)}{(1+V_{gj}^*)}\lambda_c^{*2} C_{k,DE}^* + \frac{g^*\lambda_c^*(1-\lambda_c^*\Lambda_o^*)}{\bar{v}_{fi}^*} C_{k,CD}^*$$
$$+ \rho_g^* V_{gj}^{*2}\frac{(1-2C_{k,CE}^*)}{(1+V_{gj}^*)}\lambda_c^{*2} C_{k,DE}^*$$

Reproduced with permission of the copyright owner. Further reproduction prohibited without permission.

$$C_{42} = -C_{14}\left(C^*_{k,DE}\right)^2$$

$$C_{43} = -C_{15}\left(C^*_{k,DE}\right)^2$$

$$C_{44} = -C_{16}\left(C^*_{k,DE}\right)^2$$

$$C_{45} = -C_{17}$$

$$D_{23} = C_{46} + C_{49}$$

$$D_{24} = -4\ell_c^* C_{45} + C_{47} - 3\ell_c^* C_{49} + C_{50} + C_{51}$$

$$D_{25} = 5\ell_c^{*2} C_{46} - 4\ell_c^* C_{47} + C_{48} + 2\ell_c^{*2} C_{49} - 3\ell_c^* C_{50}$$
$$- 2\ell_c^* C_{51} + C_{52} + C_{53} + C_{54}$$

$$D_{26} = -2\ell_c^{*3} C_{46} + 5\ell_c^{*2} C_{47} - 4\ell_c^* C_{48} + 2\ell_c^{*2} C_{50} + \ell_c^{*2} C_{51}$$
$$- 2\ell_c^* C_{52} - 3\ell_c^* C_{53} - 2\ell_c^* C_{54} + C_{55} + C_{56}$$

$$D_{27} = -2\ell_c^{*3} C_{47} + 5\ell_c^{*2} C_{48} + 2\ell_c^{*2} C_{53} + \ell_c^{*2} C_{54}$$
$$- \ell_c^* C_{55} - 3\ell_c^* C_{56}$$

$$D_{28} = -2\ell_c^{*3} C_{48} + 2\ell_c^{*2} C_{56}$$

Reproduced with permission of the copyright owner. Further reproduction prohibited without permission.

where

$$C_{46} = (1+k_e)\frac{(1+2V_{gj}^*)}{(1+V_{gj}^*)} A^* (\ell_c^*)^2 C_{k,CE}^* + \rho_g^* V_{gj}^{*2} \frac{(1-2C_{k,CE}^*)}{(1+V_{gj}^*)} A^* \ell_c^{*2} C_{k,CE}^*$$

$$C_{47} = -(1+k_e)\frac{(1+2V_{gj}^*)}{(1+V_{gj}^*)} \ell_c^* C_{k,CE}^* - \frac{g^* A^* \ell_c^{*2}}{\bar{v}_{fi}^*} - \rho_g^* V_{gj}^{*2} \frac{(1-2C_{k,CE}^*)}{(1+V_{gj}^*)} C_{k,CE}^* \ell_c^*$$

$$C_{48} = C_5$$

$$C_{49} = -(1+V_{gj}^*) A^* \ell_c^{*2} C_{k,CE}^*$$

$$C_{50} = (1+V_{gj}^*) \ell_c^* C_{k,CE}^*$$

$$C_{51} = -C_{24} (C_{k,DE}^*)^2$$

$$C_{52} = -C_{40}$$

$$C_{53} = -(1+k_e)\frac{(1+2V_{gj}^*)}{(1+V_{gj}^*)} \ell_c^{*2} C_{k,DE}^* - \rho_g^* V_{gj}^{*2} \frac{(1-2C_{k,CE}^*)}{(1+V_{gj}^*)} \ell_c^* C_{k,DE}^*$$

$$C_{54} = -C_{42}$$

$$C_{55} = -C_{44}$$

$$C_{56} = C_{17}$$

Reproduced with permission of the copyright owner. Further reproduction prohibited without permission.

The useful identities are:

$$D_8 + D_{15} \equiv 0$$

$$D_{15} + D_{28} \equiv 0$$

$$D_{22} + D_{28} \equiv 0$$

and $$D_7 + D_{14} + D_{21} + D_{27} \equiv 0$$

because

$$C_4 + C_{20} + C_{32} + C_{47} \equiv 0$$

$$C_5 + C_{21} + C_{33} + C_{48} \equiv 0$$

$$C_{13} + C_{26} + C_{41} + C_{53} \equiv 0$$

$$C_{14} + C_{27} + C_{42} + C_{54} \equiv 0$$

$$C_{16} + C_{28} + C_{44} + C_{55} \equiv 0$$

$$C_{17} + C_{29} + C_{45} + C_{56} \equiv 0$$

Reproduced with permission of the copyright owner. Further reproduction prohibited without permission.

APPENDIX B

THE PROGRAM "INSTAB"

B-1. The Flow Diagram

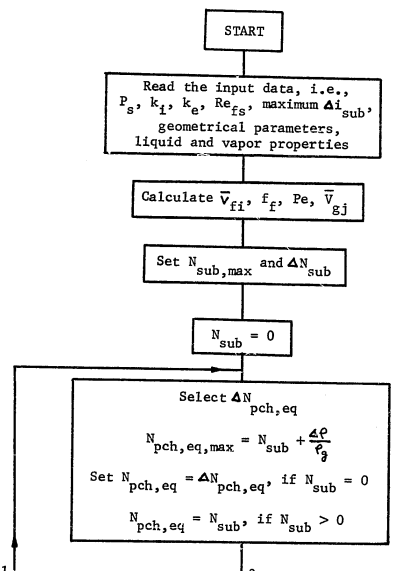

Reproduced with permission of the copyright owner. Further reproduction prohibited without permission.

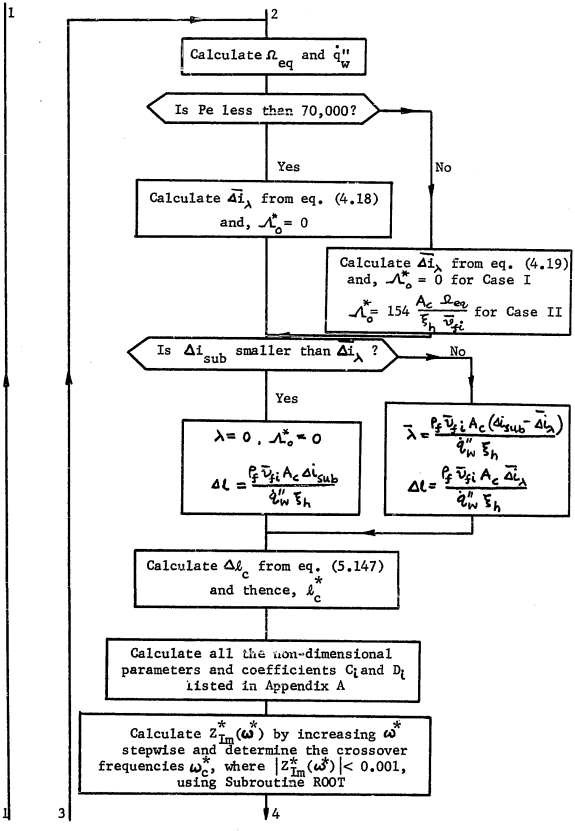

Reproduced with permission of the copyright owner. Further reproduction prohibited without permission.

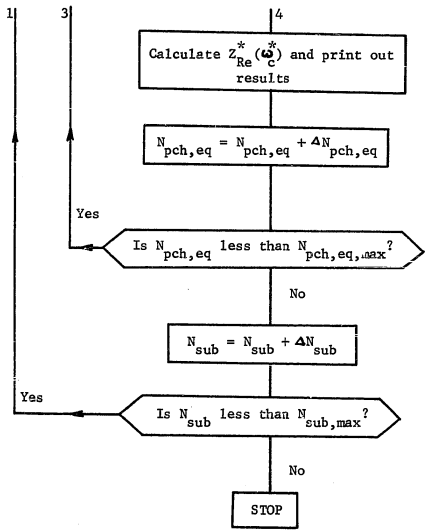

Reproduced with permission of the copyright owner. Further reproduction prohibited without permission.

B-2. The Listing of the Program

```
C   TWO PHASE FLOW INSTABILITY WITH THERMAL NON -EQUILIBRIUM
      DIMENSION FIMAG(500)
      COMMON X(500),ZIMAG(500),D(60),ROW,TIMAG,ROZR,L
      REAL KI,KE,LE,LH,N,LAMDA
      READ(5,101) PS,RE,KI,KE,SUBM
  101 FORMAT(5F16.2)
      READ(5,102) LE,HP,AC,DH,G,ANGV
  102 FORMAT(4F15.7,2F1.-4)
      READ(5,103) DENF,DENG,CPF,CONDF,VISF,SIGMA,LH
  103 FORMAT(6F12.7,F8.4)
      VFI=RE*VISF/(DENF*DH)
      FF=0.184/(RF**0.2)
      XD=DH/LE
      CMC=2.0
      CMD=2.0
      FFGC=C/C*FF/(2*XD)
      FFGD=CMD*FF/(2*XD)
      PR=VISF*CPF/CONDF
      PE=RE*PR
      VGJ=1.41*(G*SIGMA*(DENF-DENG)/(DENF**2))**0.25
      WRITE(6,210) PS,RE,PE,VFI,VGJ,KI,KE
  210 FORMAT (5X,25HSYSTEM PRESSURE          =,F10.1,3X,4HPSIA/,5X,
     125HREYNOLDS NUMBER             =,F12.1,/,5X,
     225HPECLET NUMBER               =,F12.1,/,5X,
     325HINLET VELOCITY              =,F12.4,3X,6HFT/SEC/,5X,
     425HDRIFT VELOCITY              =,F12.4,3X,6HFT/SEC/,5X,
     525HINLET ORIFICE COEF          =,F12.4,/,5X,
     625HOUTLET ORIFICE COFF         =,F12.4)
      WRITE(6,211) LE,HP,AC,DH,G
  211 FORMAT (5X,25HLENGTH OF TEST SECTION  =,F12.1,3X,2HFT/,5X,
     125HHEATED PERIMETER            =,F12.6,3X,2HFT/,5X,
     225HAREA OF CROSS SECTION       =,F12.7,3X,4HSQFT/,5X,
     325HHYD. DIAMETER               =,F12.6,3X,2HFT/,5X,
     425HGRAVITY ACCL COEF           =,F12.4,3X,7HFT/SEC2)
      WRITE(6,212) DENF,DENG,CPF,CONDF,VISF,SIGMA,LH
  212 FORMAT (5X,25HSAT. LIQUID DENSITY     =,F12.4,3X,7HLBM/FT3/,5X,
     125HSAT. VAPOR DENSITY          =,F12.6,3X,7HLBM/FT3/,5X,
     225HLIQUID SPECIFIC HEAT        =,F12.6,3X,9HBTU/LBM-F/,5X,
     325HLIQUID THERMAL COND.        =,F12.6,3X,12HBTU/SEC-FT-F/,5X,
     425HSAT. LIQUID VISCOSITY       =,F12.6,3X,10HLBM/SEC-FT/,5X,
     525HSURFACE TENSION             =,F12.6,3X,8HLBM/SEC2/,5X,
     625HLATENT HEAT                 =,F12.4,3X,7HBTU/LBM/////,
     74X,3HSUB,7X,3HPCH,6X,5HOMEGA,5X,6HXLAMDA,6X,3HXLC,7X,2HWC,6X,
     85HSTABN,6X,7HRESULTS,6X,6HZREALC,6X,6HZIMAGC//)
      XVGJ=VGJ/VFI
      SUBUL=(DENF-DENG)*SUBM/(DENG*LH)
      SUBDEL=SUBUL/20.0
      SUB=0.0
   55 DISUB=SUB*DENG*LH/(DENF-DENG)
      DELPCH=(DENF-DENG)/(4.00*DENG)
      PCHM=SUB*(DENF-DENG)/DENG
      PCH=SUB
      IF(PCH.LE.0.) PCH=PCH+DELPCH
   50 OMEGA=PCH+VFI/LE
      O=OMEGA*AC*LH*DENF*DENG/(HP*(DENF-DENG))
      IF(PE-7000C.C) 60,60,61
   60 DELIL=0.0022*N*DH*CPF/CONDF
      N=0.
      GO TO 62
   61 DELIL=154*G/(DENF*VFI)
      N=0.0   For Case I ,   N = 154 * Ac * OMEGA /(HP * VFI) For Case II.
   62 IF(DISUB-DELIL)70,70,71
   70 LAMDA=0.
```

Reproduced with permission of the copyright owner. Further reproduction prohibited without permission.

```
      N=0.0
      DELL=DENF*VFI*AC*DISUB/(Q*HP)
      GO TO 72
   71 LAMDA=DENF*VFI*AC*(DISUB-DELIL)/(Q*HP)
      DELL=DENF*VFI*AC*DELIL/(Q*HP)
   72 IF(ABS(DELL)-0.0001) 80,80,73
   73 DUM1=LE-LAMDA
      DUM2=DUM1**2-2*DELL*(DUM1-DELL*(1-EXP(-DUM1/DELL)))
      DELLC=DUM1-SQRT(DUM2)
      XLC=DELLC/DELL
      GO TO 81
   80 XLC=1.0
   81 IF(XLC-LE.0.) GO TO 51
      IF(XLC-0.1.) GO TO 51
      XLC2=XLC**2
      XLC3=XLC**3
      XLC4=XLC**4
      XLC5=XLC**5
      XDENG=DENG/DENF
      XLAMDA=LAMDA/LE
      XDELL=DELL/LE
      XVFI=1/PCH
      XCKL=XVFI*(1+XVGJ)
      XLCD=XLAMDA+XLC*XDELL
      XA=XDELL/(2.0*XCKL)
      XA2=XA**2
      XA3=XA**3
      CKCD=1+XA*(XLC**2)
      CKDE=1+XLC*(1-XLCD)/(CKCD*XCKL)
      CKCE=CKCD*CKDE
      T12=XLAMDA/XVFI
      T34=ALOG(CKDE)/XLC
      TSP=T12+T34
      XG=G/(OMEGA**2)*LE)
      BUM1=SQRT(XA)
      IF(BUM1-LE.0.) GO TO 900
      BUM=ATAN(BUM1*XLC)/BUM1
      GO TO 901
  900 BUM=XLC
  901 YLCD=ALOG(CKCD)
      YLCE=ALOG(CKCE)
      YLDE=ALOG(CKDE)
      C1=-N*(1+XVGJ)*(2./3.)*XA2*XLC3
      C2=T12+XDELL*DUM/XVFI-N*(1+XVGJ)*YLCD+N*(1+XVGJ)*XA*XLC2+(1+XVGJ)*
     1(1-XLC*N)*YLDE/XLC-XG*N*XDELL*(XLC-BUM)/(XVFI*XCKL)-FFGC*XVFI*
     2(1+XVGJ)*N*((2./3.)*XA2*XLC3+(2./5.)*XA3*XLC5)
      C3=2*(K)+FF*XLAMDA/(2*XD)+KF)-2*XLC*N*(1+CF)-(1+XVGJ)*YLCE+(1+XVGJ
     1)*XA*XLC2+XC**N*(YLCD-XA*XLC2)/XVFI+FFGC*(XDELL*XLC*(2-XLC*N)+
     2XVFI*(1+2*XVGJ)*N*(XA*XLC2+0.5*XA2*XLC4)+FFGD*2.0*(1-XLC*N)*
     3(1-XLCD)
      C4=-2*(1+KF)*XLC+XG*(YLCD+XLC*N)/XVFI+FFGC*(-XDELL*XLC2+XVFI*
     1(1+2*XVGJ)*(XA*XLC2+0.5*XA2*XLC4))-FFGD*2.0*XLC*(1-XLCD)
      C5=XG*XLC/XVFI
      C6=-N*(1+XVGJ)*XA*XLC2*CKCD
      C7=(1+XVGJ)*(1-XLC*N)*YLDE+(1+XVGJ)*XLC*N*CKCD
      C8=-FFGD*XVFI*(1+2*XVGJ)*N*XA*XLC2*(CKCD**2)
      C9=(1+XVGJ)*XLC*(CKCD-YLDE)+XG*(1-XLC*N)*(1/CKCD-1/CKCE)/XVFI+
     1(1+KF)*(1+2*XVGJ)*XLC*(1-XLC*N)/(1+XVGJ)+FFGC*(1+2*XVGJ)*XLC*
     2(1-XLC*N)*(1-XLCD)/(1+XVGJ)+XDENG*(XVGJ**2)*(1-2*CKCF)*XLC*
     3(1-XLC*N)/(1+XVGJ)
      C10=FFGD*XVFI*(1+2*XVGJ)*XLC*N*(CKCD**2)
      C11=-(1+XVGJ)*XLC*(1-XLC*N)
      C12=(1+XVGJ)*XLC2
```

Reproduced with permission of the copyright owner. Further reproduction prohibited without permission.

```
      C13=-(1+KF)*(1+2*XVGJ)*XLC2/(1+XVGJ)-XG*XLC*(1/CKCD-1/CKCE)/XVFI
     1-XG*XLC*(1-XLC**N)/(XVFI*CKCD)-FFGD*(1+2*XVGJ)*XLC2*(1-XLCD)/(1+
     2XVGJ)-XDENG*(XVGJ**2)*(1-2*CKCE)*XLC2/(1+XVGJ)
      C14=FFGD*XVFI*(1+2*XVGJ)*XLC*(CKCD**2)
      C15=-FFGD*XVFI*(1+2*XVGJ)*XLC*(1-XLC**N)*CKCD
      C16=FFGD*XVFI*(1+2*XVGJ)*XLC2*CKCD
      C17=XG*XLC2/(XVFI*CKCD)
      D(1)=C1
      D(2)=-4*XLC*C1+C2+C6
      D(3)=5*XLC2*C1-4*XLC*C2+C3-3*XLC*C6+C7+C8
      D(4)=-2*XLC*C1+5*XLC2*C2-4*XLC*C3+C4+2*XLC2*C6-3*XLC*C7-2*XLC*C8+
     1C9+C10+C11
      D(5)=-2*XLC*C2+5*XLC2*C3-4*XLC*C4+C5+2*XLC2*C7+XLC2*C8-3*XLC*C9-
     12*XLC*C10-2*XLC*C11+C12+C13+C14+C15
      D(6)=-2*XLC*C3+5*XLC2*C4-4*XLC*C5+2*XLC2*C9+XLC2*C10-2*XLC*C12-
     13*XLC*C13-2*XLC*C14-XLC*C15+C16+C17
      D(7)=-2*XLC*C4+5*XLC2*C5+2*XLC2*C13+XLC2*C14-XLC*C16-3*XLC*C17
      D(8)=-2*XLC*C5+2*XLC2*C17
      C18=(2./3.)*(1+XVGJ)*XA2*XLC3
      C19=(1+XVGJ)*XLC5-(1+XVGJ)*XA*XLC2+XG*XDELL*(XLC-RUNT)/(XVFI*XCKL)+
     1FFGC*XVFI*(1+2*XVGJ)*((2./3.)*XA2*XLC3+(2./3.)*XA3*XLC5)
      C20=2*(1+KF)*XLC-XG*XLCD/XVFI+XG*XA*XLC2/XVFI+FFGC*XDELL*XLC2-
     1FFGC*XVFI*(1+2*XVGJ)*(XA*XLC2+0.5*XA2*XLC4)+FFGD*2*XLC*(1-XLCD)
      C21=-C5
      C22=(1+XVGJ)*XA*XLC2*CKCD
      C23=(1+XVGJ)*XLC*(YLDE-CKCD)
      C24=FFGD*XVFI*(1+2*XVGJ)*XA*XLC2*(CKCD**2)
      C25=-C12
      C26=(1+KE)*(1+2*XVGJ)*XLC2/(1+XVGJ)+XG*XLC*(1/CKCD-1/CKCE)/XVFI+
     1FFGD*(1+2*XVGJ)*XLC2*(1-XLCD)/(1+XVGJ)+XDENG*(XVGJ**2)*(1-2*CKCE)*
     2XLC2/(1+XVGJ)
      C27=-C14
      C28=-C16
      C29=-C17
      D(9)=C18
      D(10)=-4*XLC*C18+C19+C22
      D(11)=5*XLC2*C18-4*XLC*C19+C20-3*XLC*C22+C23+C24
      D(12)=-2*XLC3*C18+5*XLC2*C19-4*XLC*C20+C21+2*XLC2*C29-3*XLC*C23-
     12*XLC*C24+C25+C26+C27
      D(13)=-2*XLC3*C19+5*XLC2*C20-4*XLC*C21+2*XLC2*C23+XLC2*C24-
     12*XLC*C25-3*XLC*C26-2*XLC*C27+C28+C29
      D(14)=-2*XLC3*C20+5*XLC2*C21+2*XLC2*C26+XLC2*C27-XLC*C28-3*XLC*C29
      D(15)=-2*XLC3*C21+2*XLC2*C29
      C30=-(1+KE)*(1+2*XVGJ)*N*XA*XLC2*CKCE/(1+XVGJ)-XDENG*(XVGJ**2)*
     1(1-2*CKCE)*CKCE*N*XA*XLC2/(1+XVGJ)
      C31=(1+KE)*(1+2*XVGJ)*XLC**2*CKCE/(1+XVGJ)+XG*N*XA*XLC2/XVFI+XDENG*
     1(XVGJ**2)*CKCE*(1-2*CKCE)*XLC*N/(1+XVGJ)
      C32=(1+KE)*(1+2*XVGJ)*XLC*CKCE/(1+XVGJ)-XG*XLC*N/XVFI+XDENG*
     1(XVGJ**2)*CKCE*(1-2*CKCE)*XLC/(1+XVGJ)
      C33=-C5
      C34=(1+XVGJ)*N*XA*XLC2*CKCE
      C35=-(1+XVGJ)*XLC*N*CKCE
      C36=-C8*(CKDE**2)
      C37=-(1+XVGJ)*XLC*CKCF-(1+KF)*(1+2*XVGJ)*XLC*(1-XLC*N)*CKDF/(1+
     1XVGJ)-XDENG*(XVGJ**2)*(1-2*CKCE)*CKDF*XLC*(1-XLC*N)/(1+XVGJ)
      C38=-C13*(CKDE**2)
      C39=-C11*CKDE
      C40=-C12*CKDE
      C41=(1+KE)*(1+2*XVGJ)*XLC2*CKDE/(1+XVGJ)+XG*XLC*(1-XLC*N)/(XVFI*
     1CKCD)+XDENG*(XVGJ**2)*(1-2*CKCE)*XLC2*CKDE/(1+XVGJ)
      C42=-C14*(CKDE**2)
      C43=-C15*(CKDE**2)
      C44=-C16*(CKDE**2)
```

Reproduced with permission of the copyright owner. Further reproduction prohibited without permission.

```
      C45=-C17
      D(16)=C30+C34
      D(17)=-4*XLC*C30+C31-3*XLC*C34+C35+C36
      D(18)=5*XLC2*C30-4*XLC*C31+C32+2*XLC2*C34-3*XLC*C35-2*XLC*C36+C37+
     1C38+C39
      D(19)=-2*XLC3*C30+5*XLC2*C31-4*XLC*C32+C33+2*XLC2*C35+XLC2*C36-
     13*XLC*C37-2*XLC*C38-2*XLC*C39+C40+C41+C42+C43
      D(20)=-2*XLC3*C31+5*XLC2*C32-4*XLC*C33+2*XLC2*C37+XLC2*C38-2*XLC*
     1C40-3*XLC*C41-2*XLC*C42-XLC*C43+C44+C45
      D(21)=-2*XLC3*C32+5*XLC2*C33+2*XLC2*C41+XLC2*C42-XLC*C44-3*XLC*C45
      D(22)=-2*XLC3*C33+2*XLC2*C45
      C46=(1+KE)*(1+2*XVGJ)*XA*XLC2*CKCE/(1+XVGJ)+XDENG*(XVGJ**2)*(1-2*
     1CKCE)*XA*XLC2*CKCE/(1+XVGJ)
      C47=-(1+KE)*(1+2*XVGJ)*XLC*CKCE/(1+XVGJ)-XG*XA*XLC2/XVFI-XDENG*
     1(XVGJ**2)*CKCE*(1-2*CKCE)*XLC/(1+XVGJ)
      C48=C5
      C49=-(1+XVGJ)*XA*XLC2*CKCE
      C50=(1+XVGJ)*XLC*CKCE
      C51=-C24*(CKDE**2)
      C52=-C40
      C53=-(1+KE)*(1+2*XVGJ)*XLC2*CKDE/(1+XVGJ)-XDENG*(XVGJ**2)*(1-2*
     1CKCE)*XLC*CKDE/(1+XVGJ)
      C54=-C42
      C55=-C44
      C56=C17
      D(23)=C46+C49
      D(24)=-4*XLC*C46+C47-3*XLC*C49+C50+C51
      D(25)=5*XLC2*C46-4*XLC*C47+C48+2*XLC2*C49-3*XLC*C50-2*XLC*C51+C52+
     1C53+C54
      D(26)=-2*XLC3*C46+5*XLC2*C47-4*XLC*C48+2*XLC2*C50+XLC2*C51-2*XLC*
     1C52-3*XLC*C53-2*XLC*C54+C55+C56
      D(27)=-2*XLC3*C47+5*XLC2*C48+2*XLC2*C53+XLC2*C54-XLC*C55-3*XLC*C56
      D(28)=-2*XLC3*C48+2*XLC2*C56
      W(1)=0.0
      ZIMAG(1)=0.0
      DELW=0.02
      DO 300 I=1,250
      J=I+1
      W(J)=W(I)+DELW
      FI=-D(1)*W(J)**7+D(3)*W(J)**5-D(5)*W(J)**3+D(7)*W(J)
      FR1=-D(2)*W(J)**6+D(4)*W(J)**4-D(6)*W(J)**2+D(8)
      FR2=-D(9)*W(J)**6+D(11)*W(J)**4-D(13)*W(J)**2+D(15)
      FR3=D(10)*W(J)**5-D(12)*W(J)**3+D(14)*W(J)
      FR4=-D(16)*W(J)**6+D(18)*W(J)**4-D(20)*W(J)**2+D(22)
      FR5=D(17)*W(J)**5-D(19)*W(J)**3+D(21)*W(J)
      FR6=D(24)*W(J)**4-D(26)*W(J)**2+D(28)
      FR7=D(23)*W(J)**5-D(25)*W(J)**3+D(27)*W(J)
      FIMAG(J)=FI+FR3*COS(W(J)*T12)-FR2*SIN(W(J)*T12)+FR5*COS(W(J)*T34)-
     1FR4*SIN(W(J)*T34)+FR7*COS(W(J)*TSP)-FR6*SIN(W(J)*TSP)
      ZIMAG(J)=-FIMAG(J)/(W(J)**2)
      IF(ABS(ZIMAG(J))-0.0001) 305,305,304
  304 IF(ZIMAG(I)/ZIMAG(J)) 301,300,300
  305 WC=W(J)
      ZIMAGC=ZIMAG(J)
      FREALC=FR1+FR2*COS(WC*T12)+FR3*SIN(WC*T12)+FR4*COS(WC*T34)+
     1FR5*SIN(WC*T34)+FR6*COS(WC*TSP)+FR7*SIN(WC*TSP)
      ZREALC=-FREALC/(WC**2)
      L=0
      GO TO 400
  301 CALL ROOT(I,T12,T34,TSP)
      IF(L-21)306,307,307
  307 WRITE(6,308)
  308 FORMAT(2X,27HITERATION STEPS ARE OVER 20)
```

Reproduced with permission of the copyright owner. Further reproduction prohibited without permission.

```
      GO TO 300
  306 WC=ROW
      ZREALC=ROZR
      ZIMAGC=TIMAG
  400 STABN=-ZREALC
      IF(ABS(STABN)-0.005) 515,515,520
  515 WRITE(6,202) SUB,PCH,OMEGA,XLAMDA,XLC,WC,STABN,ZREALC,ZIMAGC
  202 FORMAT(7F10.4,3X,12HST. BOUNDARY,2(2X,E12.4))
      GO TO 300
  520 WRITE(6,201) SUB,PCH,OMEGA,XLAMDA,XLC,WC,STABN,ZREALC,ZIMAGC
  201 FORMAT(7F10.4,3X,12H CROSS OVER ,2(2X,E12.4))
  300 CONTINUE
      PCH=PCH+DELPCH
      IF(PCH-PCHM) 50,50,52
   52 SUB=SUB+SUBDEL
      IF(SUB-SUBUL) 55,55,56
   51 STOP
   56 CALL EXIT
      END
```

Reproduced with permission of the copyright owner. Further reproduction prohibited without permission.

```
      SUBROUTINE ROOT(I,T12,T34,TSP)
      COMMON W(500),ZIMAG(500),D(60),ROW,TIMAG,ROZR,L
      L=1
      J=I+1
      TW=W(J)
      TIMAG=ZIMAG(J)
    1 DEL=(TW-W(I))*(ZIMAG(I)/(ZIMAG(I)-TIMAG))
      V=W(I)+DEL
      V1=-D(1)*V**7+D(3)*V**5-D(5)*V**3+D(7)*V
      V1=-D(2)*V**6+D(4)*V**4-D(6)*V**2+D(8)
      V2=-D(9)*V**6+D(11)*V**4-D(13)*V**2+D(15)
      V3=D(10)*V**5-D(12)*V**3+D(14)*V
      V4=-D(16)*V**6+D(18)*V**4-D(20)*V**2+D(22)
      V5=D(17)*V**5-D(19)*V**3+D(21)*V
      V6=D(24)*V**4-D(26)*V**2+D(28)
      V7=D(23)*V**5-D(25)*V**3+D(27)*V
      VIMAG=V1+V3*COS(V*T12)-V2*SIN(V*T12)+V5*COS(V*T34)-V4*SIN(V*T34)+
     1V7*COS(V*TSP)-V6*SIN(V*TSP)
      TIMAG=-VIMAG/(V**2)
      IF(ABS(TIMAG)-0.001) 6,6,7
    6 VREAL=V1+V2*COS(V*T12)+V3*SIN(V*T12)+V4*COS(V*T34)+V5*SIN(V*T34)+
     1V6*COS(V*TSP)+V7*SIN(V*TSP)
      ROZR=-VREAL/(V**2)
      ROW=V
      GO TO 10
    7 TW=V
      L=L+1
      IF(L-20)1,1,10
   10 RETURN
      END
```

Reproduced with permission of the copyright owner. Further reproduction prohibited without permission.

APPENDIX C

REDUCED EXPERIMENTAL DATA FOR COMPARISON WITH THEORETICAL PREDICTION

By definition:

$$N_{sub} = \frac{\Delta\rho}{\rho_g}\frac{\Delta i_{sub}}{\Delta i_{fg}}$$

$$N_{pch,eq} = \frac{\Omega_{eq}\, l}{\overline{v}_{fi}} = \frac{\dot{q}''_w\, \xi_h}{A_c\, \Delta i_{fg}}\frac{\Delta\rho}{\rho_g\rho_f}\frac{l}{\overline{v}_{fi}} = \frac{\dot{q}_w\, \Delta\rho}{A_c \overline{v}_{fi}\, \Delta i_{fg}\, \rho_g \rho_f}$$

$$\omega^* = \frac{\omega}{\Omega_{eq}} = \frac{2\pi f}{\Omega_{eq}}$$

Table 9. Reduced Data for Set No. I

Run No.	N_{sub}	$N_{pch,eq}$	Ω_{eq} (per sec)	ω^*
OT 5	1.477	9.540	3.403	1.540
OT 4	1.688	8.410	3.000	1.483
OT 3	2.171	8.010	2.857	1.298
OT 2	2.472	5.770	2.058	1.343
OT 1	3.105	6.090	2.172	1.200
OT 9	4.131	7.350	2.622	0.866
OT 8	4.975	8.210	2.928	0.759
OT 7	5.517	9.200	3.281	0.652
OT 6	6.120	10.370	3.700	0.568
OT 10	7.025	11.800	4.209	0.497

Reproduced with permission of the copyright owner. Further reproduction prohibited without permission.

Table 10. Reduced Data for Set No. II

Run No.	N_{sub}	$N_{pch,eq}$	Ω_{eq} (per sec)	ω^*
OT 55	2.080	5.459	1.862	1.513
OT 54	2.380	5.776	1.970	1.381
OT 53	2.750	6.155	2.100	1.298
OT 52	3.130	6.664	2.273	1.119
OT 51	3.580	7.037	2.400	1.010
OT 59	4.970	9.312	3.176	0.671
OT 58	5.510	10.432	3.558	0.652
OT 57	6.070	11.342	3.869	0.569
OT 56	6.500	11.891	4.056	0.518
OT 60	7.400	13.158	4.488	0.454

Table 11. Reduced Data for Set No. III

Run No.	N_{sub}	$N_{pch,eq}$	Ω_{eq} (per sec)	ω^*
OT 73	1.079	10.650	3.952	1.450
OT 72	1.462	9.650	3.581	1.352
OT 71	1.985	8.700	3.229	1.188
OT 77	2.820	6.830	2.535	1.130
OT 76	3.520	7.190	2.670	0.984
OT 75	4.250	8.276	3.070	0.810
OT 74	4.980	9.290	3.450	0.694
OT 80	5.290	9.430	3.500	0.645
OT 79	5.990	10.220	3.793	0.583
OT 78	6.510	11.020	4.090	0.528

Reproduced with permission of the copyright owner. Further reproduction prohibited without permission.

Table 12. Reduced Data for Set No. IV

Run No.	N_{sub}	$N_{pch,eq}$	Ω_{eq} (per sec)	ω^*
OT 15	1.780	10.850	3.870	1.280
OT 14	2.020	9.410	3.356	1.418
OT 13	2.533	8.870	3.164	1.267
OT 12	2.955	8.140	2.903	1.027
OT 11	3.166	8.796	3.137	0.959
OT 19	3.860	8.210	2.928	0.880
OT 18	4.492	8.860	3.160	0.797
OT 17	5.125	9.520	3.395	0.700
OT 16	5.670	9.990	3.563	0.646
OT 20	6.633	11.610	4.141	0.520

Table 13. Reduced Data for Set No. V

Run No.	N_{sub}	$N_{pch,eq}$	Ω_{eq} (per sec)	ω^*
OT 25	1.600	6.548	1.724	1.970
OT 24	1.869	6.907	1.819	1.838
OT 23	2.382	7.266	1.913	1.616
OT 22	3.015	8.056	2.121	1.385
OT 21	3.560	8.500	2.238	1.115
OT 29	3.680	8.690	2.288	1.052
OT 28	4.583	9.940	2.617	0.862
OT 27	5.370	10.930	2.878	0.716
OT 26	5.940	11.980	3.155	0.692
OT 30	6.844	14.050	3.700	0.561

Reproduced with permission of the copyright owner. Further reproduction prohibited without permission.

Table 14. Reduced Data for Set No. VI

Run No.	N_{sub}	$N_{pch,eq}$	Ω_{eq} (per sec)	ω^*
OT 34	1.870	10.560	5.726	0.952
OT 33	2.170	8.500	4.609	0.944
OT 32	2.470	8.095	4.389	0.931
OT 31	2.864	9.188	4.982	0.823
OT 38	4.070	10.054	5.452	0.639
OT 37	4.764	10.711	5.808	0.570
OT 36	5.310	11.685	6.336	0.511
OT 35	5.520	11.904	6.455	0.435
OT 40	6.390	12.727	6.901	0.384
OT 39	6.750	13.203	7.159	0.361

Table 15. Reduced Data for Set No. VII

Run No.	N_{sub}	$N_{pch,eq}$	Ω_{eq} (per sec)	ω^*
OT 45	1.210	7.610	2.714	1.496
OT 44	1.630	6.029	2.150	1.558
OT 43	2.140	5.299	1.890	1.450
OT 42	2.502	5.566	1.985	1.322
OT 41	2.985	5.838	2.082	1.140
OT 49	4.250	7.482	2.670	0.753
OT 48	4.794	8.431	3.007	0.656
OT 47	5.520	9.521	3.396	0.540
OT 46	5.940	10.050	3.585	0.505

Reproduced with permission of the copyright owner. Further reproduction prohibited without permission.

APPENDIX D

UNCERTAINTY OF THE EXPERIMENTAL DATA

From Chapter II, the uncertainty bands for the temperature, flow, and power measurements are:

Inlet temperature	± 1°F
Inlet flow (for the flow range reported in the present dissertation)	± 3% of the measured flow
Input power	± 4% of the measured power

The method suggested by Kline and McClintock [48] has been used to determine the uncertainty bands for the subcooling number, equilibrium phase change number, and the dimensionless frequency of oscillation, ω^*. For the data reported in the present dissertation, the uncertainty band for the subcooling number is found to be less than ± 0.1, whereas that for the equilibrium phase change number is found to be ± 5% of the measured value. The maximum uncertainty in the non-dimensional frequency of oscillation, ω^*, is also ± 5% of the measured value.

Reproduced with permission of the copyright owner. Further reproduction prohibited without permission.

APPENDIX E

REPEATABILITY OF THE EXPERIMENTAL DATA

To check the repeatability of the experimental data, set number I was re-run after six months from the date of the initial run. The second set is designated as set number I(b), the results of which are tabulated in Table 16. The stability boundaries for sets number I and I(b) are compared in Figure 33. Very good agreement is obtained at low and moderate subcooling numbers. For high subcooling numbers, set number I(b) shows a slightly more stable system than set number I, but it is still within the uncertainty band as shown in Figure 33. The frequency of oscillation for the two sets is compared in Figure 34, and good agreement is found except for one data point.

Table 16. Reduced Data for Set No. I(b)

Run No.	N_{sub}	$N_{pch,eq}$	Ω_{eq} (per sec)	ω^*
OT 104	1.84	7.50	2.68	1.121
OT 103	2.38	6.30	2.25	1.232
OT 102	2.96	6.05	2.16	1.213
OT 101	3.35	6.70	2.39	1.006
OT 108	3.98	7.60	2.71	0.870
OT 107	4.56	8.50	3.04	0.732
OT 106	5.07	9.50	3.39	0.662
OT 105	5.58	10.20	3.64	0.606
OT 109	6.69	12.00	4.28	0.474

Reproduced with permission of the copyright owner. Further reproduction prohibited without permission.

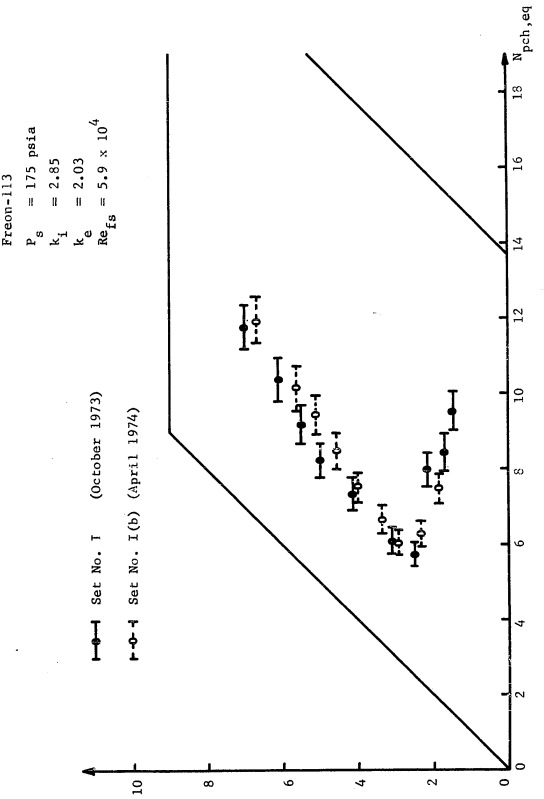

Figure 33. Comparison of Stability Boundary between Sets No. I and I(b)

Reproduced with permission of the copyright owner. Further reproduction prohibited without permission.

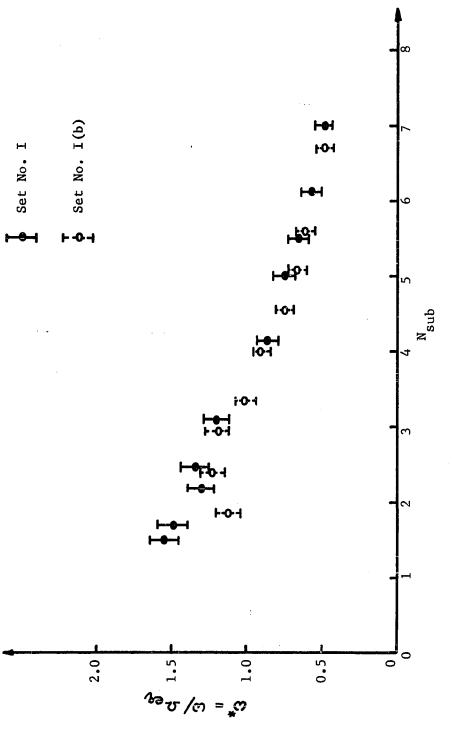

Figure 34. Comparison of Frequency of Oscillation between Sets No. I and I(b)

Reproduced with permission of the copyright owner. Further reproduction prohibited without permission.

BIBLIOGRAPHY

1. Bouré, J. A., Bergles, A. E., and Tong, L. S., "Review of Two-phase Flow Instability," ASME paper no. 71-HT-42.

2. Ishii, M., "Thermally Induced Flow Instabilities in Two-Phase Mixtures in Thermal Equilibrium," Ph.D. Thesis, School of Mechanical Engineering, Georgia Institute of Technology, Atlanta, Georgia, June 1971.

3. Tong, L. S., Boiling Heat Transfer and Two-Phase Flow, John Wiley & Sons Inc., June 1967.

4. Collier, J. G., Convective Boiling and Condensation, McGraw-Hill Book Company (UK) Limited, 1972.

5. Thermodynamic Properties of "Freon" 113, Technical Bulletin T-113A, E. I. du Pont de Nemours and Co., Wilmington, Delaware.

6. Surface Tension of the "Freon" Compounds, Technical Bulletin D-27, E. I. du Pont de Nemours and Co., Wilmington, Delaware.

7. Transport Properties of "Freon" Fluorocarbons, Technical Bulletin C-20, E. I. du Pont de Nemours and Co., Wilmington, Delaware.

8. Yadigaroglu, G., and Bergles, A. E., "Fundamentals and Higher-Mode Density-Wave Oscillations in Two-Phase Flow," Journal of Heat Transfer, ASME Transactions, Series C, Vol. 94, p. 189, 1972.

9. Jeglic, F. A., and Grace, T. M., "Onset of Flow Oscillations in Forced-Flow Subcooled Boiling," NASA TN D-2821, 1965.

10. Serov, E. P., "The Operation of Once-Through Boilers in Variable Regimes," Trudy, Moscow Energ. Ins. 11, 1953.

11. Serov, E. P., "Transient Process in Steam Generators," Teploenergetik, Vol. 13 (9), p. 50, 1966.

12. Serov, E. P., "Analytical Investigation of the Boundary Conditions for the Formulation of Pulsation in Steaming Pipes during Forced Circulation," High Temperature, Vol. 3, p. 545, 1965.

13. Wallis, G. B., and Heasley, J. H., "Oscillation in Two-Phase Flow System," Journal of Heat Transfer, ASME Transactions, Series C, Vol. 83, p. 363, 1961.

Reproduced with permission of the copyright owner. Further reproduction prohibited without permission.

BIBLIOGRAPHY (Continued)

14. Bouré, J., These de Docteur - Ingenier, Universite de Grenoble, France, 1965.

15. Bouré, J., "The Oscillatory Behavior of Heated Channels. An Analysis of Density Effects," C.E.A.R. 3049, Centre d'Etudes Nucleaires de Grenoble, France, 1966.

16. Zuber, N., "Flow Excursions and Oscillations in Boiling Two-Phase Flow Systems with Heat Addition," Symposium on Two-Phase Flow Dynamics, Eindhoven, Vol. 1, p. 1071, September 1967.

17. Meyer, J., and Rose, R., "Application of a Momentum Integral Model to the Study of Parallel Channel Boiling Flow Oscillations," Journal of Heat Transfer, ASME Transactions, Series C, Vol. 85, p. 1, 1963.

18. Carver, M. B., "An Analytical Model for the Prediction of Hydrodynamic Instability in Parallel Heated Channels," Report No. AECL-2681, Atomic Energy of Canada Limited, Chalk River, Ontario, 1967.

19. Ishii, M., and Zuber, N., "Thermally Induced Flow Instabilities in Two-Phase Mixtures," Paper No. B5.11, 4th International Heat Transfer Conference, Paris, 1970.

20. Griffith, P., Clark, J. A., and Rohsenow, W. M., "Void Volume in Subcooled Boiling Systems," ASME Paper No. 58-HT-19, 1958.

21. Bowring, R. W., "Physical Model, Based on Bubble Detachment, and Calculation of Steam Voidage in the Subcooled Region of a Heated Channel," Report No. HPR-10, Institute for Atomenergi, Halden, Norway, 1962.

22. Dix, G. E., "Vapor Void Fractions for Forced Convection with Subcooled Boiling at Low Flow Rates," Ph.D. Thesis, University of California, Berkeley, 1971. Also, General Electric Report No. NEDO-10491.

23. Levy, S., "Forced Convection Subcooled Boiling - Prediction of Vapor Volume Fraction," International Journal of Heat and Mass Transfer, Vol. 10, p. 951, 1967.

24. Staub, F. W., "The Void Fraction in Subcooled Boiling - Prediction of the Initial Point of Net Vapor Generation," Journal of Heat Transfer, ASME Transactions, Series C, Vol. 90, p. 151, 1968.

25. Ahmad, S. Y., "Forced Convection Subcooled Boiling - Prediction of the Onset of Bubble Detachment," Atomic Energy of Canada Limited, Chalk River, Ontario, 1969.

Reproduced with permission of the copyright owner. Further reproduction prohibited without permission.

BIBLIOGRAPHY (Continued)

26. Ahmad, S. Y., "Axial Distribution of Bulk Temperature and Void Fraction in a Heated Channel with Inlet Subcooling," Journal of Heat Transfer, ASME Transactions, Series C, Vol. 92, p. 595, 1970.

27. Costa, J., "Mésure de la Perte de Pression per Acceleration et Étude de l'Apparition du Taux de Vide en Ebullition Locale a Basse Pression," Note TT number 244, CENG, Grenoble, France, 1967.

28. Maurer, G. W., "A Method of Predicting Steady State Boiling Vapor Fraction in Reactor Coolant Channels," WAPD-BT-19, 1960.

29. Rouhani, S. Z., "Void Measurements in the Regions of Subcooled and Low-Quality Boiling," Report No. AE-RTL-849, 1966.

30. Rouhani, S. Z., "Calculation of Steam Volume Fraction in Subcooled Boiling," Journal of Heat Transfer, ASME Transactions, Series C, Vol. 90, p. 158, 1968.

31. Rouhani, S. Z., and Axelsson, E., "Calculation of Void Volume Fraction in the Subcooled and Quality Boiling Regions," International Journal of Heat and Mass Transfer, Vol. 13, p. 383, 1970.

32. Ferrell, J. K., and Bylund, D. M., "Low Pressure Steam-Water Flow in a Heated Vertical Channel," Final Report Volume II on a Study of Convection Boiling inside Channels, North Carolina State University, Department of Chemical Engineering, Raleigh, N. C., 1966.

33. Egen, R. A., Dingee, D. A., and Chastain, J. W., "Vapor Formation and Behavior in Boiling Heat Transfer," Battelle Memorial Institute Report No. BMI-1163, 1957.

34. Martin, R., "Measurement of the Local Void Fraction at High Pressure in a Heating Channel," Nuclear Science and Engineering, Vol. 48, p. 125, 1972.

35. Staub, F. W., Walmet, G. E., and Niemi, R. O., "Heat Transfer and Hydraulics - The Effect of Subcooled Voids," Final Report No. NYO-3679-8. Also, EURAEC-2120, February 1967 - June 1969.

36. Bartolemei, G. G., and Chanturiya, V. M., "Experimental Study of True Void Fraction when Boiling Subcooled Water in Vertical Tubes," Thermal Engineering, Vol. 14, No. 2, p. 123, 1967.

37. Evangelisti, R., and Lupoli, P., "The Void Fraction in an Annular Channel at Atmospheric Pressure," International Journal of Heat and Mass Transfer, Vol. 12, p. 699, 1969.

38. Schlichting, H., Boundary Layer Theory, 6th ed., McGraw-Hill Book Company, p. 578, 1968.

Reproduced with permission of the copyright owner. Further reproduction prohibited without permission.

BIBLIOGRAPHY (Concluded)

39. Zuber, N., and Findlay, J. A., "Average Volumetric Concentration in Two-Phase Flow Systems," Journal of Heat Transfer, ASME Transactions, Series C, Vol. 87, p. 453, 1965.

40. Zuber, N., Staub, F. W., and Bijwaard, G., "Vapor Void Fraction in Subcooled Boiling and Saturated Boiling Systems," Proceedings of the Third International Heat Transfer Conference, Vol. 5, p. 24, AIChE, New York, 1966.

41. Zuber, N., and Dougherty, D. E., "Liquid Metals Challenge to the Traditional Methods of Two-Phase Flow Investigations," Symposium on Two-Phase Flow Dynamics, Eindhoven, Vol. 1, p. 1091, September 1967.

42. Kroeger, P. G., and Zuber, N., "An Analysis of the Effects of Various Parameters on the Average Void Fractions in Subcooled Boiling," International Journal of Heat and Mass Transfer, Vol. 11, p. 211, 1968.

43. Lobachev, A. G., Kolchugin, B. A., Zakharov, E. A., and Kruglikhina, G. G., "Investigation of Vapor Void Fraction in Heated Pipes in Two Phase Upward and Downward Flow," Teploenergetika, No. 5, p. 75, 1973.

44. Kocamustafaogullari, G., "Thermo-Fluid Dynamics of Separated Two-Phase Flow," Ph.D. Thesis, School of Mechanical Engineering, Georgia Institute of Technology, Atlanta, Georgia, December 1971.

45. Porter, B., Stability Criteria for Linear Dynamical Systems, Academic Press, New York, 1968.

46. Zuber, N., "An Analysis of Thermally Induced Flow Oscillations in the Near-Critical and Super-Critical Thermodynamic Region," Final Report NAS8-11422, N.A.S.A., 1966.

47. Popov, E. P., The Dynamics of Automatic Control System, Pergamon Press, 1962.

48. Kline, S. J., and McClintock, F. A., "Describing Uncertainties in Single-Sample Experiments," Mechanical Engineering, Vol. 75, p. 3, 1953.

Reproduced with permission of the copyright owner. Further reproduction prohibited without permission.

VITA

Born on May 5, 1948, Pradip Saha is the eldest son of Mr. Lakshmi Narayan Saha and Mrs. Satya Mayee Saha of Calcutta, India. He graduated from St. Paul's Higher Secondary School, Calcutta in 1963 and entered Bengal Engineering College, University of Calcutta, for his undergraduate education. In June 1968, he received his Bachelor of Engineering (Mechanical) degree and joined the Kuljian Corporation (India) Private Limited as a Design Engineer.

In April 1970, Mr. Saha came to Georgia Institute of Technology for pursuing his graduate studies in mechanical engineering with special interest in thermal and fluid sciences. In September 1971, he received his Master of Science in Mechanical Engineering degree and entered the Ph.D. program in the same institute.

Mr. Saha is co-author of a technical report on heat transfer in gun barrels and a paper on vapor void fraction in subcooled boiling.

Reproduced with permission of the copyright owner. Further reproduction prohibited without permission.